RENSIT:
RadioElectronics. NanoSystems. Information Technologies

Journal "Radioelectronics. Nanosystems. Information Technologies" (abbr. RENSIT)
publishes original articles, reviews and brief reports, not previously published, on topical problems in **radioelectronics (including biomedical) and fundamentals of information, nano- and biotechnologies and adjacent areas of physics and mathematics.**

Designed for **researchers, graduate students, physics students of senior courses and teachers**.
It turns out **2 times a year** (that includes 2 issues)

Authors of journal are academicians, corresponding members and foreign members of Russian Academy of Natural Sciences (RANS) and their colleagues,
as well as other russian and foreign authors on presentation of their manuscripts by the members of RANS, which can be obtained by authors before sending articles to editors.
And also after its receiving - on recommendation of a member of editorial board of journal, or another member of Academy of Natural Sciences, that gave her opinion on article at request of editor.
The editors will accept articles in both **Russian and English** languages.

Articles are internally peer reviewed (**double-blind peer review**) by members of the Editorial Board.
Some articles undergo external review, if necessary.

Journal RENSIT is included in the **DB SCOPUS, EBSCO Publishing,** in the international abstracts database - **Ulrich's International Periodicals Directory**,(USA, New York, http://www.ulrichsweb.com), in the **AJ and DB VINITI RAS** (http://www.viniti.ru), and DB **Russian Science Citation Index (RSCI** http://elibrary.ru/project_risc.asp).

Full-text content is posted in the DB of the **Russian Scientific Electronic Library**
- information resource on the Internet http://elibrary.ru and is available for registered users.
And also - in Open Access **CyberLeninka NEB** of Russian Federation http://cyberleninka.ru.

On journal's website http://www.rensit.ru posted metadata publications
and **RENSIT: Radioelectronics. Nanosystems. Infomation Technologies - english version** (cover-to-cover translation) of journal, which is a party to **CrossRef.**

The founder - the **Russian Academy of Natural Sciences**
Publisher - Publishing Center of the Russian Academy of Natural Sciences
Publisher Address: 29/16, Sivtsev Vrazhek lane, Moscow 119002, Russian Federation

CONTENTS

RUSSIAN ACADEMY OF NATURAL SCIENCES

DEPARTMENT OF RADIOELECTRONICS, NANOPHYSICS AND INFORMATION TECHNOLOGIES PROBLEMS

RENSIT:

RADIOELECTRONICS. NANOSYSTEMS. INFORMATION TECHNOLOGIES.

2023, VOL. 15, № 2

FOUNDED IN **2009**
4 ISSUES PER YEAR
MOSCOW

ISSN 2414-1267

The journal on-line is registered by the Ministry of Telecom and Mass Cjmmunications of the Russian Federation. Certificate El. no. FS77-60275 on 19.12.2014

EDITORIAL BOARD ADDRESS
218-219 of., 7 b., 11, Mokhovaya str., 125009 MOSCOW, RUSSIAN FEDERATION,
TEL. **+7 495 629 3368**
FAX **+7 495 629 3678** FOR GRACHEV

DOI: 10.17725/rensit.2023.15.109

Dynamic thermoelectric model of a heterojunction bipolar transistor taking into account the voltage drop on the emitter metallization tracks

[1,2]Vyacheslav A. Sergeev, [1]Alexander M. Hodakov

[1]Kotelnikov Institute of Radioengineering and Electronics of RAS, Ulyanovsk Branch, http://www.ulireran.ru/

Ulyanovsk 432071, Russian Federation

[2]Ulyanovsk State Technical University, https://www.ulstu.ru/

Ulyanovsk, 432027, Russian Federation

E-mail: sva@ulstu.ru, hod22am@mail.ru

Received March 20, 2023, peer-reviewed March 27, 2023, accepted April 06, 2023

Abstract: **A dynamic 3D thermoelectric model has been developed to calculate the temperature field and emitter current density in the comb structure of a heterojunction bipolar transistor (HBT) with the length of the emitter metallization paths comparable to the size of the crystal, taking into account the inhomogeneous distribution of current density under the emitter paths caused by a voltage drop on the resistance of the current-carrying metallization. The model is based on an iterative solution in the COMSOL Multiphysics software environment of a non-stationary heat equation together with a system of equations for the distribution of electric potential along the emitter path and the current density under the path. It is shown that during the action of the heating power pulse in the HBT, the distribution of temperature and current density along the emitter tracks change character, respectively, from homogeneous and monotonically decreasing to non-monotonically changing. At the same time, the maximum temperature and current density reach stationary values with a rate significantly exceeding the rate of overheating increase with homogeneous heating of the structure, and the maxima of temperature and current density in the process of self-heating shift from the beginning to the center of the tracks. The proposed model can be used to evaluate the thermomechanical stresses in the structure of the HBT and the limiting electrical parameters in the pulsed modes of operation of the HBT.**

Keywords: **heterojunction bipolar transistor, dynamic thermoelectric model, current density, temperature, inhomogeneity**

UDC 621.382.029

Acknowledgments: This work was supported by the Russian Science Foundation (project no. 22-29-01134).

For citation: Vyacheslav A. Sergeev, Alexander M. Hodakov. Dynamic thermoelectric model of a heterojunction bipolar transistor taking into account the voltage drop on the emitter metallization tracks. *RENSIT: Radioelectronics. Nanosystems. Information Technologies,* 2023, 15(2):109-116e. DOI: 10.17725/rensit.2023.15.109.

CONTENTS

1. INTRODUCTION

Along with the active development of MIS and HEMT microwave transistors, modern radio and telecommunications equipment widely uses high-power bipolar (BT), including heterojunction (HBT), microwave transistors [1-4]. Devices of this class are the least reliable as part of modern radio-electronic systems for various purposes, since they operate in the most severe thermal and electrical conditions. This class of devices is characterized by the presence of a strong positive thermal feedback (PTF) and the manifestation of the effects of an inhomogeneous and unstable distribution of current density, power and temperature in transistor structures [5-7], which lead to local overheating and thermomechanical stresses of the structure and, as a result, to the acceleration of degradation mechanisms and instrument failures.

One of the most common geometries of the structures of modern high-power BTs and HBTs is a strip or comb geometry with a parallel arrangement of elementary transistors (cells) of HBTs (see **Fig. 1** [4] and **Fig. 2** [7]). Self-heating of each HBT cell by dissipated power and thermal coupling between neighboring cells lead to an uneven temperature profile of the HBT elementary transistor matrix. Due to the positive temperature coefficient of the emitter current, currents of higher density will flow through the central cells of the HBT with a higher temperature, which

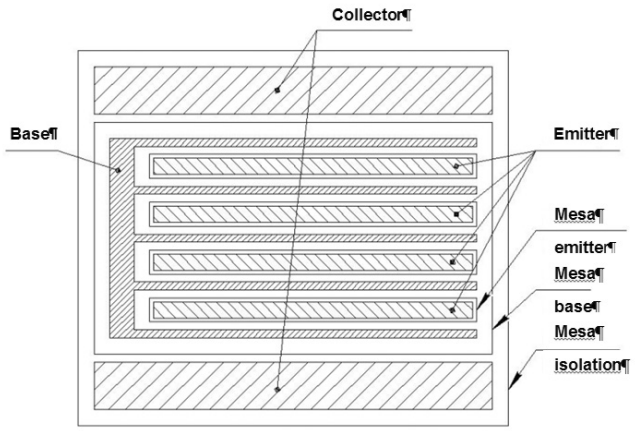

Fig. 1. *Topology of the HBT active region* [4].

leads to an increase in heat release, which can ultimately lead to thermal breakdown or degradation of the device [8, 9], which is especially strong. manifests itself at high levels of injection [10].

In order to reduce the uneven temperature distribution and solve these thermal problems, various options for one-dimensional geometry design are used, including changing the length of the emitter in HBT cells [7] and changing the distance between emitters between HBT cells [8], which allows to reduce the temperature difference between individual cells.

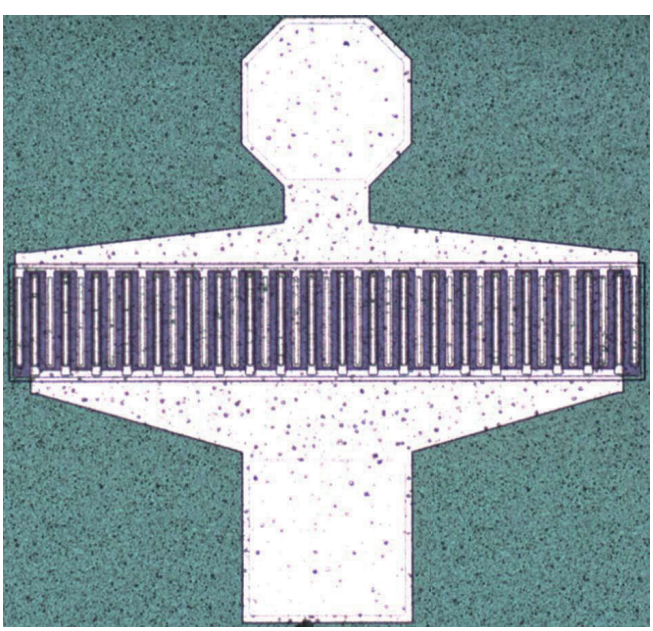

Fig. 2. *Comb structure of HBT with 20 elementary transistors* [7].

In well-known works, thermoelectric processes in comb-like HBT structures were considered without taking into account the voltage drop on the current-carrying tracks of emitter metallization, which leads to a significant inhomogeneous distribution of the emitter current density, and hence the power dissipation density along the emitter tracks [11-13].

In [14], we considered a stationary thermoelectric model of the HBT microwave transistor structure, taking into account the voltage drop on the current-carrying tracks of the emitter metallization. It is shown that the distributions of temperature and current density along the emitter tracks of the structure change their character: from monotonically and weakly decreasing from the beginning of the track to the end in the isothermal approximation, these distributions become nonmonotonic and essentially inhomogeneous. In addition, the maximum current density and temperature shift from the beginning to the center of the track with an increase in the operating current. Note that for semiconductor structures, it is not the absolute deviation of the local temperature of the structure from the average value that is critically important, but the gradient of temperature change, which determines the level of thermomechanical stresses and the dynamics of electromigration processes in the elements of the structure [15].

In radio-electronic systems of HBT microwave transistors, as a rule, operate not in stationary, but in pulsed modes with the duration and duty cycle of the pulses varying over a wide range. In this case, it is obvious that during the action of the dissipated power pulse, the distribution of current density and temperature in the structure will be transformed. This article presents a 3D thermoelectric model for calculating the temperature field and the distribution of the emitter current density in the comb structure of the GBT, taking into account the joint influence of all the above factors of the inhomogeneous distribution of current and temperature in the device structure, including the inhomogeneous distribution of the current density under the emitter tracks as a result of the voltage drop across resistance of current-carrying metallization.

2. THERMOELECTRIC MODEL

Fig. 3 shows the geometry of the HBT semiconductor structure model used in calculating the temperature fields, which is a rectangular semiconductor crystal with dimensions $l_x \times l_y \times l_z$, with emitter metallization tracks located on its upper surface with dimensions $a_e \times L_e \times h_e$. The crystal is placed on an ideal heat sink with temperature T_0. As in [14], assuming the emitter tracks to be narrow, we neglect the effect of pushing the emitter current to the side edges of the tracks along the coordinate x.

The temperature field in the HBT structure $T(x,y,z,t)$ at an arbitrary time t in the process of self-heating of the structure by a heating power pulse is found from the solution of the non-stationary heat conduction equation

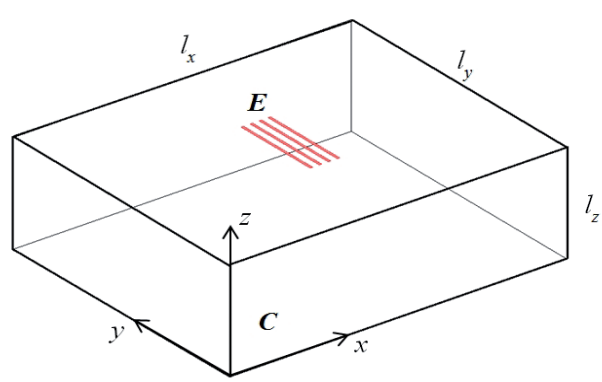

Fig. 3. *Geometry of the HBT structure model: E – emitter, C - semiconductor crystal.*

$$c(T)\,\rho(T)\frac{\partial T}{\partial t}+\nabla_{x,y,z}\left(\lambda(T)\nabla_{x,y,z}T\right)=0, \quad (1)$$

where c, ϱ, λ – coefficients of heat capacity, density and thermal conductivity of the crystal material, with the following boundary conditions:

- side surfaces and the upper surface of the crystal are thermally insulated;
- the temperature of the lower surface of the crystal is equal to the temperature of the heat sink T_0;
- on the upper surface in the region of the emitter of the structure, the heating power density is given, which is determined by the formula:

$$q_e(T)=-\lambda(T)\frac{\partial T}{\partial z}\bigg|_{z=l_z}=\begin{cases}J_e(T)U_c,(x,y)\in S_e\\0,(x,y)\in S-S_e\end{cases}, \quad (2)$$

where S, $S_e = na_eL_e$ – area of the upper surface of the crystal and its active region, n – number of emitter tracks, J_e, U_c – emitter current density and collector voltage.

As an initial condition for the temperature in solving equation (1), a uniform temperature distribution over the HBT structure was taken

$$T(x,y,z,0) = T_0. \quad (3)$$

Emitter current density distribution J_e under the track of the emitter metallization of the structure is found from the solution of the following system of equations:

$$J_e(T)=$$
$$=J_{e0}\left(T/T_0\right)^3\exp\left\{\frac{-E_g+e\left(U_e-\varphi_e-rS_en^{-1}J_e(T)\right)}{kT}\right\}, \quad (4)$$

where J_{e0} – parameter weakly dependent on temperature, U_e – direct voltage drop across the emitter *p-n* junction, E_g – semiconductor bandgap, e – electron charge, φ_e – emitter metallization potential, r – transistor input ohmic resistance, k – Boltzmann's constant;

$$\frac{dJ_{em}(y)}{dy}=-\frac{J_e(y)}{h_e}, \quad (5)$$

$$\frac{d\varphi_e(y)}{dy}=-\frac{J_{em}(y)}{\sigma_{em}}, \quad (6)$$

$$J_{em}(y_{eb})=I_e/h_ea_e, \quad (7)$$

$$J_{em}(y_{ee})=0, \quad (8)$$

$$\frac{d\varphi_e}{dy}\bigg|_{y=y_{eb}}=-\frac{I_e}{\sigma_{em}h_ea_e}, \quad (9)$$

$$\frac{d\varphi_e}{dy}\bigg|_{y=y_{ee}}=0, \quad (10)$$

where I_e – total emitter current, J_{em} – current density by emitter track metallization, y_{eb} and y_{ee} – track start and end coordinates, σ_{em} – specific conductivity of emitter track metallization.

To ensure the condition for switching on the transistor in an electrical circuit (constancy of the total emitter current I_e) it is necessary that the equality be satisfied:

$$\iint_{S_e}J_e(x,y,t)\,dx\,dy=I_e. \quad (11)$$

3. SOLUTION OF THE PROBLEM AND RESULTS OF CALCULATIONS

The model non-stationary problem (1)-(11) was solved by the method of successive time intervals [16], that is, the entire time of the heat transfer process was divided into a number of intervals $\Delta t = t_j - t_{j-1}$, within which the non-stationary heat conduction equation was solved with the initial power density $q_{cj}(x,y,l_z,t_{j-1})$ and temperature $T_j(x,y,l_z,t_{j-1})$ distributions, found as a result of solving on previous interval. The values of the potentials U_e and φ_e were found by a numerical iterative method, a similar algorithm of which is presented in [17]. As an initial approximation of the dependence $J_e^0(y)$ in the iterative process, the current density values calculated by the formula [18] were chosen:

$$J_e^0(y)=\frac{2\varphi_{T_0}}{L_ea_eR_e}\cdot\frac{C^2}{\cos^2\left[C\left(1-y/L_e\right)\right]}, \quad (12)$$

where $\varphi_{T_0} = \frac{kT_0}{e}$ – temperature potential at T_0 = 300 K, the value of which is equal to 26 мВ; R_e – metallization resistance of the emitter track, and the constant C is found from the solution of the equation $C\mathrm{tg}C = R_e I_e / 2n\varphi_{T0}$.

The original program included an appeal to the COMSOL Multiphysics interactive software environment. As in [14], an InGaP/GaAs GBT with a crystal size of 300×250×100 microns and an active transistor structure with four gold emitter tracks with a width a_e = 2 microns and a thickness of h_e = 0.5 microns was chosen as the calculated base object of the study, while the length of the tracks during calculations varied and was set within L_e = (40÷80) microns. The functional dependences on the temperature of the thermophysical characteristics c, ϱ, λ of the crystal material were selected from the COMSOL program materials database. The temperature of the ideal heat sink T_0 was assumed to be 300 K.

In order to compare the calculation results with the results of calculations based on the stationary model, numerical calculations based on the proposed dynamic model are given for a variant of the transistor operating mode at I_e = 40 мА, U_c = 7 В. The initial value of the offset voltage at the emitter junction U_e = 1.2 В. The total current of the transistor structure was considered evenly distributed between the emitter metallization tracks.

Figures 4 and **5** show the dynamics of changes in the maximum and average temperature of the structure, as well as the maximum emitter current density of the HBT structure during the action of a heating power pulse.

Approximating the change in the maximum and average overheating of the structure by a function of the form $\Delta T(1 - \exp(-t/\tau_T))$, where τ_T thermal

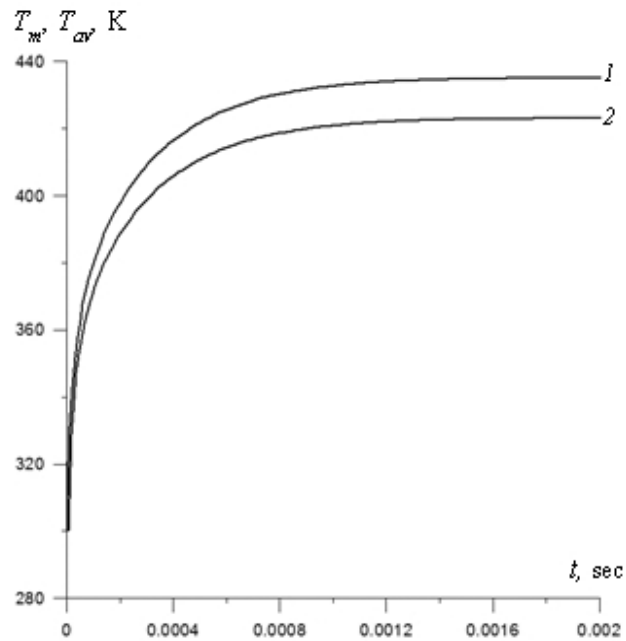

Fig. 4. *Change in the maximum (1) and average (2) temperature of the active region: I_e = 40 mA, U_c = 7 V; a_e = 2 μm, L_e = 60 μm, h_e = 0.5 μm.*

time constant that determines the rate of increase of overheating, according to the obtained dependences, it is possible to estimate the change in the rate of increase of overheating as a result of inhomogeneous current distribution under the action of positive thermal feedback in

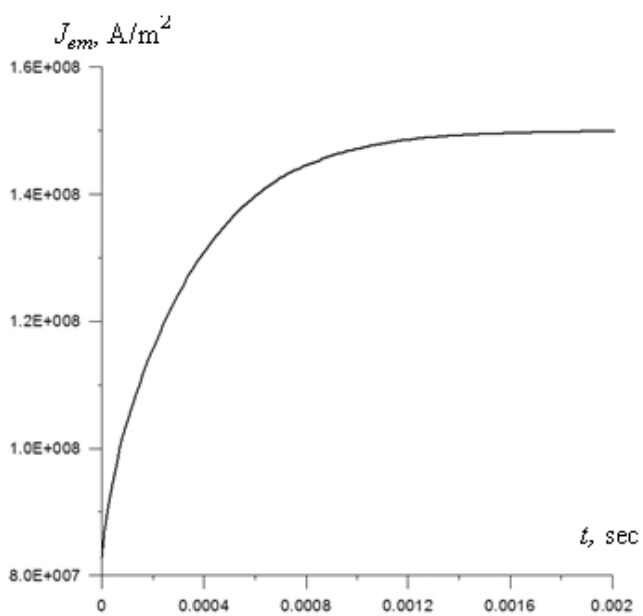

Fig. 5. *Changing the maximum emitter current density: I_e = 40 mA, U_c = 7 V; a_e = 2 μm, L_e = 60 μm, h_e = 0.5 μm.*

the structure compared with the case of homogeneous heating of the structure. When the structure is heated by a uniformly distributed power density $\tau_T^{homogen} = \tau_{Tcr}$, where τ_{Tcr} thermal time constant of the crystal, determined by the thermal diffusivity of the crystal material and its thickness d: $\tau_{Tcr} = d^2/\alpha$. For a GaAs crystal with a thickness of 100 microns is about 300 microseconds. From the dependencies in Fig. 4 and Fig. 5, it can be seen and numerical calculations show, that the thermal time constant $\tau_T^{heterogen}$ with inhomogeneous heating and the action of PFT is approximately 130 microseconds, that is, 2.3 times less $\tau_T^{homogen}$, that is, the rate of change in the maximum and average overheating of the structure significantly exceeds the rate of increase in overheating with homogeneous heating of the structure. This is obviously due to the redistribution of the current density along the emitter metallization tracks and, accordingly, the power density dissipated in the HBT collector junction under the track.

From the distributions of overheating along the emitter track presented in **Fig. 6**

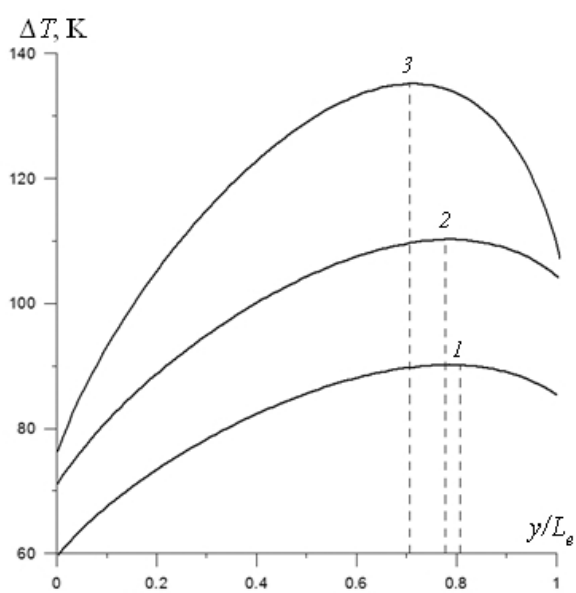

Fig. 6. *Overheating along the 3rd emitter track: I_e = 40 mA, U_c = 7 V; a_e = 2 μm, L_e = 60 μm, h_e = 0.5 μm; t: 1 – 0.15, 2 – 0.3, 3 – 2 ms.*

at different times, it can be seen that in the process of HBT heating, the maximum temperature value shifts from the edge of the track to its center, i.e., to the center of the crystal.

It should also be noted again that the proposed model did not consider the redistribution of the total current of the structure between the cells as a result of uneven heating of the cells of the HBT structure due to their different arrangement with respect to the edges of the crystal. This effect will probably lead to even greater inhomogeneity of the temperature and current density distributions in the structure and requires a separate additional analysis.

4. CONCLUSION

The developed dynamic thermoelectric model of the HBT comb structure, taking into account the inhomogeneous distribution of the emitter current density as a result of the voltage drop on the emitter metallization tracks and the positive thermoelectric feedback acting in the HBT structure, determines the rate and nature of the change in the temperature and current density distribution along the emitter tracks of the structure under the action of a pulse heating power in HBT: from monotonically and weakly decreasing from the beginning of the track to the end in the isothermal approximation, these distributions become nonmonotonic and significantly inhomogeneous. In this case, the maximum temperature and current density reach stationary values at a rate significantly exceeding the rate of increase in overheating during uniform heating of the structure, and the temperature and current density maxima in the process of self-heating of the structure shift from the beginning to the center of

the tracks. The proposed model can be used in the development of HBT structures and evaluation of their limiting functionality in terms of current and temperature in the pulsed operating modes of the HBT.

REFERENCES

1. Jianjun Gao. *Heterojunction Bipolar Transistors for Circuit Design: Microwave Modeling and Parameter Extraction*. United States, John Wiley & Sons Inc, 2015, 280 p.
2. Xin Wen, Akshay Arabhavi, Wei Quan. Performance Prediction of InP/GaAsSb Double Heterojunction Bipolar Transistors for THz applications. *J. Appl. Phys.*, 2021, 130:034502.
3. Lachner R. Industrialization of mmWave SiGe technologies: Status, future requirements and challenges. *IEEE 13th Topical Meeting on Silicon Monolithic Integrated Circuits in RF Systems*, 2013:105-107.
4. Kozlovskij EYu, Zaharov SI, Semenova LM, Tejder AA. Razrabotka tekhnologii izgotovleniya geterobipolyarnykh tranzistorov na osnove struktur InGaP/GaAs [Development of manufacturing technology for heterobipolar transistors based on InGaP/GaAs structures]. *Sb. trudov 31-oj Mezhdunarodnoj konferencii "SVCH-tekhnika i telekommunikatsionnye tekhnologii, KryMiKo"*, Sevastopol, SevGU, 2021, 3:27-29 (in Russ.).
5. Lee CP, Chau FHF, Ma W, Wang NL. The Safe Operating Area of GaAs-Based Heterojunction Bipolar Transistor. *IEEE Trans. Electron.*, 2006, 53(11):2681-2688.
6. Chen Liang. Thermal stability improvement of a multiple finger power SiGe heterojunction bipolar transistor under different power dissipations using non-uniform finger spacing. *Chinese Physics B*, 2011, 20:018501.
7. Jin Dongyue. Thermal stability of the power SiGe HBT with non-uniform finger length. *Proc. International Conference on Microwave and Millimeter Wave Technology,* 2008:166-169, doi: 10.1109/ICMMT.2008.4540331.
8. Dongyue Jin, Wanrong Zhang, Hongyun Xie, Liang Chen, Pei Shen, Ning Hu. Structure optimization of multi-finger power SiGe HBTs for thermal stability improvement. *Microelectronics Reliability,* 2009, 49(4):382-386.
9. Rui Chen. Thermal resistance matrix representation of thermal effects and thermal design in microwave power HBTs with two-dimensional array layout. *Chinese Phys. B*, 2019; doi: 10.1088/1674-1056. ab3436.
10. Lu Z, Zhou L, X. Hu X. Electro-Thermal analysis of SiGe HBT under HPM Injection. *IEEE MTT-S International Conference on Numerical Electromagnetic and Multiphysics Modeling and Optimization (NEMO)*, 2020:1-4.
11. Caves KY, Barnes IA. Optimum length of emitter stripes in "comb" structure transistors. *IEEE Trans*, 1965, ED-12(2):84-85.
12. Sergeev VA, Khodakov AM. Two-Section Model of the Current Distribution in Strip Layouts of Bipolar and Hetero-Bipolar Microwave Transistors. *Journal of Communications Technology and Electronics,* 2022, 67(11):1400-1405.
13. Sergeev VA. Analiticheskaya model neizotermicheskogo raspredeleniya plotnosti moshchnosti v strukturakh bipolyarnykh tranzistorov [Analytical model of non-isothermal power density distribution in bipolar transistor structures]. *Izvestiya vuzov. Elektronika*, 2005, 3:22-28, (in Russ.).

14. Sergeev VA, Hodakov AM. Thermoelectric model of a heterojunction bipolar transistor taking into account the voltage drop on the current-carrying metallization. *RENSIT: Radioelectronics. Nanosystems. Information technologies*, 2022, 14(2):103-110. DOI: 10.17725/rensit.2022.14.103.
15. Hodakov AM, Tarasov RG, Sergeev VA, KulikovAA. Thermal deformation model of the submodule of the X-band output power amplifier. *RENSIT: Radioelektronika. Nanosistemy. Informacionnye Tehnologii*, 2021, 13(1):13-18. DOI: 10.17725/rensit.2021.13.013.
16. Kozdoba LA. *Reshenie nelinejnyh zadach teploprovodnosti* [Solving nonlinear heat conduction problems]. Kiev, Naukova dumka Publ., 1976, 136 p.
17. Sergeev VA, Hodakov AM. *Nelinejnye teplovye modeli poluprovodnikovykh priborov* [Nonlinear thermal models of semiconductor devices]. Ul'yanovsk, UlGTU Publ., 2012, 159 p.
18. Sergeev VA, Hodakov AM. Thermal model of a heterojunction bipolar transistor taking into account the voltage drop on the emitter fingers of metallization. *Moscow Workshop on Electronic and Networking Technologies (MWENT),* 2022. DOI: 10.1109/MWENT55238.2022.9802430.

DOI: 10.17725/rensit.2023.15.117

Modeling of thermoelectrical processes in a power MOSFET modules

[1,2]Vitaliy I. Smirnov, [1]Alexander M. Hodakov, [1]Andrey A. Gavrikov

[1]Kotelnikov Institute of Radioengineering and Electronics of RAS, Ulyanovsk Branch, http://www.ulireran.ru/
Ulyanovsk 432071, Russian Federation
[2]Ulyanovsk State Technical University, https://www.ulstu.ru/
Ulyanovsk 432027, Russian Federation

E-mail: smirnov-vi@mail.ru, hod22am@mail.ru, a.gavrikoff@gmail.com

Received April 25, 2023, peer-reviewed May 03, 2023, accepted May 10, 2023

Abstract: **The paper represents thermal model of power MOSFET module based on a transistors mounted on copper-ceramic DBC (Direct Bond Copper) plate. The analysis of thermal processes in the module caused by pulse heating of particular transistors was performed by the finite elements method using COMSOL Multiphysics. The model performs estimation of the temperature field on the DBC plate and transistors overheat temperature. The modeling results was compared to the experiment – thermal impedance matrix measured by the modulation method using the heating power modulated by the harmonic law. Analysis of the data obtained allows to conclude that the calculated and experimental values of the dies overheating temperature are in good agreement with each other and confirms the correctness of the developed thermal power module model.**

Keywords: **power module, MOSFET, thermal model, temperature filed, thermal resistance**

UDC 621.382.32

Acknowledgments: The work was supported by the Russian Science Foundation (project No. 23-29-00026).

For citation: Vitaliy I. Smirnov, Alexander M. Hodakov, Andrey A. Gavrikov. Modeling of thermoelectrical processes in a power MOSFET modules. *RENSIT: Radioelectronics. Nanosystems. Information Technologies,* 2023, 15(2):117-124e. DOI: 10.17725/rensit.2023.15.117.

Contents

1. INTRODUCTION

Power modules are widely used in various industries, including transport, electric power, metallurgy, industrial electric drive, etc. They usually consist of several powerful MOSFETs or IGBTs mounted on a common heat-conducting substrate, enclosed in a sealed case. The main requirements for power modules are the ability to switch high currents at high frequency and withstand high voltages in the closed state. Unlike devices of similar purpose, implemented on discrete electronic components, power modules have a much higher power density. In them, due to the dense dies arrangement, active and parasitic connections between the module elements are sharply reduced, which increases the efficiency and reduces possible overloads and the level of electromagnetic interference when switching transistors [1].

A feature of power modules operation is that at any time only a part of the transistors are in the open state, the other transistors are closed. The result is inhomogeneous heating of the module dies and, as a consequence, inhomogeneous temperature distribution over the substrate surface. This can lead to the average temperature over the substrate within the normal

range, some dies will have a temperature above the maximum allowable. To prevent this, it is necessary to control the temperature of each module chip. Such a problem can be solved either by analyzing the thermal model or by measuring the thermal impedance matrix, which takes into account thermal cross-links between the module transistors.

2. OBJECT AND RESEARCH METHOD

The object of research was the power module SK85MH10T manufactured by Semikron, consisting of four power MOSFETs mounted on a board made using DBC technology (Direct Bond Copper). The design of the module is shown in **Fig. 1***a*, where the numbers indicate: 1 – die; 2 – jumper; 3 – DBC board; 4 – radiator; 5 – dielectric; 6 – base of the module. The basis of the DBC board is an Al_2O_3 ceramic substrate, on both sides of which a copper foil is attached by sintering in an oxygen atmosphere. The copper foil provides high electrical and thermal conductivity to the mounting layer of the DBC board, and the ceramic base provides good insulating properties. The structure of the transistor formed in each module chip is shown in Fig. 1*b*.

To study the mutual influence of thermal connections between the transistors of the module, measurements of cross-coupled thermal resistances and determination of the elements of the thermal impedance matrix were carried out. In order to maintain the temperature of the base of the module constant due the measurements, the module was attached to the heatsink using thermal grease. After measuring cross thermal resistances, the module cover was dismantled in order to determine the exact dimensions of the chips and their location on the DBC board, which is necessary to simulate the thermal processes that occur when heating current pulses pass through the module transistors.

Fig. 1*b* shows only part of the power MOSFET structure, namely its base cell. In reality, a powerful MOSFET is made up of many such base cells, which can number in the thousands. A feature of the structure is the presence in each base cell of an antiparallel diode between the p^+ source region and the n^- drain region. When the transistor is open, when the current flows from the drain to the source, the anti-parallel diode does not affect the operation of the transistor in any way. However, the JEDEC standard [2] recommends using it to measure the die temperature. To do this, a small measuring current is passed through the diode (shown by arrows in Fig. 1*b*) and the voltage USD between the source and drain is measured, which decreases linearly with increasing die temperature. It should be taken into account that the voltage USD is measured for a plurality of diodes connected in parallel, while the value of USD depends on the local temperature of the die. In the case of a non-uniform temperature distribution across the die, the measured USD voltage will determine the highest local temperature of the die.

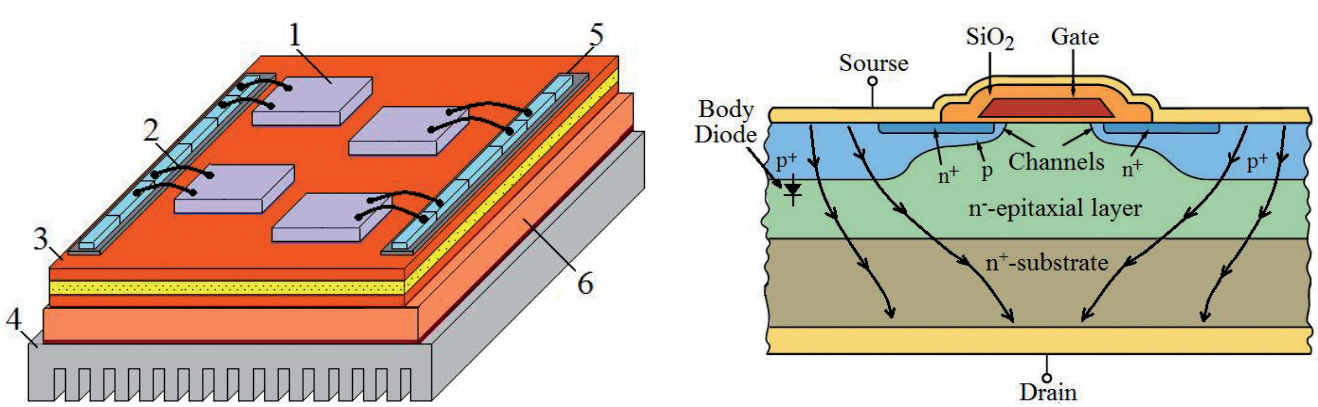

Fig. 1. *Power module SK85MH10T: a) design; b) MOSFET structure.*

The most widely used method for studying thermoelectric processes in power modules is the analysis of their thermal model. To build a model, the principle of thermoelectric analogy is often used [3], according to which thermal parameters (heat flux, temperature, thermal resistance, heat capacity, etc.) correspond to an electrical analogue (current strength, voltage, resistance, electric capacitance, etc.). In this case, the object is represented by an equivalent circuit consisting of RC-chains connected in a certain way according to its design. Usually, Cauer or Foster substitution circuits are used [4]. Thermal processes occurring in an object are mathematically described similarly to electrical processes in an equivalent circuit.

To determine the equivalent circuit parameters, either used information about the material and geometry of the structural elements of the object or experimental results. An illustration of the first approach is the work [5], in which the authors managed to calculate the parameters of all elements of the power module from six pairs of IGBTs and diodes located on a copper base that has thermal contact with an aluminum radiator. To experimentally determine the parameters of the equivalent circuit, measurements of transient responses are often used. A sequence of heating current pulses with a duration increasing according to a logarithmic law is passed through the object, and after each pulse, the response to this effect is measured – the change in the dies temperature until a steady state is reached. An analysis of the heating curve allows to determine the thermal resistance components used to build a model of a multi-chip system [6]. Modeling methods based on solving the heat equation are widely used. In this case, either the finite element method [7] or the differential difference method [8] is used to calculate heat fluxes in a multi-die system.

The processes of heat removal from heated dies through the substrate to the base of the module case, as well as lateral flows to neighboring module dies, are characterized by a thermal impedance matrix $Z_{Txy}(j\omega)$:

$$\mathbf{T}_x(j\omega) = \mathbf{Z}_{\mathbf{T}xy}(j\omega) \cdot \mathbf{P}_y(j\omega), \quad (1)$$

where $\mathbf{T}_x = \begin{pmatrix} T_1 \\ \dots \\ T_m \end{pmatrix}$, $\mathbf{P}_y = \begin{pmatrix} P_1 \\ \dots \\ P_n \end{pmatrix}$, $\mathbf{Z}_{\mathbf{T}xy} = \begin{pmatrix} Z_{T11} & \dots & Z_{T1n} \\ \dots & \dots & \dots \\ Z_{Tm1} & \dots & Z_{Tmn} \end{pmatrix}$.

The one-dimensional arrays $T_x(j\omega)$ and $P_y(j\omega)$ are the frequency-dependent characteristics of the temperature at point X and the power dissipation at point Y, and $Z_{Txy}(j\omega)$ defines the thermal coupling between points X and Y. To determine the thermal coupling between each pair of elements, which are part of the system, the authors of [9] proposed to use the PRBS method (Pseudorandom Binary Sequence – pseudo-random binary sequence). PRBS is a special signal that has an almost constant spectrum over a wide frequency range. Using PRBS as the input power $P_y(t)$ and measuring the temperature response $T_x(t)$, the elements of the thermal impedance matrix can be determined:

$$Z_{Txy}(\omega) = \frac{\boldsymbol{F}(T_x(t))}{\boldsymbol{F}(P_y(t))} = \frac{T_x(\omega)}{P_y(\omega)},$$

where $T_x(t)$ и $P_y(t)$ – time representations of the temperature at point X and the power dissipated at point Y, and F denotes the discrete Fourier transform.

Another approach was used in [10], where the authors used the modulation method of the effect of thermal power on the measurement object to measure the matrix elements. To do this, a sequence of heating current pulses with a fixed amplitude and repetition period, but with a duration varying according to a harmonic law, was passed through the transistors of the module [11]. This caused a periodic change in the die's temperature with the same modulation frequency as that of the heating power, but with a phase shift. By measuring the amplitude of the variable temperature component and the phase shift, it is possible to determine the elements of the thermal impedance matrix.

3. POWER MODULE THERMAL MODEL

The object of thermal modeling is the power module SK85MH10T, the design of which is shown in Fig. 1*a*. The module consists of four high-power MOSFETs mounted on a DBC board with dimensions $b \times c \times h_p$. Transistors are formed in silicon dies of square section $a \times a \times h_c$. The DBC board is mounted on a heatsink that keeps the bottom surface temperature constant.

The temperature field in the structure of the power module is found from the solution of the non-stationary heat conduction equation:

$$c_i(T_i)\,\rho_i(T_i)\frac{\partial T_i}{\partial t} = \nabla_{x,y,z}\left(\lambda_i(T_i)\nabla_{x,y,z}T_i\right), (i=1,...,5) \quad (2)$$

where $\lambda_i(T_i)$, $c_i(T_i)$, $\rho_i(T_i)$ are the coefficients of thermal conductivity, specific heat capacity, and density of the layers of the structure.

The initial and boundary conditions:

$T_i(x, y, z, 0) = T_0$,

where T_0 – ambient temperature. On the upper surface of the transistor dies, the density of the thermal power dissipated by the transistor die is set:

$$q_i(t) = -\lambda_i(T_i)\frac{\partial T_i}{\partial z}\bigg|_{z=h_p+h_c}, (i=1,...,4). \quad (3)$$

On the lower boundary of the model structure, which is in the zone of contact with the base of the module, the heat flow spreading condition is set:

$$-\lambda_5(T_5)\frac{\partial T_5}{\partial z}\bigg|_{z=0} = \alpha_{sp}(T_5(x,y,0,t) - T_0),$$

where $\alpha_{sp} = 1/(b \times c \times R_{sp})$ – the effective heat transfer coefficient of the DBC board with the base of the power module and the heatsink, and RSP is the thermal spreading resistance [12]. On all other free surfaces Σ of the structure of the power module, there is no heat exchange with the external environment:

$$\frac{\partial T_i}{\partial n}\bigg|_{\Sigma} = 0.$$

The heat conductivity equation (2) was solved by the finite element method using the COMSOL Multiphysics software environment. The dimensions of the transistor die were $a \times a \times h_c = 6 \times 6 \times 0.5$ mm^3, and DBC-board $b \times c \times h_p = 40 \times 28 \times 1.0$mm^3.

The main physical properties of the materials of the structure of the studied power module are presented in **Table 1**. The temperature dependences of the thermophysical characteristics of silicon used in solving the thermal problem were taken from the COMSOL library of materials. Initial temperature $T_0 = 300$ K.

As in [10], the module heating by pulse-width modulated current pulses using only two transistors (1 and 2) was modeled. As a result of current pulses flowing through the transistor, the average heating power over the repetition period changed according to the harmonic law:

$$P(t) = P_{av} + P_1 \sin(2\pi\nu t),$$

where P_{av} – average heating power, $P_1 = aP_{av}$ – amplitude of the variable component of the heating power, ν – modulation frequency, a – modulation factor. The amplitude of the variable component of the heating power dissipated in the transistor 1, $P_1 = 1.12$ W, in transistor 2 – $P_1 = 1.04$ W, with modulation factor $a = 0.5$. With $\nu = 55$ Hz the dependences of power density (3) on time will be determined by the expression:

$$q_1(t) = 62222[1 + 0.5\sin(2\pi 55t)],$$
$$q_2(t) = 57778[1 + 0.5sin(2\pi 55t)].$$

The effective heat transfer coefficient was a model parameter. Its value was calculated according to the method presented in [12] and

Table 1

Physical parameters of structural elements of the power module

Structure element	Material	ϱ, kg/m^3	λ, W/(m·K)	c_p, J/(kg·K)
Die	Si	2330	$\lambda(T)$	$c_p(T)$
DBC board	Cu Al_2O_3	8700 3900	400 27	385 776

refined by the iterative method according to the experimental data on the heating temperature of the module structure element. In the presented calculation variant, this temperature was the junction temperature of the 1st transistor.

4. MODELING RESULTS AND THEIR ANALYSIS

The results of calculating the temperature field created by the heated dies of the module during the flow of current pulses through transistors No. 1 and No. 2 are shown in **Fig. 2**. On the right is a color temperature scale that allows you to evaluate the temperature at various points in the module.

Since the power modules mainly operate in a pulsed mode, when some of the transistors are open and the rest are closed, the temperature dynamics of all transistors, including transistors in the closed state, is of interest. The results of calculating the change in the overheating temperature of transistors under pulsed action are shown in **Fig. 3**.

The simulation results were compared with the experimental studies results [10]. The purpose of the research was to measure the elements of the thermal impedance matrix of the SK85MH10T power module, which consists of four powerful MOSFETs mounted on a copper-ceramic board. To solve this problem, a modulation method for measuring thermal resistance was used, using the heating

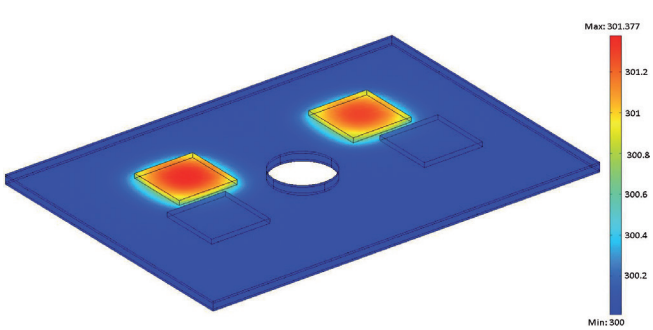

Fig. 2. *The results of the power module's temperature field calculation: 1…4 – MOSFET dies, 5 – DBC board.*

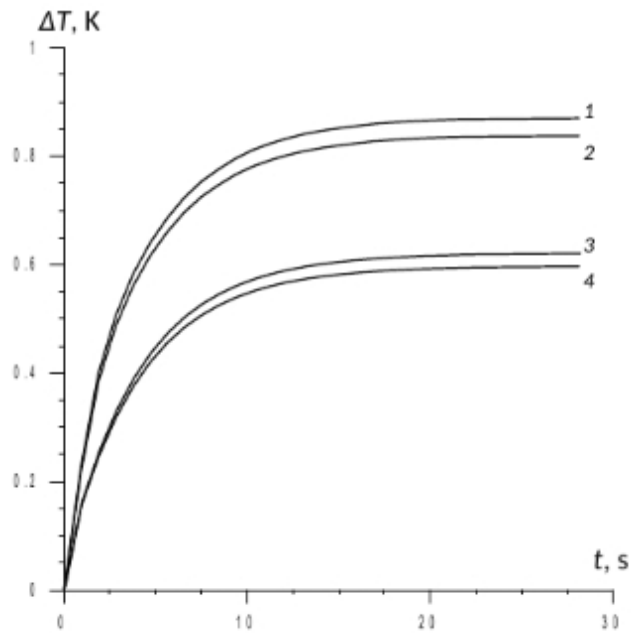

Fig. 3. *Changes in the overheating temperature of transistors under pulsed thermal exposure (curve number corresponds to the transistor chip number).*

of each transistor with a power modulated according to a harmonic law and measuring the variable temperature component of all other transistors of the power module. The ratio of the transition temperature amplitudes T_{j1} and power dissipation P_1 determines the modulus of the thermal impedance $Z_T(\nu)$ at the modulation frequency ν, and the ratio of the imaginary Im T_{j1} and the real Re T_{j1} Fourier transform of the transition temperature determines the phase tangent φ(ν) of the thermal impedance. This made it possible to determine both diagonal and off-diagonal elements of the thermal impedance matrix.

If the measurement object has a complex structure and the heat flow propagates through the elements of this structure from the die to the case and further through the radiator to the environment, then the total thermal resistance includes several components, for example, "transition-case", "case-radiator", "radiator-environment". They can be determined by measuring and analyzing the dependence of the real part Re $Z_T(\nu)$ or the phase φ(ν) of the thermal impedance on the modulation frequency

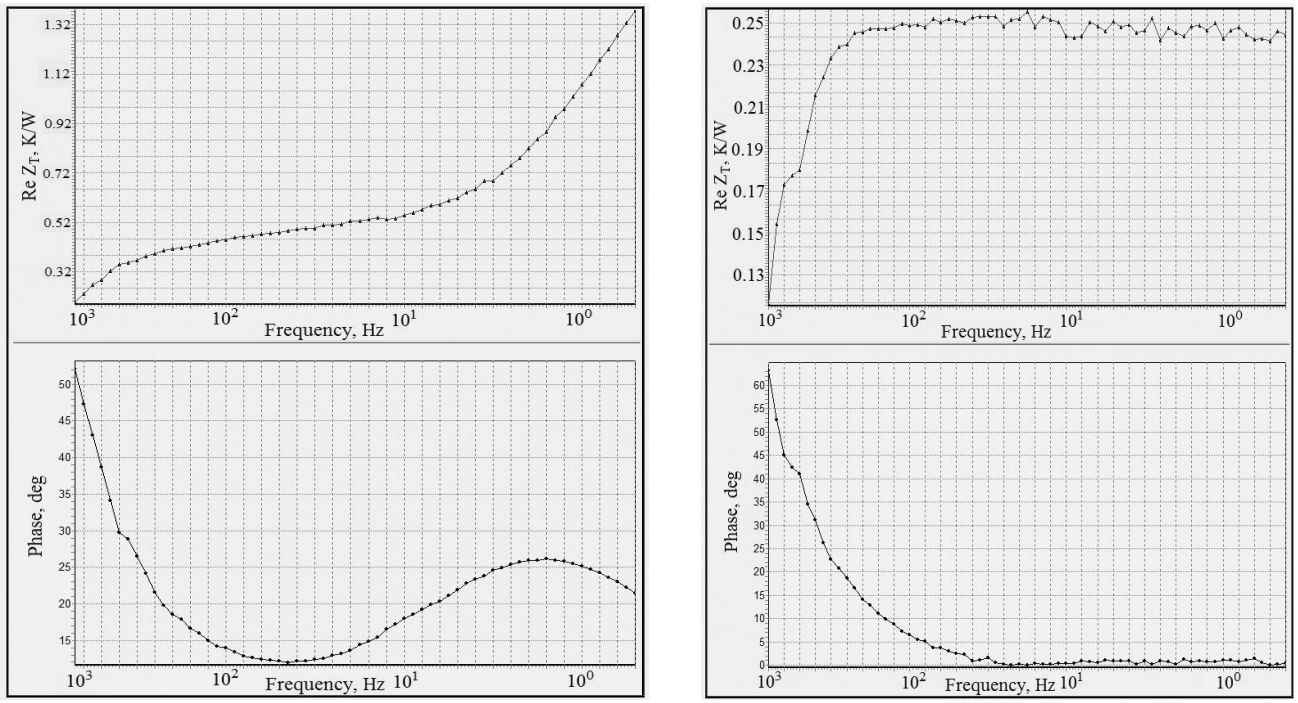

Fig. 4. *Dependence Re $Z_T(\nu)$ (top) and $\varphi(\nu)$ (bottom): a) for Z_{22}; b) for Z_{13}* [10].

of the heating power ν. **Fig. 4***a* shows the results of measuring such dependences for one of the diagonal terms of the thermal impedance matrix Z_{22}, when the heating current pulses were passed through transistor 2, and the junction temperature T_{j1} was also measured for it. Fig. 4*b* shows a similar dependence for the Z_{13} matrix element, when the thermal power was dissipated in transistor 1, and the temperature response was measured for transistor 3. It can be seen that the character of the Re $Z_T(\nu)$ dependence for Z_{13} differs from that for Z_{22}: there is no increase in thermal impedance with a decrease in the modulation frequency to several hertz. In addition, unlike Z_{22}, there is no minimum in the frequency dependence of the phase $\varphi(\nu)$ of the thermal impedance, and the value of the phase itself in a wide frequency range is only a few angular degrees.

In the presence of several thermal resistance components, the dependence Re $Z_T(\nu)$ has features in the form of flat sections or inflection points. To reveal these features, the Re $Z_T(\nu)$ curve was differentiated with respect to the modulation frequency ν. The result of processing $Z_T(\nu)$, which includes the calculation of $(\mathrm{dRe}Z_T/\mathrm{d}\nu)^{-1}$ as a function of $\mathrm{Re}Z_T$, is shown in **Fig. 5**. The components of thermal resistance appear as maxima, the position of which relative to the abscissa axis determines their values. For transistor 2, these components are R_{T1} = 0.495K/W, R_{T2} = 0.532K/W and R_{T3} = 0.596K/W. The results of similar measurements for other transistors of the module differ from each other by no more than 3%.

The sequential heating of all transistors of the module at different frequencies of the heating power modulation and the measurement of the response to this effect made it possible to determine the diagonal and off-diagonal elements of the thermal impedance matrix Z_{Txy} [10]:

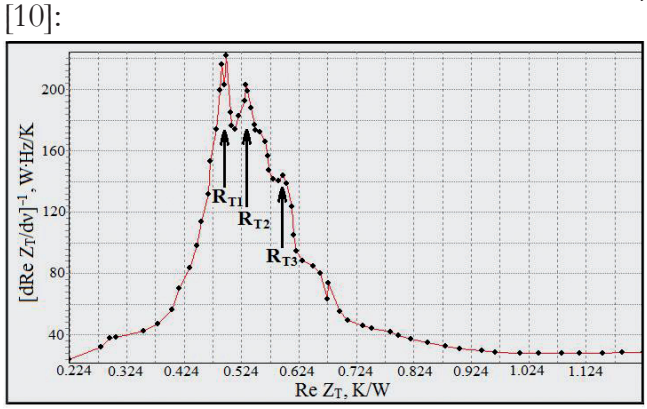

Fig. 5. *Thermal resistance components of power module transistor 2* [10]

$$\mathbf{Z}_{\mathrm{T}xy}=\begin{pmatrix} 0.534+0.102j & 0.263 & 0.243 & 0.268 \\ 0.267 & 0.532+0.104j & 0.273 & 0.263 \\ 0.264 & 0.278 & 0.546+0.103j & 0.268 \\ 0.273 & 0.261 & 0.264 & 0.536+0.100j \end{pmatrix}. \quad (4)$$

Diagonal members of the matrix are complex quantities, the real parts of which determine the components of the thermal resistance "transition – the base of the module" of all transistors of the module. For the off-diagonal terms of the matrix, which determine the thermal cross-links between transistors, the phase does not exceed 2°; therefore, the imaginary part of the off-diagonal terms is practically equal to zero.

Using the elements of the matrix $Z_{\mathrm{T}xy}$ (4), and knowing the power dissipated in certain transistors, it is possible to calculate the die temperature of any transistor of the power module using formula (1). To check this, the 1st and 2nd transistors were simultaneously heated with a power modulated according to a harmonic law, and the overheating temperatures ΔT of all transistors of the module were measured. The results are shown in the first row of Table 1. The second row of **Table 2** shows the results of calculating the overheating temperature based on the measured values of the elements of the thermal impedance matrix $Z_{\mathrm{T}xy}$ and the power dissipation in the 1st and 2nd transistors. The third line shows the simulation results using a numerical method for solving the heat equation. It can be seen that the values of the overheating temperature of all transistors of the power module, obtained by various methods, are in good agreement with each other, which confirms the correctness of the developed thermal model of the power module.

Table 2

The results of measurement and calculation of the module transistors overheating temperature

	ΔT_1, K	ΔT_2, K	ΔT_3, K	ΔT_4, K
Experiment	0.87	0.82	0.63	0.61
Calculation based on $Z_{\mathrm{T}xy}$	0.87	0.84	0.62	0.60
Calculation based on model	0.88	0.86	0.59	0.58

5. CONCLUSION

To study thermoelectric processes in a power module consisting of four high-power MOSFETs, a thermal model based on the solution of the heat equation by the finite element method using the COMSOL Multiphysics software environment is proposed. Within the framework of the model, the calculation of the thermal field was made under the pulsed action of thermal power on a part of the module died. This made it possible to estimate the degree of thermal influence of the dies among themselves and to calculate the overheating temperatures of all the module dies.

To check the reliability of the obtained simulation results, they were compared with results obtained experimentally. As experimental results, the results of measuring the elements of the thermal impedance matrix obtained by the modulation method, as well as the results of direct measurements of the overheating temperature of the dies under the pulsed action of thermal power on individual dies of the module, were used. An analysis of the data obtained allows us to conclude that the calculated and experimental values of the die overheating temperature are in good agreement with each other, therefore, the developed model adequately describes the thermal processes in the considered power module.

REFERENCES

1. Verhulevski KA. Novye silovye moduli kompanii Microsemi na osnove karbida kremiya [New Microsemi Silicon Carbide Power Modules]. *Komponenty i tehnologii,* 2013, 4:138-142 (in Russ.).
2. Thermal Impedance Measurements for Vertical Power MOSFETs (Delta Source-Drain Voltage Method). JEDEC JESD24-3 standard.
3. Aronov VL, Fedotov YA. Issledovanie i ispytanie poluprovodnikovykh priborov [Research and testing of semiconductor devices]. Moscow, Vysshaya shkola Publ, 1975, 325 p.

4. Vyakhirev VB. Izmerenie teplovykh kharakteristik poluprovodnikovykh elektronnykh komponentov [Measurement of thermal characteristics of semiconductor electronic components]. *Tehnologii v elektronnoy promyshlennosti,* 2013, 3:90-92 (in Russ.).
5. Brückner T, Bernet S. Estimation and Measurement of Junction Temperatures in a Three-Level Voltage Source Converter. *IEEE Transactions on Power Electronics,* 2007, 22:3-12.
6. Luo Z, Ahn H, Nokali M. A thermal model for insulated gate bipolar transistor module. *IEEE Transactions on Power Electronics,* 2004, 19:902-907.
7. Yun C, Malberti P, Ciappa M, Fichtner W. Thermal Component Model for Electrothermal Analysis of IGBT Module Systems. *IEEE Transactions on Advanced Packaging*, 2001, 24:401-406.
8. Drofenik U, Kolar JW. Teaching Thermal Design of Power Electronic Systems with Web-Based Interactive Educational Software. *Proc. 18th Annual IEEE Applied Power Electronics Conference and Exposition*, 2003, 1:1029-1036.
9. Davidson JN, Stone DA, Foster MP. Real-time prediction of power electronic device temperatures using PRBS-generated frequency-domain thermal cross-coupling characteristics. *IEEE Transactions on Power Electronics,* 2015, 30:2950-2961.
10. Smirnov VI, Sergeev VA, Gavrikov AA, Shorin AM. Izmereniye perekrestnykh teplovykh soprotivleniy cilovykh modulei. [Measurement of cross thermal resistances of power modules]. *Jurnal Radioelektroniki*, 2019, 7:1-15 (in Russ.).
11. Smirnov VI, Sergeev VA, Gavrikov AA, Shorin AM. Modulation method for measuring thermal impedance components of semiconductor devices. *Microelectronics Reliability,* 2018, 80:205-212.
12. Sadeghi E, Bahrami M, Djilali N. Thermal Spreading Resistance of Arbitrary-Shape Heat Sources on a Half-Space: A Unified Approach. *IEEE Transactions on Components and Packaging Technologies*, 2010, 2:267-277.

DOI: 10.17725/rensit.2023.15.125

Radiometric method for soil moisture portraits obtaining to study the hydrology of dams

Igor A. Sidorov, Alexander G. Gudkov, Sergey V. Chizhikov
Bauman Moscow State Technical University, https://bmstu.ru/
Moscow 105005, Russian Federation
E-mail: igorasidorov@yandex.ru, profgudkov@gmail.com, chigikov95@mail.ru

Evgeny P. Novichikhin
Kotelnikov Institute of Radioengineering and Electronics of RAS, Fryazinsky Branch, http://fire.relarn.ru/
Fryazino 114149, Moscow Region, Russian Federation
E-mail: epnov@mail.ru

Igor O. Porokhov
A.I. Berg Central Scientific-Research Radioengineering Institute, http://www.cnirti.ru/
Moscow 105066, Russian Federation
E-mail: ds4@cnirti.ru.

Received April 11, 2023, peer-reviewed April 18, 2023, accepted April 25, 2023

Abstract: **The methods for the artificial hydraulic structures condition monitoring using trace microwave radiometers are considered, in order to timely detect places of underground leaks to ensure trouble-free operation. Several practical examples of the use of microwave radiometers on various ground-based mobile carriers are described. The characteristics of microwave radiometers used in practice for hydrological monitoring of earthen dams are given. The possibility of detecting potentially dangerous sections of dams, places of erosion of the dam cover, possible places of underground leaks is shown. The possibility of combining microwave radiometers with other means of remote sensing, such as optical video cameras, thermal infrared cameras and georadars, is being considered. The advantages of multisensory sensing to increase the reliability of detecting places of underground leaks are substantiated.**

Keywords: **microwave radiometers, earth dam, remote sensing, radio brightness temperature, relic radiation, unmanned aerial vehicles, soil moisture**

UDC 681.7.069.32

Acknowledgments: The study was carried out at the expense of the grant of the Russian Science Foundation No. 22-19-00063 https://rscf.ru/project/22-19-00063.

For citation: Igor A. Sidorov, Alexander G. Gudkov, Evgeny P. Novichikhin, Sergey V. Chizhikov, Igor O. Porokhov. Radiometric method for soil moisture portraits obtaining to study the hydrology of dams. *RENSIT: Radioelectronics. Nanosystems. Information technologies,* 2023, 15(2):125-132e. DOI: 10.17725/rensit.2023.15.125.

Contents

1. INTRODUCTION

There are examples of the practical use of microwave radiometers to monitor the hydrological situation along pipeline routes [1], to detect oil films on the water surface [2], to monitor the condition of highways

[3], to determine the coordinates of forest and peat fires [4], to determine the moisture content in the productive soil layer for the needs of digital agriculture [5]. This article is devoted to the urgent topic of microwave radiometric monitoring of earthen dams in order to detect places of underground leaks, for timely measures to prevent a catastrophe [6], based on many years of practical experience in the use of microwave radiometers [7-14].

To protect low-lying areas in river valleys and sea coasts from flooding, to regulate water flow for water supply, for agricultural and industrial needs, according to a rough estimate, tens of thousands of kilometers of dams of various types have been built in the world. There are no exact statistics on the total length of dams in the world, only the largest objects included in the register of dams by the International Commission on Large Dams are taken into account. Safe, trouble-free operation of artificial hydraulic structures is an extremely important task, since, as a rule, a dam break leads to catastrophic consequences with significant economic damage, human casualties and serious environmental consequences for the entire region that has been flooded, especially if oil and gas infrastructure facilities, pipelines, production, processing or storage facilities of hydrocarbon products have fallen into the flooding zone. It may take years to eliminate the consequences of the disaster…

The most common cause of a dam break is overflow, which may occur due to the discrepancy between the actual spillway and the calculated values, clogging of the spillway with extraneous debris. The second most common cause of accidents is subsidence of the soil and instability of the slopes of the dam. The third cause of accidents are underground leaks that cause internal erosion of the dam body, the formation of voids with subsequent subsidence or movement of the soil.

Therefore, timely detection of underground leaks in earthen dams with their subsequent elimination of leaks allows preventing possible accidents and catastrophes.

In the Kingdom of the Netherlands, about half of the country's territory has been reclaimed from the sea and is located below sea level. The coastline is formed by alluvial dunes. Behind them are the lands reclaimed from the sea, called polders and protected by dunes and artificial dams from sea waters. The total length of the protective dams exceeds three thousand kilometers. In the Netherlands there is also the longest dam in Europe – Afsleitdijk, thirty kilometers long. The problem of flood protection and water balance regulation is especially relevant in the Netherlands, where a special flood protection department, the Watershap, is organized, which organizes continuous monitoring of artificial hydraulic structures using the most modern remote sensing methods, including the method of microwave radiometry.

The purpose of this work is to show the results of the practical use of microwave radiometers for monitoring the condition of earthen dams, the possibility of searching for places of underground leaks, identifying places with violation of protective coatings of dams and identifying places of erosion of the dam under the protective layer, using various means of transporting radiometers – unmanned aerial vehicles, special machines, quad bike and hand cart.

2. EQUIPMENT AND RESEARCH METHOD

Microwave radiometers designed for remote sensing can be placed on various platforms – space, aviation and ground. Radiometers placed on space satellites, for example, the well-known MIRAS radiometric system developed by the European Space Agency, operating in the L-band with passive aperture synthesis, designed to measure soil moisture and ocean water salinity, the best in its class in many respects, is completely not applicable for detecting leaks in earthen dams, since the system provides the size of the pixel is more than 35 kilometers, which exceeds the length of the longest European dam [7]. Previously, experiments were conducted to detect leakages in earthen dams using a scanning radiometer placed on board the aircraft from a height of 300 meters [1]. The pixel element was approximately 20 meters. This resolution is clearly not enough to accurately determine the coordinates of the leak location. Acceptable resolution, of the order of half a meter, can be provided by trace radiometric systems placed at extremely low altitudes, since the resolution of trace radiometers without synthesis of the antenna aperture is determined by the width of the main beam of the antenna pattern, which is approximately equal to the ratio of the wavelength to the aperture value. Usually, the aperture value of such antennas does not exceed 1-2 wavelengths, which for the *L*-band (wavelength 21 cm) will be about half a meter. This characteristic size determines the minimum dimensions of the radiometer. Radiometers with such dimensions can have a mass of two to twenty kilograms and can be easily placed on an unmanned aerial vehicle, a special road vehicle, an ATV or moved on a trolley. The use of a UAV as a carrier of a microwave

Fig. 1. *Placement of the radiometer on the UAV.*

radiometer (**Fig. 1**) has the advantage that almost any section of the dam becomes available for shooting when movement on the ground is difficult. The disadvantages of this method of movement are the reduced resolution or detail of the sensing. The resolution of the microwave radiometer is equal to the height of the radiometer above the earth's surface. When flying a UAV over a dam to ensure flight safety, the height must be at least 10 meters, respectively, and the permitted element will have a size of about 10 by 10 meters. This is enough to detect places of underground leaks, but it is absolutely not enough to accurately identify places of erosion of dams. When moving the radiometer using a crane (**Fig. 2**), the resolution will be from 1 to 2 meters, depending on the setting of the crane boom, but this value may vary significantly due to road surface irregularities. In addition, a

Fig. 2. *Sounding of the dam using a crane.*

Fig. 3. *A system of two radiometers on an the quad bike.*

bulky crane may not pass everywhere. The placement of the radiometer on the ATV significantly increases the cross–country ability, but the resolution is stable and is 1 meter – the height of the installation of the radiometer (**Fig.3**). But the ATV also cannot always move across the entire surface of the dam. For hard-to-reach places, moving the radiometer on a trolley (**Fig.4**) or carrying it on your hands is used.

The main parameters of the radiometer are presented in **Table 1.**

The method of detecting leaks in dams is based on the fact that a microwave radiometer is able to receive and measure the power of its own radiothermal radiation that originated underground in depth, passed through the rock thickness and radiated into open space. Simultaneously with the radiation of the dam, the radiometer also receives part of the relic radiation of the celestial sphere

Fig. 4. *Moving the radiometer on the trolley.*

Table 1

Radiometer parameters

Parameters	Value
The central frequency of the receiving module, MHz	1412±30
Reception bandwidth, MHz	50 ±20
Number of receiving channels	1
Sensing method	Along flight line
Viewing width, H - height above the ground	1.0xH
Sensitivity, K degree	0.5
Card Type	SD-Card
Continuous recording time, at least an hour	8
Supply voltage, V	12
Power consumption, W max	6
Weight, kg	8.5
Size, mm	500X400X80

reflected from the earth's surface with the addition of its own atmospheric radiation. Radiation can be received simultaneously at one or at different wavelengths (frequency ranges) and at two wave polarizations – vertical and horizontal. The depth of sounding is determined by the selected wavelength, humidity and mineralization of the soil, and usually lies in the range from one to five wavelengths. For dams sensing, it is convenient to use the *L*-band (wavelength 21 cm.), since this ensures sufficient depth of sounding and in this range there is a frequency band (from 1400 to 1427 MHz), specially allocated for the operation of radio astronomers and passive locators. According to the measured values of radio brightness temperatures on the vertical T_{bv} and horizontal T_{bh}, the I_p polarization index is calculated by the formula:

$$I_p = (T_{bv} - T_{bh})/(T_{bv} + T_{vh}).$$

The value of the polarization index weakly depends on the temperature of the soil layer and is mainly determined by the value of the dielectric permittivity of the soil, which depends on the moisture content. The dependence of the polarization index on soil moisture varies under different conditions and depends on the material and

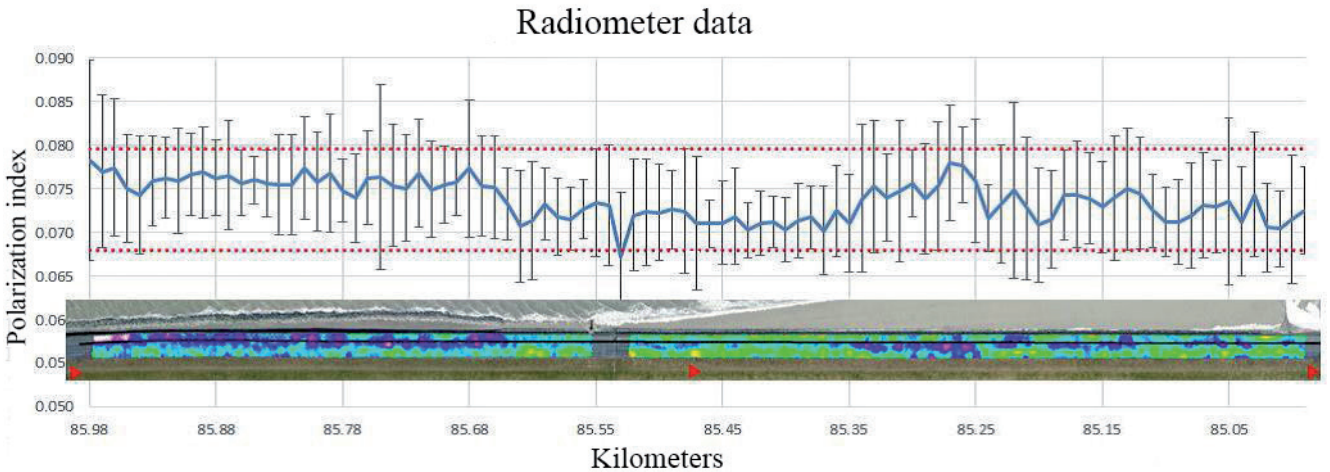

Fig. 5. *The study of the kilometer section of the dam results.*

thickness of the dam coating, the material of the embankment, the presence of vegetation, etc. To accurately determine the radiation-humidity dependence, a special calibration of the radiometric system is required, in relation to specific conditions.

3. DAM SOUNDING RESULTS

A system of two radiometers combined with a satellite navigation system receiver was used to study the asphalt pavement on the Lauwers-Mer dam (Netherlands). The system measures the intensity of its own radiothermal radiation of the underlying surface simultaneously at two polarizations in the L-band, and stores its digital readings together with navigation information. The radio brightness temperatures measured by the system are particularly sensitive to changes in the dam coating material and soil moisture (dielectric properties). For example, the dielectric constant of water is 80, asphalt-about 5, air-1. By measuring the radio brightness temperatures simultaneously in two polarizations, the polarization index is determined as an indicator of the asphalt structure. The graph of the dependence of the polarization index on the longitudinal coordinate obtained during a full-scale experiment on the Lauwers-Mer dam is shown in **Fig. 5**. The same graph shows a fragment of a soil moisture content map constructed from these data along the trajectory of the carrier. On the map, sections of the dam with normal moisture are shown in green, areas with increased moisture are shown in blue, and places with critical waterlogging are shown in purple. Such places were registered, photographed and samples (pits) of asphalt pavement were taken in them in order to identify the causes of waterlogging. Photos of critical places and asphalt samples are shown in **Fig. 6**. During the laboratory examination of the samples, it was revealed

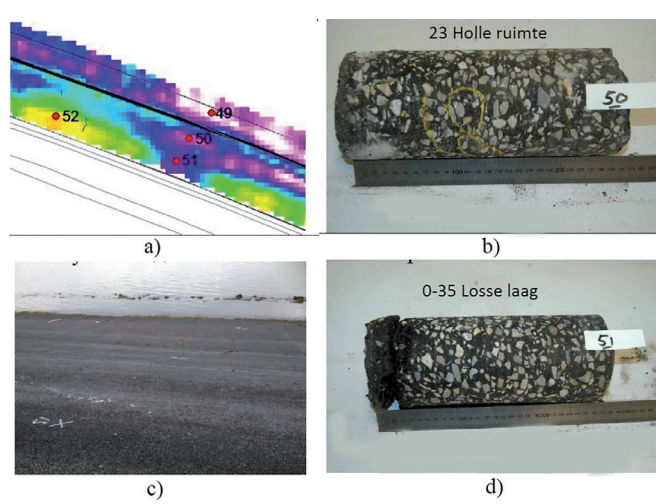

Fig. 6. *A map of the dam site with photos of coating samples at critical points. a) dam moisture map; b) photo of the core at point 50 – emptiness; c) photo of the dam section; d) photo of the core at point 51 – loose structure.*

that the first sample contains internal voids, and the second contains places with a loose asphalt structure. In both cases, the coating is able to effectively protect the dam from external meteorological factors and requires repair. During the experiment, along with radiometric survey, photo and video shooting was performed to document the results, as well as shooting with a thermal infrared camera, the data of which correlates well with radiometer data and complements them with more accurate information about the surface temperature of the dam.

The presence of places with damaged asphalt pavement of the dam, over time, can result in erosion of the dam body, underground leaks, leaching of soil and, as a result, to the formation of voids that can cause soil movement or partial collapse with catastrophic consequences. Microwave radiometers, which are capable of detecting water in the depth of the dam, are completely insensitive to underground voids. But ground-penetrating radars can be successfully used to detect underground voids. Georadar is specialized active radar designed to probe underground objects. The principle of its operation is based on generating and emitting an electromagnetic pulse into the ground through a transmitting antenna and receiving signals reflected from various underground in homogeneities. The reflected pulses are received by the receiving antenna with some delay depending on the distance of the inhomogeneity from the antenna. The complete absence of reflected signals in any range of band means that there is a void in this range. Thus, the combined use of several types of sensors – microwave radiometers, optical cameras, infrared cameras and georadar provides enough data for a comprehensive survey of the condition of dams with recommendations for measures to ensure long-lasting and trouble-free operation.

4. CONCLUSION

As a result of the research carried out, the following conclusions can be made:

- the method of microwave radiometric sensing can be successfully used to monitor the condition of dams, search for places of underground leaks and erosion of the coating;
- an unmanned aerial vehicle, a crane, an ATV or a trolley can be used as a carrier of the radiometer;
- multisensory sensing using, in addition to a microwave radiometer, an optical video camera, a thermal infrared camera and a ground-penetrating radar increases the likelihood of detecting places of underground leaks, erosion of the coating and the presence of underground voids.

REFERENCES

1. Sidorov IA, Gudkov AG, Sister VG, Ivannikova EM, Leushin VY. Monitoring of the hydrological situation along pipeline routes by means of microwave radiometry methods. *Chem. Petrol. Eng.,* 2021, 56, 929-234; doi: 10.1007/s10556-021-00864-6.
2. Gudkov AG, Sister VG, Ivannikova EM, Leushin VY, Plyushchev VA, Sidorov IA, Chetyrkin DY. On the possibility of detecting oil films on water surface by microwave radiometry methods. *Chem. Petrol. Eng.*, 2019, 55:57-62; doi: 10.1007/s10556-019-00580-2.
3. Sidorov IA, Soldatenko AP, Gudkov AG, Leushin VY, Novichikhin E.P. Results of field experiments on monitoring the hydrological situation along highways with a multifrequency polarimetric

system of microwave radiometers. *Mashinostroitel*, 2015, 12:46-55 (in Russ.).

4. Sister, V.G., Ivannikova, E.M., Gudkov, A.G., Leushin, V.Y., Sidorov, I.A., Plyushchev, V.A., Soldatenko, A.P. Detection of forest and peat-bog fire centers by means of microwave radiometer sounding. *Chem. Petrol. Eng.*, 2016, 52:123-125; doi: 10.1007/s10556-016-0160-2.
5. Verba VS, Gulyaev YV, Shutko AM, Krapivin VF. and others (total 45 authors). *Microware Radiometry of Land and Water Surfaces: From Theory to Practice*. Sofia, Marin Drinov Academic Publishing, 2013, 296 p.
6. Jeu RDe, Parinussa R, Biemond L, Haarbrink R, Shutko A, Demontoux F, Provoost Y. Safety inspection of levees with L-band radiometry. *Proc. 11th Specialist Meeting on Microwave Radiometry and Remote Sensing of the Environment, MicroRad-2010*, pp. 96-98. DOI: 10.1109/MICRORAD.2010.5559583.
7. Yashchenko AS, Bobrov PP. Features of SMOS Level 1C data processing in remote sensing tasks. *Modern problems of remote sensing of the Earth from space*. 2017, 14(3):78-91 (in Russ.). DOI: 10.21046/2070-7401-2017-14-3-78-91.
8. Shutko A, Abramov V, Haldin A, Novichikhin E, Krapivin V, Golovachev S, Pliushchev V, Sidorov I, Biriukov E, Haarbrink R, Archer F, Hristov P, Gavrailov E. Sea surface and land-sea contact zones sensing at passive microwaves and in optical band. *ECOLOGICA* (Belgrad), 2009, 55:345-349.
9. Shutko AM, Krapivin VF, Haarbrink RB, Sidorov IA, Novichikhin EP, Archer F, Krissilov AD. *Practical Microwave Radiometric Risk Assesment*. Sofia, Prof. Marin Drinov Publ. House, Bulg. Academy of Sciences, 1910, 100 pp.
10. Archer, F, Shutko A, Coleman TL, Haldin A, Sidorov I, Novichikhin E. Microwave Remote Sensing of Land Surface from Mobile Platform: The Alabama 2003-2005 Experiment. Abstract. To be presented at "*The Int 7IEEE 2006 Geoscience & Remote Sensing Symposium (IGARSS'06)*", Denver, CO, USA, 31 July- 04 August, 2006.
11. Sidorov IA, Gudkov AG, Leushin VYu, Gorlacheva EN, Novichikhin EP, Agasieva SV. Measurement and 3D Visualization of the Human Internal Heat Field by Means of Microwave Radiometry. *Sensors*, 2021, 21(12):4005; doi: 10.3390/s21124005.
12. Vesnin SG, Sedankin MK, Ovchinnikov LM, Gudkov AG, Leushin VYu, Sidorov IA, Goryanin II. Portable microwave radiometer for wearable devices. *Sensors and Actuators A: Physical*, 2021, 318:112506; doi: 10.1016/j.sna.2020.112506.
13. Gudkov AG, Agasieva SV, Sidorov IA, Khokhlov NF, Chernikov AS, Vagapov Yu. A portable microwave radiometer for proximal measurement of soil permittivity. *Computers and Electronics in Agriculture,* 2022, 198:107076. DOI: 10.1016/j.compag.2022.107076.
14. Shutko AM, Haldin A, Krapivin V, Novichikhin E, Sidorov I, Tishchenko Y, Haarbrink R, Georgiev G, Kancheva R, Nikolov H, Coleman T, Archer F, Pampaloni P, Paloscia S, Krissilov A, Carmona A. Microwave radiometry in monitoring and emergency mapping of water seepage and dangerously high ground waters. *Journal of Telecommunications and Information*

Technology, 2007, 1:76-82. Available from: https://www.researchgate.net/publication/228698604_Microwave_radiometry_in_monitoring_and_emergency_mapping_of_water_seepage_and_dangerously_high_ground waters#fullTextFileContent.

DOI: 10.17725/rensit.2023.15.133

Controlling the dynamics of spin polarization of conduction electrons by electrical and mechanical action

Vyacheslav K. Ignatiev, Nikolay G. Lebedev, Sergey V. Perchenko, Dmitry A. Stankevich

Volgograd State University, https://volsu.ru/
Volgograd 400062, Russian Federation
E-mail: vkignatjev@yandex.ru, nikolay.lebedev@volsu.ru, perchenko@volsu.ru, dimon50002004@yandex.ru

Received April 27, 2023, peer-reviewed May 04, 2023, accepted May 11, 2023

Abstract: **A quantum model for the interaction of a collectivized conduction electron with a crystal field in a homogeneous and isotropic deformed polycrystalline sample, taking into account the spin-orbit interaction, is proposed. A dynamic equation of motion of the conduction electron spin in a stress-strained metal is obtained. It is shown that under conditions of inhomogeneous torsion in the stationary case, the average spin of conduction electrons is oriented predominantly along the current density vector. The maximum value of the spin-orbit interaction is observed when the torsion axis is orthogonal to the current density vector.**

Keywords: **spin-orbit interaction, transition metals, Wannier functions, torsion distortion**

PACS: 67.57.Lm, 72.25.Ba, 75.76.+j

Acknowledgments: The study was funded by the Russian Science Foundation grant No. 22-22-20035 (https://rscf.ru/project/22-22-20035/) and the budget of the Volgograd region.

For citation: Vyacheslav K. Ignatiev, Nikolay G. Lebedev, Sergey V. Perchenko, Dmitry A. Stankevich. Control of the dynamics of spin polarization of conduction electrons by electrical and mechanical action. *RENSIT: Radioelectronics. Nanosystems. Information Technologies,* 2023, 15(2):133-138e. DOI: 10.17725/rensit.2023.15.133.

Content

1. INTRODUCTION

One of the directions of modern spintronics is the study of spin fluxes in conductors and semiconductors in order to use these in various kinds of microelectronic devices [1, 2]. In recent decades, a new scientific direction in condensed matter physics has been formed – straintronics, which uses physical effects in matter due to deformations that occur in micro-, nano- and hetero-structures under the action of external controlling fields, leading to a change in the electronic structure, electrical, magnetic , optical and other properties of materials [3]. One of the branches of straintronics is aimed at studying the effect of mechanical stresses on the electronic properties of a substance.

Earlier, within the framework of the created models of a stress-strain ferromagnet, a solution of Landau-Lifshitz-Gilbert type equations was obtained in the form of a dynamic hysteresis loop [4] and it was shown that the crystal field effectively interacts with the spin moments of localized electrons [5], and taking into account the spin-orbit interaction can effectively polarize

conduction electrons in the macroscopic region [6].

In the paper the dynamic control of a polarization by conduction current and torsional strain, which are variable in magnitude and direction, is considers. The novelty of the proposed approach lies in taking into account the interaction with the crystal field of a deformed metal in the model Hamiltonian of collective conduction electrons using relativistic spin-orbit corrections of the second order. Previously, this interaction was not taken into account, since in an unde-formed crystal it does not create a macroscopic coherent polarization of spin currents.

2. MODEL BUILDING

Let us consider the mechanically induced spin polarization of the conduction electron in a homogeneous and isotropic polycrystalline. The interaction of the collective electron with the crystal field is chosen in the form of a spin-orbit interaction with lattice ions, that is, relativistic corrections in the second order of a magnitude $1/c$, where c is the speed of light. The energy of the Coulomb interaction of conduction electrons with each other, as well as with the other electrons of the crystallite, both collective and localized in the ions of the lattice, that is, with the crystal in the framework of the self-consistent field method, is taken into account by replacing its mass with the effective mass m.

Let there are N sites in the crystallite, each of which contains identical ions with an effective charge $+Ze$. Such lattice creates a perturbation of the potential energy of an electron at a point with a radius vector $\mathbf{r}$ and the corresponding electric field

$$\mathbf{E}(\mathbf{r}) = -\frac{eZ}{4\pi\varepsilon_0}\sum_{k=1}^{N}\frac{\mathbf{r}-\mathbf{r}_k}{\left|\mathbf{r}-\mathbf{r}_k\right|^3},$$

where ε_0 is the electrical constant, e is the elementary charge, $\mathbf{r}_k$ is the radius vector of the k-th node of the lattice. The value of the effective charge Z can be estimated by equating the coordinate of the maximum of the hydrogen-like radial wave function to the covalent radius of the atom. For example, for platinum the atomic radius is $1.39\cdot10^{-10}$ m, which for a 6s shell corresponds to $Z \approx 22.45$.

The spin-orbital addition to the electron energy has the form [7]

$$\hat{V} = \frac{\hbar e}{2m^2c^2}\left[\mathbf{E}(\mathbf{r})\times\hat{\mathbf{p}}\right]\hat{\mathbf{s}}, \quad (1)$$

where m is the effective mass of an electron with charge $-e$, where $\hbar$ is the Dirac constant, p and s are the electron momentum and spin operators respectively.

The dynamics of the electron spin, created by perturbation (1), is described by the equa-tion for averages [8]

$$\frac{ds_\alpha}{dt} = \frac{i}{\hbar}\left\langle\left[\hat{V},\hat{s}_\alpha\right]\right\rangle =$$

$$= -\frac{e^2Z\varepsilon_{\alpha\beta\gamma}}{8\pi\varepsilon_0m^2c^2}\sum_{k=1}^{N}\left\langle\left[\frac{\mathbf{r}-\mathbf{r}_k}{\left|\mathbf{r}-\mathbf{r}_k\right|^3}\times\hat{\mathbf{p}}\right]_\beta\hat{s}_\gamma\right\rangle,$$

where $\varepsilon_{\alpha\beta\gamma}$ is the unit asymmetric Levi-Civita tensor. Here and below greek indices denote spatial variables.

We choose the wave function of the collective conduction electron in the form of the Wannier function [9]:

$$\psi(\mathbf{r}) = \frac{1}{\sqrt{N}}\sum_{n=1}^{N}\Psi(\mathbf{r}-\mathbf{R}_n)\exp(i\mathbf{k}\mathbf{R}_n),$$

where $\Psi(\mathbf{r})$ is the hydrogen-like function of an electron, $\mathbf{R}_n$ is the lattice vector.

After summing over the spin variables, setting $\langle\hat{\mathbf{s}}\rangle = \mathbf{s}$ and performing the change of variables $\mathbf{r}-\mathbf{r}_k \to \mathbf{r}$, we obtain the equation

$$\frac{ds_\alpha}{dt} = -\frac{\hbar e^2Z\varepsilon_{\alpha\beta\gamma}}{8\pi\varepsilon_0m^2c^2N}s_\gamma\sum_{n,m,k=1}^{N}\exp\left(i\mathbf{k}\left(\mathbf{R}_n-\mathbf{R}_m\right)\right)\times$$
$$\times\left\langle\Psi\left(\mathbf{r}+\mathbf{r}_k-\mathbf{R}_m\right)\left|\frac{\hat{l}_\beta}{r^3}\right|\Psi\left(\mathbf{r}+\mathbf{r}_k-\mathbf{R}_n\right)\right\rangle, \quad (2)$$

where $\hat{\boldsymbol{l}}$ is the electron orbital momentum operator.

Hydrogen-like functions are small at $r > na_B/Z$, where $a_B = 5.29\cdot10^{-11}$ m is the Bohr

radius and n is the principal quantum number. Therefore, the average on the right side of expression (2) is non-zero only when $\mathbf{R}_n - \mathbf{r}_k = 0$ or a_v and $\mathbf{R}_m - \mathbf{r}_k = 0$ or $\mathbf{a}_v$, where $\mathbf{a}_v$ is a vector drawn to the nearest neighbouring site. Then, taking into account that the orbital momentum operator is Hermitian, we obtain

$$\frac{ds_\alpha}{dt} = -\frac{\hbar e^2 Z \varepsilon_{\alpha\beta\gamma}}{4\pi\varepsilon_0 m^2 c^2} s_\gamma \times$$
$$\times\left\{\cos(\mathbf{ka}_v)\,\mathrm{Re}\left\langle\Psi_v^+\left|\frac{\hat{l}_\beta}{r^3}\right|\Psi\right\rangle + \sin(\mathbf{ka}_v)\,\mathrm{Im}\left\langle\Psi_v^-\left|\frac{\hat{l}_\beta}{r^3}\right|\Psi\right\rangle\right\}.$$

Here, $\Psi_v^{\pm}(\mathbf{r}) = \Psi(\mathbf{r}+\mathbf{a}_v) \pm \Psi(\mathbf{r}-\mathbf{a}_v)$ are functions with parity coinciding (index "+") and with opposite (index "–") parity of the function $\Psi(\mathbf{r})$. The equation implies summation over the index v over pairs of symmetrically located nearest neighbouring sites.

Introducing the wave vector $\mathbf{k} = -\mathbf{j}m/(e\hbar n_e)$, where $\mathbf{j}$ is the charge current density, n_e is the concentration of conduction electrons, we obtain in the first order of smallness in $\mathbf{ka}_v$ the equation of motion of the conduction electron spin:

$$\frac{d\mathbf{s}}{dt} = \left[\{\mathbf{I}-\mathbf{J}\}\times\mathbf{s}\right],$$
$$\mathbf{I} = \frac{\hbar e^2 Z}{4\pi\varepsilon_0 m^2 c^2}\sum_v \mathrm{Re}\left\langle\Psi_v^+\left|\frac{\hat{\mathbf{l}}}{r^3}\right|\Psi\right\rangle, \qquad (3)$$
$$J_\alpha = \frac{eZj_\beta}{4\pi\varepsilon_0 mc^2 n_e}\sum_v a_{v\beta}\,\mathrm{Im}\left\langle\Psi_v^-\left|\frac{\hat{l}_\alpha}{r^3}\right|\Psi\right\rangle.$$

In a non-deformed crystallite, due to the orbital momentum unquench [10], the value $\mathbf{J} = 0$.

3. EQUATION OF SPIN DYNAMICS IN STRESS-STRAIN CRYSTAL

Let us consider an inhomogeneous distortion, in which a point, including a crystal site with coordinate $\mathbf{r}$, is transferred to a new position with coordinate $\mathbf{r}'$ by the displacement vector $\mathbf{u}$, related to the original by known relations [11]

$$r'_\alpha = r_\alpha + u_\alpha, \quad dr'_\alpha = (\delta_{\alpha\beta} + u_{\alpha\beta})\,dr_\beta, \quad u_{\alpha\beta} = \partial_\beta u_\alpha,$$

with the help of which it is easy to obtain shift derivatives:

$$dr_\beta = (\delta_{\alpha\beta} + u_{\beta\alpha})^{-1}\,dr'_\alpha \approx (\delta_{\alpha\beta} - u_{\beta\alpha})\,dr'_\alpha,$$
$$\frac{\partial}{\partial r'_\alpha} = \frac{\partial r_\beta}{\partial r'_\alpha}\frac{\partial}{\partial r_\beta} = \partial_\alpha - u_{\beta\alpha}\partial_\beta.$$

Using shift derivatives, the orbital momentum operator and wave function can be repre-sented as

$$\hat{l}'_\alpha = -i\varepsilon_{\alpha\beta\gamma} r'_\beta \frac{\partial}{\partial r'_\gamma} = \hat{l}_\alpha - i\varepsilon_{\alpha\beta\gamma}\left(u_\beta\partial_\gamma - r_\beta u_{\delta\gamma}\partial_\delta\right), \qquad (4)$$
$$\Psi(\mathbf{r}') = \Psi(\mathbf{r}) + \partial_\alpha\Psi\cdot u_{\alpha\beta} r_\beta.$$

Correspondingly, the orientations of the crystal axes and orbitals of valence electrons change under deformation. With sample torsion strain along the $\mathbf{n}$ axis of the form $\mathbf{\Omega}(\mathbf{r}) = \mathbf{n}(\mathbf{rn})\omega$, where ω is an angle of torsion per unit length, *rad/m*, limited to the first degrees of deformation, we obtain

$$u_\beta = \omega\varepsilon_{\beta\sigma\nu} n_\sigma n_\mu r_\nu r_\mu,$$
$$u_{\delta\gamma} = \omega\varepsilon_{\delta\sigma\nu} n_\sigma n_\mu\left(r_\nu\delta_{\mu\gamma} + r_\mu\delta_{\nu\gamma}\right) =$$
$$= \omega\varepsilon_{\delta\sigma\nu} n_\sigma n_\gamma r_\nu + \omega\varepsilon_{\delta\sigma\gamma} n_\sigma n_\mu r_\mu,$$
$$\hat{\mathbf{l}}' = \hat{\mathbf{l}} + \omega(\mathbf{nr})\left[\mathbf{n}\times\hat{\mathbf{l}}\right] + \omega\left[\mathbf{n}\times\mathbf{r}\right](\mathbf{n}\hat{\mathbf{l}}),$$
$$\hat{l}'_\alpha = \hat{l}_\alpha + \omega\varepsilon_{\alpha\beta\gamma} n_\beta n_\delta\left(r_\delta\hat{l}_\gamma + r_\gamma\hat{l}_\delta\right),$$
$$\Psi(\mathbf{r}') = \Psi(\mathbf{r}) + i\mathbf{\Omega}(\mathbf{r})\hat{\mathbf{l}}\Psi(\mathbf{r}) =$$
$$= \Psi(\mathbf{r}) + i\omega n_\beta n_\delta r_\delta\hat{l}_\beta\Psi(\mathbf{r}).$$

In the approximation linear in ω, taking into account the Hermiticity of the orbital momentum operator and the commutation relations

$$\left[\hat{l}_\alpha, \hat{l}_\beta\right] = i\varepsilon_{\alpha\beta\gamma}\hat{l}_\gamma, \qquad \left[\hat{l}_\alpha, r_\beta\right] = i\varepsilon_{\alpha\beta\gamma} r_\gamma$$

we obtain expressions for the averages

$$\left\langle\Psi'_v\middle|\Psi'\right\rangle - \left\langle\Psi_v\middle|\Psi\right\rangle = i\omega n_\beta n_\delta\left\langle\Psi_v\middle|r_\delta\hat{l}_\beta - \hat{l}_\beta r_\delta\middle|\Psi\right\rangle =$$
$$= \omega\varepsilon_{\beta\delta\gamma} n_\beta n_\delta\left\langle\Psi_v\middle|r_\gamma\middle|\Psi\right\rangle = 0,$$
$$\left\langle\Psi'_v\middle|\hat{l}'_\alpha\middle|\Psi'\right\rangle - \left\langle\Psi_v\middle|\hat{l}_\alpha\middle|\Psi\right\rangle =$$
$$= \omega n_\beta n_\delta\left\langle\Psi_v\middle|\hat{l}_\alpha r_\delta\hat{l}_\beta - \hat{l}_\beta r_\delta\hat{l}_\alpha + \varepsilon_{\alpha\beta\gamma} r_\delta\hat{l}_\gamma + \varepsilon_{\alpha\beta\gamma} r_\gamma\hat{l}_\delta\middle|\Psi\right\rangle =$$
$$= 2\omega\varepsilon_{\alpha\beta\gamma} n_\beta n_\delta\left\langle\Psi_v\middle|r_\gamma\hat{l}_\delta\middle|\Psi\right\rangle.$$

Let us substitute these relations into the formula for the operator **J** in the equation (3):

$$J_{\alpha'} = \frac{\omega e Z}{2\pi\varepsilon_0 mc^2 n_e}\varepsilon_{\alpha'\beta'\gamma'} n_{\beta'} n_{\delta'} j_{\sigma'} \sum_{\nu} a_{\nu\sigma'}\, \mathrm{Im}\left\langle \Psi_\nu^- \left| \frac{r_{\gamma'}\hat{l}_{\delta'}}{r^3} \right| \Psi \right\rangle. \quad (5)$$

The relation (5) is written in the coordinate system associated with the axes of the crystallite. Let us introduce a laboratory coordinate system associated with instruments that set the conduction current and distortion and measure the spin components. The components of vectors and tensors in the laboratory system will be denoted by non-primed indices, but in the coordinate system, associated with the crystal axes, by prime marks.

Let us transform the vectors of current density and torsion axes from the laboratory system into the system of crystal axes $j_{\sigma'} = p_{\sigma'\sigma} j_\sigma$, $n_{\delta'} = p_{\delta'\delta} n_\delta$, and the vectors **I** and **J** from the system of crystal axes into the laboratory one $J_\alpha = p^{-1}_{\alpha\alpha'} J_{\alpha'}$, where $p_{a'a}$ is a unitary rotation matrix, which is conveniently expressed in terms of Euler angles. Substituting this transformation into equation (3) and averaging the vector **s** in the macroscopic region over random orientations of crystallites:

$$\frac{d\overline{\mathbf{s}}}{dt} = \left[\left\{\overline{\mathbf{I}} - \overline{\mathbf{J}}\right\} \times \overline{\mathbf{s}}\right] + \overline{\left[\left\{\delta\mathbf{I} - \delta\mathbf{J}\right\} \times \delta\mathbf{s}\right]}$$
$$\delta\mathbf{I} = \mathbf{I} - \overline{\mathbf{I}}, \quad \overline{\delta\mathbf{I}} = 0, \quad \delta\mathbf{J} = \mathbf{J} - \overline{\mathbf{J}}, \quad \overline{\delta\mathbf{J}} = 0. \quad (6)$$

Here the overline means averaging over random orientations of crystallites,

$$\overline{I}_\alpha = \frac{\hbar e^2 Z}{4\pi\varepsilon_0 m^2 c^2}\, \overline{p^{-1}_{\alpha\alpha'}} \sum_{\nu} \mathrm{Re}\left\langle \Psi_\nu^+ \left| \frac{\hat{l}_{\alpha'}}{r^3} \right| \Psi \right\rangle,$$

$$\overline{J}_\alpha = \frac{\omega e Z}{2\pi\varepsilon_0 mc^2 n_e}\varepsilon_{\alpha'\beta'\gamma'}\, \overline{p^{-1}_{\alpha\alpha'} p_{\beta'\beta} p_{\sigma'\sigma} p_{\delta'\delta}}\, n_\beta n_\delta j_\sigma \times$$
$$\times \sum_{\nu} a_{\nu\sigma'}\, \mathrm{Im}\left\langle \Psi_\nu^- \left| \frac{r_{\gamma'}\hat{l}_{\delta'}}{r^3} \right| \Psi \right\rangle. \quad (7)$$

Analytical averaging of equations (7) leads to

$$\overline{\mathbf{I}} = 0, \quad \overline{\mathbf{J}} = \omega K \left[\mathbf{n} \times \left[\mathbf{n} \times \mathbf{j}\right]\right],$$
$$K = \frac{eZ}{12\pi\varepsilon_0 mc^2 n_e} \sum_{\nu} \mathrm{Im}\left\langle \Psi_\nu^- \left| \mathbf{a}_\nu \frac{\left[\mathbf{r} \times \hat{\mathbf{l}}\right]}{r^3} \right| \Psi \right\rangle. \quad (8)$$

The maximum value of **J** is obtained when the torsion axis is orthogonal to the current density vector. In this case

$$\overline{\mathbf{J}} = -\omega K \mathbf{j}. \quad (9)$$

It follows from Eq. (3) that the spin modulus of a single electron is conserved in a non-deformed crystallite. Equation (6) shows that in the presence of inhomogeneous distortion, the modulus of the spin averaged over the sample is not conserved due to the second term on the right side. Therefore, it can be considered as a relaxation one and, by analogy with the Bloch-Bloembergen equation, can be written as

$$\overline{\left[\left\{\delta\mathbf{I} - \delta\mathbf{J}\right\} \times \delta\mathbf{s}\right]} = -\frac{\overline{\mathbf{s}} - \overline{\mathbf{s}}_e}{\tau}, \quad (10)$$

where $\overline{\mathbf{s}}_e$ is the equilibrium value of the spin averaged over the sample, τ is the longitudinal relaxation time. In this case, the steady state in (6) corresponds to the orientation of the average spin parallel or antiparallel to the vector $\overline{\mathbf{J}}$. Averaging the perturbation (1) over the quantum state and over random orientations of crystallites, similarly to the averaging of its commutator, we obtain that the energy of the states when the average spin is oriented parallel or antiparallel to the vector $\overline{\mathbf{J}}$ is $\pm\hbar\left|\overline{\mathbf{J}}\right|/2$, respectively.

Then, at a finite temperature T, taking into account the formula (9), we write the equilibrium value of the spin averaged over the sample in the equation (10) in the form:

$$\overline{\mathbf{s}}_e = -\frac{\mathbf{j}}{2j}\,\mathrm{th}\left(\frac{\hbar\omega K j}{2k_B T}\right),$$

where k_B is the Boltzmann constant. Thus, the equation for the dynamics of the average electron spin (6) takes the form

$$\frac{d\overline{\mathbf{s}}}{dt} = -\omega K\left[\mathbf{j} \times \overline{\mathbf{s}}\right] - \tau^{-1}\left(\overline{\mathbf{s}} + \frac{\mathbf{j}}{2j}\,\mathrm{th}\left(\frac{\hbar\omega K j}{2k_B T}\right)\right). \quad (11)$$

In the steady-state case, the average spin of the conduction electrons over a polycrystalline sample will be oriented predominantly along the current density vector **j**, as was shown earlier in [6].

For an *s*-electron with $l = 0$ in the relation (8), all integrals are equal to zero. In transition metals, the *s* and *p* bands overlap [10]. Therefore, collective conduction electrons can be formed from *p*-state electrons. In a crystallite, the axis of localization of the maximum electron density of the *p*-electron will be oriented in the direction of the v-pair of nearest neighbours, that is, along the vector $\mathbf{a}_v$. Let us direct the polar axis z along the vector $\mathbf{a}_v$ and count the azimuthal angle φ from the plane $\mathbf{a}_v\mathbf{r}$. Then the wave function of the electron can be represented as:

$$\Psi(\mathbf{r}) = i\sqrt{\frac{3}{4\pi}}R_{n1}(r)\cos(\theta),$$

where $R_{n1}(r)$ is is the *p*-electron radial wave function, θ is the polar angle. Then from the formula (8) follows the form of the coefficient *K*:

$$K = \frac{\hbar eZa}{24\pi\varepsilon_0 mc^2 n_e}\int_0^\infty R_{n1}(x)\,dx \times$$

$$\times\int_0^1 \{R_{n1}(x_1) - R_{n1}(x_2)\}(1-y^2)\,dy,$$

where **a** is the distance to the nearest neighbours,

$$x = Zr/a_B, \quad b = Za/a_B, \quad y = \cos\theta,$$

$$x_1 = \sqrt{x^2 + b^2 + 2xby}, \quad x_2 = \sqrt{x^2 + b^2 - 2xby}.$$

4. CONCLUSION

The resulting equation of motion (11) demonstrates the dynamic effect of controlling the spin polarization of conduction electrons with the inhomogeneous deformation of the metal. The resulting equations are valid for a wide class of crystals with strong spin-orbit interaction, for example, for platinum, etc. The effect can find application in a number of branches of modern spintronics.

Thus, over last 3 years, it have appeared a number of experimental works in which the discovered effects of spintronics and spincaloritronics have not yet been explained: controlling the direction of the heat flux by the magneto-thermoelectric effect in a deformed metal magnet [12], expansion of the temperature range of heat pumping using elastocaloric effect [13], anomalous Righi-Leduc effect in ferromagnetic materials [14]. The dynamic effect presented in this paper can form the basis of the theory of new effects of strain spintronics.

REFERENCES

1. Fetisov YuK, Sigov AS. Spintronika: fizicheskie osnovu i ustroistva [Spintronics: physical foundations and devices]. *RENSIT: Radioelectronics. Nanosystems. Information technologies*, 2018, 10(3):343-356e. DOI: 10.17725/rensit.2018.10.343.
2. Bebenin NG. Effect of electric current on the spin polarization of electrons in materials with inhomogeneous magnetization. *JETP*, 2022, 161(5):737-745.
3. Bukharaev A.A., Zvezdin A.K., Pyatakov, Fetisov Yu.K. Straintronics: a new trend in micro- and nanoelectronics and material science. *Phys. Usp.*, 2018, 61:1175 – 1212.
4. Ignatiev V.K., Lebedev N.G., Orlov A.A. Quantum model of a hysteresis in a single-domain magnetically soft ferromagnetic. *Journal of Magnetism and Magnetic Materials*, 2018, 446:135-142.
5. Ignatiev V.K., Lebedev N.G., Orlov A.A., Perchenko S.V. Quantum model for studying magneto-mechanical properties of a magnetically soft ferromagnet. *Journal of Magnetism and Magnetic Materials*, 2020, 494:165658.
6. Ignatiev V.K., Lebedev N.G., Stankevich D.A. The effect of the spin polarization control of conduction electrons through the deformation of a ferromagnet. *Technical Physics Letters,* 2022, 48(12):25-28.
7. Berestetskii VB, Pitaevskii LP, Lifshitz EM. *Teoreticheskaya fizika. T. IV. Kvantovaya electrodinamika* [Course of Theoretical Physics, Vol. 4, Quantum Electrodynamics]. Moscow, Fizmatlit Publ., 2002, 720 p.
8. Landau LD, Lifshitz EM. *Teoreticheskaya fizika. T. III. Kvantovaya mehanika. Nerelyativ-istskaya*

teoriya [Course of Theoretical Physics, Vol. 3, Quantum Mechanics. Non-relativistic Theory]. Moscow, Fizmatlit Publ., 2004, 800 p.

9. Madelung O. *Teoiriya tverdogo tela* [Theory of solid states]. Moscow, Nauka Publ., 1980, 416 p.
10. Krinchik GS. *Fizika magnitnyx yavlenij* [Physics of magnetic phenomena]. Moscow, MGU Publ., 1976, 367 p.
11. Landau LD, Lifshitz EM. *Teoreticheskaya fizika. T. VII. Teoriya uprugosti* [Course of Theoretical Physics, Vol. 7, Theory of Elasticity]. Moscow, Fizmatlit Publ., 2003, 264 p.
12. Ota S, Uchida K-I, Iguchi R, Thach PV, Awano H, Chiba D. Strain-induced switching of heat current direction generated by magneto-thermoelectric effects. *Scientific Reports*, 2019, 9:13197.
13. Snodgrass R, Erickson D. A multistage elastocaloric refrigerator and heat pump with 28 K temperature span. *Scientific Reports,* 2019, 9:18532.
14. Zhou D.-K., Xu Q.-L., Yu X.-Q., Zhu Z.-G., Su G. Identification of spin effects in the anomalous Righi–Leduc effect in ferromagnetic metals. *Scientific Reports,* 2020, 10:11732.

DOI: 10.17725/rensit.2023.15.139

Development of AUC diagrams for analysis of interhemispheric asymmetry of amplitude-frequency characteristics of EEG to detect delayed cerebral ischemia induced by non-traumatic subarachnoid hemorrhage

Olga S. Sushkova, Alexei A. Morozov, Ivan A. Kershner

Kotelnikov Institute of Radioengineering and Electronics of RAS, http://www.cplire.ru/

Moscow 125009, Russian Federation

E-mail: o.sushkova@mail.ru, morozov@cplire.ru, ivan.kershner@gmail.com

Irina V. Okuneva, Mikhail V. Sinkin

Sklifosovsky Research Institute for Emergency Medicine, Department of Emergency Neurosurgery, https://sklif.mos.ru/

Moscow 129090, Russian Federation

E-mail: okunevaiv@mail.ru, mvsinkin@gmail.com

Received May 28, 2023, peer-reviewed June 05, 2023, accepted June 12, 2023.

Abstract: **The article describes a new type of AUC diagrams intended for the analysis of interhemispheric asymmetry of amplitude-frequency characteristics of electroencephalograms (EEG) of patients with subarachnoid hemorrhage, as well as a new type of head maps named maps of interhemispheric asymmetry of EEG. AUC diagrams are a new statistical tool for identifying regularities in biomedical signals. The idea of AUC diagrams is to visually represent the dependence of the area under the ROC curve (AUC) when comparing data samples from the bounds of the range of given characteristic of this data, for example, frequency or amplitude, etc. The article demonstrates that this principle of data analysis allows us to identify some signs of postoperative complications that may occur in patients undergoing intensive care unit. It is known that the signs of such complications are changes in the amplitude and frequency of EEG oscillations in the neurophysiological frequency ranges delta, theta, alpha, and beta; however, amplitude changes can be caused by other reasons including the state of sleep and exposure to pharmacological drugs. Changes in the amplitude caused by postoperative complications can be revealed by analysis of the interhemispheric asymmetry of the patient's EEG. The developed type of AUC diagrams and interhemispheric EEG asymmetry maps help to automate such EEG analysis. The effectiveness of the developed statistical tools was demonstrated by the analysis of data in two patients with clinically confirmed delayed cerebral ischemia induced by subarachnoid hemorrhage.**

Keywords: **AUC diagrams, ROC analysis, EEG, EEG frequency ranges, interhemispheric asymmetry, head maps, interhemispheric asymmetry maps, delayed cerebral ischemia, subarachnoid hemorrhage, biomedical signals**

UDC 519.67, 612.1, 53.083, 519.24, 004.93

Acknowledgments: The authors thank Prof. Yuri Vladimirovich Obukhov for constructive criticism and assistance in research. The research was supported by the Russian Science Foundation, grant No. 22-69-00102, https://rscf.ru/en/project/22-69-00102/.

For citation: Olga S. Sushkova, Alexei A. Morozov, Ivan A. Kershner, Irina V. Okuneva, Mikhail V. Sinkin Development of AUC diagrams for analysis of interhemispheric asymmetry of amplitude-frequency characteristics of EEG to detect delayed cerebral ischemia induced by non-traumatic subarachnoid hemorrhage. *RENSIT: Radioelectronics. Nanosystems. Information Technologies,* 2023, 15(2):139-152e. DOI: 10.17725/rensit.2023.15.139.

Contents

1. INTRODUCTION

Delayed cerebral ischemia is a dangerous complication that can occur in the patient a few days after surgical treatment for non-traumatic subarachnoid hemorrhage. Delayed cerebral ischemia causes an immediate threat to the patient's life. Timely diagnosis of this complication is an urgent medical problem. One of the methods for diagnosing delayed cerebral ischemia is continuous monitoring of the patient's condition using electroencephalography (EEG). Currently, EEG analysis is carried out by a doctor. At the same time, the automatic detection of signs of delayed ischemia according to EEG data is considered an open scientific problem. The automation of EEG analysis is a complex problem because the EEG signs of delayed ischemia can be caused by other reasons. For example, an increase in EEG amplitude in the delta frequency band can occur during a patient's sleep, and signs of epileptiform activity can be easily confused with EEG artifacts that occur during chewing. This study aims to create new statistical methods that help to identify EEG signs of delayed cerebral ischemia and automate the continuous analysis of EEG.

The first scientific works that demonstrated the relationship between electrical processes in the cerebral cortex and the work of the circulatory system were made even before the advent of electroencephalography at the end of the 19th century [1]. Even then, researchers noted the complexity of the studied phenomena and the inconsistency of the results of experiments on animal models. After the invention of EEG in 1924 [2], numerous works were published indicating that EEG in different neurophysiological frequency ranges reacts differently to changes in blood flow velocity and the level of blood oxygenation. The fundamental papers of Japanese researchers [3,4] summarized the results of experimental studies and served as the basis for further study in this area. The experimental results described in the neurophysiological literature indicate the possibility of diagnosing delayed cerebral ischemia after subarachnoid hemorrhage using EEG [5-13]. At the same time, however, the problem of clinical diagnosis of delayed ischemia differs from the problem of group analysis of patients. This is caused by different EEG recording conditions leading to a large number of EEG artifacts, individual characteristics of patients, and the need for decision-making on changing the treatment regimen. Currently, EEG is considered a promising tool for diagnosing delayed ischemia but the creation of automatic diagnostic systems requires further research [9].

The most popular regularities of EEG changes caused by delayed cerebral ischemia described in the literature are the increase in the amplitude of the delta rhythm and the decrease in the amplitude of the alpha rhythm [4-6]. The EEG power spectral density (PSD) ratio in the delta and alpha frequency ranges is also widely used [14-16]. The use of the delta/alpha PSD ratio is appropriate when comparing groups of patients because it allows us to increase group differences by combining two regularities of opposite directions in one parameter. However, it should be noted that the problem of identifying regularities in patient groups is fundamentally different from the problem of clinical diagnosis of patients. The use of delta/alpha PSD ratio for individual patient diagnosis may cause erroneous results because the patterns of changes in alpha and delta rhythms may differ in different patients. In particular, in some patients, the alpha rhythm may be absent, which makes the delta/alpha PSD ratio mathematically incorrect.

In studies of EEG in delayed cerebral ischemia, the comparison of the EEG amplitude before and after the onset of ischemia was mainly carried out. Unfortunately, in clinical practice, it is not always possible to start EEG monitoring of a patient immediately after surgery. As a result, the doctor does not have EEG data that could be used to compare the EEG amplitude in case of suspected symptoms of delayed ischemia, which complicates the operational diagnosis based on the regularities described in the literature. Nevertheless, even in this case, signs based on the asymmetry of the EEG amplitude in the affected and contralateral hemispheres can be used for rapid diagnosis. The presence of interhemispheric EEG differences in patients with delayed ischemia is described in [3-6].

The problem of diagnostics based on EEG data obtained on the day of the onset of ischemia can be solved by visualizing interhemispheric EEG differences. One of the means of visual representation of EEG is the head map. Usually, the head map is a two-dimensional diagram on which the EEG amplitude values are displayed in a given frequency range on all EEG electrodes using a color scale (see an example in **Fig. 1**).

Head maps are a useful tool for diagnosing delayed cerebral ischemia if the software implementation of head maps allows displaying the average EEG amplitude over a sufficiently long time (for example, a day). The disadvantage of standard head maps is that different EEG trends are mixed and superimposed on the same diagram even if they are statistically independent. For example, different forms of interhemispheric asymmetry can be observed on different groups of electrodes; the head map will display the overall picture of the EEG amplitude for the entire considered time interval. In addition, all EEG artifacts, which can be quite significant, are also superimposed

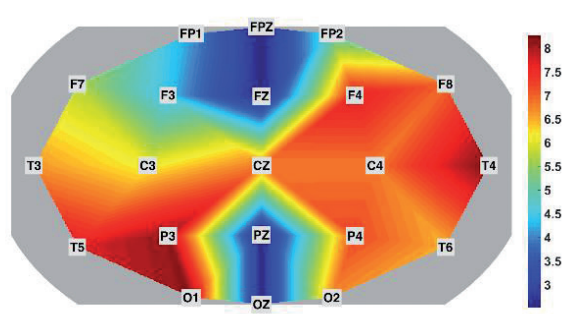

Fig. 1. *An example of a standard head map of* **a patient** *with delayed cerebral ischemia. The delta frequency range (2-4 Hz) is considered. The displayed value is the square root of the median of the square of the instantaneous EEG amplitude over 19 hours. The value is indicated using a color scale. On the head map, various trends in EEG changes are observed simultaneously as well as EEG artifacts. However, based on the head map, it can be concluded that there is interhemispheric EEG asymmetry in the delta frequency range.*

on the overall picture, which complicates the correct interpretation of EEG data. In this paper, we propose statistical tools based on AUC diagrams and the principal component analysis (PCA) that allows us to eliminate these shortcomings of standard EEG head maps. The idea of AUC diagrams is to visually represent the dependence of the area under the ROC curve (AUC) when comparing data samples from the boundaries of the range of given characteristic of this data, for example, frequency. The article proposes a new type of AUC diagram designed to identify interhemispheric EEG differences. The principal component analysis allows us to separate the components of the EEG signals, which are characterized by a correlated change in the signals in some groups of electrodes.

Another problem in using EEG to diagnose delayed cerebral ischemia is the choice of frequency ranges for analysis. The fact is that different authors use different boundaries of the neurophysiological frequency ranges delta, theta, alpha, and beta. Thus, there is an objective problem of determining and verifying the boundaries of the frequency ranges in which the manifestation of the regularities described in the literature on the diagnosis of delayed ischemia using EEG is expected. Frequency ranges must be substantiated and experimentally confirmed. In this work, AUC diagrams are used for this aim.

The article analyzes EEG data of two patients with clinically confirmed delayed cerebral ischemia induced by subarachnoid hemorrhage. Head maps of both patients showed similar patterns of interhemispheric EEG asymmetry in the delta, theta, alpha, and beta frequency ranges. Such asymmetry is not observed in patients before and after delayed ischemia as well as in patients from the control group.

2. DEVELOPMENT OF AUC DIAGRAMS FOR ANALYSIS OF INTERHEMISPHERIC EEG ASYMMETRY

2.1. Principles of constructing and reading AUC diagrams

The idea of AUC diagrams was proposed by the authors for the analysis of wave train electrical activity of the brain in the framework of the problem of diagnosing neurodegenerative diseases [17-21]. In this paper, the method of analyzing wave train electrical activity is not used; however, the principles of constructing and reading AUC diagrams remain the same. The EEG recording is divided into short segments (for example, 10 minutes each). We go through all possible combinations of values of the lower and upper bounds of the EEG frequency range. The average signal amplitude is calculated for each considered frequency range, for each EEG segment, and for each EEG electrode. For each considered frequency range, a matrix is formed:

$$M = \begin{bmatrix} a_{11} & \dots & a_{1k} \\ \dots & \dots & \dots \\ a_{m1} & \dots & a_{mk} \\ \hline b_{11} & \dots & b_{1k} \\ \dots & \dots & \dots \\ b_{m1} & \dots & b_{mk} \end{bmatrix},$$

where a_{ij} is the value of the average EEG amplitude in the considered frequency range in an electrode on the left side of the scalp; b_{ij} is the value of the average EEG amplitude in the considered frequency range in an electrode on the right side of the scalp; k is the number of pairs of symmetrical EEG electrodes; m is the number of short (10 minutes) EEG segments. The principal components of the M matrix are calculated using PCA. The number of components corresponds to the number of pairs of symmetrical electrodes. The projection of the M matrix onto the principal

components is calculated. As a result, *k* vectors are obtained; each vector includes *m* projections of amplitude values in the left hemisphere and *m* projections of amplitude values in the right hemisphere. The ROC curve for comparison of amplitude projection values in the left and right hemispheres is calculated. The area under the ROC curve (AUC) is calculated for a chosen principal component. The AUC values for all considered frequency ranges for the selected PCA component are displayed in the form of a two-dimensional diagram (AUC diagram).

Fig. 2 demonstrates an example of an AUC diagram of a patient with delayed ischemia after a subarachnoid hemorrhage corresponding to the first component of PCA. It is advisable to read the AUC diagram as follows. Let's consider monochromatic color areas adjacent to the diagonal of the AUC diagram. There are two large solid color areas in the diagram; one is cyan and the other is orange. The separation point of these regions, which is closest to the diagonal, approximately corresponds to the frequency of 6 Hz along the abscissa and ordinate axes. The cool colors (blue and cyan) on the diagram correspond to the AUC values < 0.5; the warm colors (red and yellow) correspond to AUC values > 0.5. Therefore, at frequencies below 6 Hz, the average EEG amplitude in the left hemisphere is less than in the right hemisphere, and at frequencies above 6 Hz, the average EEG amplitude, on the contrary, is greater in the left hemisphere. Thus, this patient has a multidirectional interhemispheric asymmetry of the EEG amplitude in different frequency ranges, which corresponds to the regularities of EEG changes in delayed cerebral ischemia described in the literature.

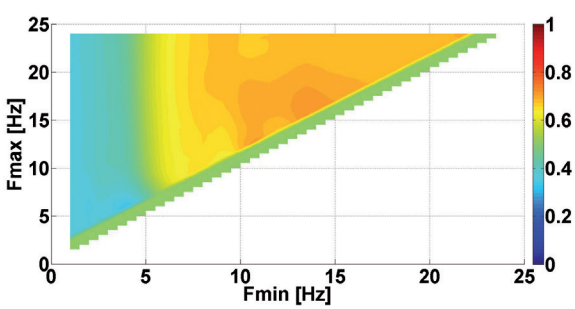

Fig. 2. *An example of an AUC frequency diagram of EEG of* **a patient** *with delayed cerebral ischemia. The displayed value is AUC when comparing the amplitudes of EEG fragments (daily EEG record is divided into 10-minute fragments) in the left and right hemispheres in the frequency range* [F_{min}, F_{max}], *where* F_{min} *is the lower bound of the frequency range, which is indicated by the abscissa, and* F_{max} *is the upper bound of the frequency range, which is indicated by the ordinate. The EEG amplitudes on all pairs of symmetrical electrodes are considered. To reduce the data of all electrodes to a single value, the projection of the amplitude values on* **the first** *component of PCA is calculated. The values are indicated using a color scale. On the AUC diagram, two solid areas are observed: cyan and orange. This is a consequence of the fact that the patient has opposite trends in interhemispheric EEG asymmetry in different frequency ranges.*

According to the literature, it can be expected that the revealed asymmetry of the EEG amplitude can be manifested differently in the areas of the scalp corresponding to different EEG electrodes. The degree of generalization of the revealed differences in the EEG amplitude is also important. To study these issues, we use interhemispheric asymmetry maps, which indicate the values of the PCA coefficients for different EEG electrodes.

2.2. Evaluation of the generalization degree of interhemispheric EEG differences

Interhemispheric asymmetry maps (IAMs) differ from standard head maps in that they reflect the degree of amplitude asymmetry between the corresponding pairs of EEG electrodes in the left and right hemispheres. The degree of asymmetry is displayed using a color scale. Gradations of red and yellow colors indicate electrodes where increased EEG amplitude is observed in comparison with the corresponding electrodes in the contralateral hemisphere. Electrodes in

the contralateral hemisphere are indicated by gradations of blue. IAM is always symmetrical along the vertical axis up to color inversion. This is a consequence of the fact that the information about the cause of the observed asymmetry is discarded. For instance, if the EEG amplitude is greater than normal in the right hemisphere, IAM looks the same as if the EEG amplitude is less than normal in the left hemisphere. This property of IAM allows us to focus on the properties of EEG interhemispheric asymmetry and abstract from the absolute value of the EEG amplitude. If necessary, the doctor can obtain comprehensive information about the EEG amplitude using standard head maps or by directly studying the EEG signals.

Another difference between IAM and standard head maps is that IAM corresponds to a single selected principal component of PCA. Thus, several IAMs correspond to one standard head map in the selected frequency range. When analyzing a patient's EEG, only IAMs corresponding to front components of PCA are usually used because they reflect the most substantial interhemispheric differences. Unfortunately, it is impossible to predict in advance which IAM contains useful diagnostic information. The fact is that some IAMs may correspond to EEG artifacts. Such IAMs are usually easy to recognize by their characteristic appearance which allows us to exclude the influence of EEG artifacts from the analysis and extract important information for the diagnosis of delayed ischemia.

Let us consider an example of IAM of a patient with delayed cerebral ischemia (**Fig. 3**). This IAM corresponds to the first component of PCA in the delta frequency range (2-4 Hz). Interhemispheric EEG asymmetry in the delta frequency range, generalized over the entire surface of the scalp is observed in IAM. Notably, interhemispheric differences are observed in the frontal area of the cortex including electrodes F3 and F4. A possible reason for this difference is that the affected brain region is located near the F4 electrode.

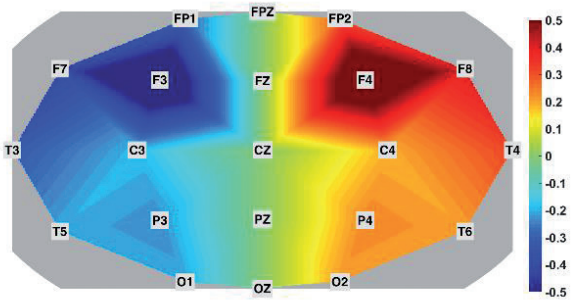

Fig. 3. *An example of an interhemispheric asymmetry map in* **a patient** *with delayed cerebral ischemia. The delta frequency range (2-4 Hz) is considered. The length of the EEG record is 19 hours. The displayed values are the coefficients of* **the first** *component of PCA. The values are indicated by a color scale. Interhemispheric EEG asymmetry in the delta frequency range is observed in IAM. It is generalized over the entire surface of the scalp. Notably, maximal interhemispheric differences are observed in electrodes F3 and F4.*

Note that we observed IAMs similar to Fig. 3 in both patients with delayed cerebral ischemia. At the same time, such IAMs were not observed when delayed ischemia is absent in patients. Below we will demonstrate that the considered patient has other forms of interhemispheric asymmetry corresponding to other components of PCA.

IAMs allow separating and considering one-by-one uncorrelated trends of interhemispheric EEG asymmetry. Next, typical cases of IAMs of the norm (patients not suffering from delayed ischemia) will be considered.

2.3. Examples of normal EEG visualization

Usually, the norm is not characterized by interhemispheric EEG asymmetry. Nevertheless, one can observe various forms of asymmetry in normal IAMs caused by EEG artifacts. **Fig. 4** demonstrates an example of IAM indicating a simple EEG artifact.

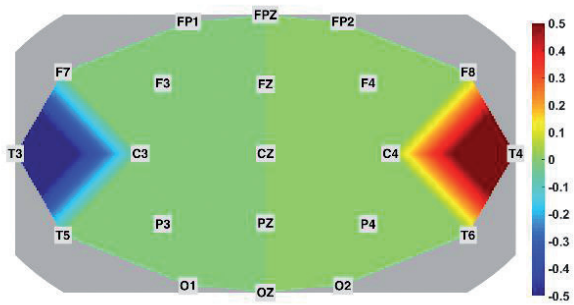

Fig. 4. *An example of an interhemispheric asymmetry map in* **a norm** *(a patient without delayed cerebral ischemia). The delta frequency range (2-4 Hz) is considered. The length of the EEG record is 32 hours. The displayed values are the coefficients of* **the first** *component of PCA. The values are indicated using a color scale. The coefficients of the PCA component under consideration differ from 0 only in electrodes T3 and T4. We can conclude that the observed interhemispheric difference is not generalized and is caused by an EEG* **artifact**.

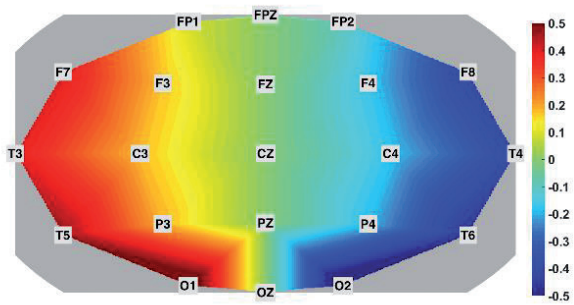

Fig. 5. *An example of an interhemispheric asymmetry map in* **a norm**. *The delta frequency range (2-4 Hz) is considered. The length of the EEG record is 17 hours. The displayed values are the coefficients of* **the first** *component of PCA. The values are indicated using a color scale. Interhemispheric EEG asymmetry in the delta frequency range is generalized over the entire surface of the scalp. Maximal interhemispheric differences are observed in electrodes O1 and O2. This example demonstrates that the presence of generalized interhemispheric asymmetry in itself is not a sign of a disease.*

Electrodes T3 and T4 in IAM are indicated in blue and red respectively. Other IAM electrodes are indicated in green, which corresponds to the coefficient of 0. This means that the observed differences between electrodes T3 and T4 do not correlate with other electrodes. Probably, the observed difference between electrodes is caused by the loss of electrical contact between the T3 electrode and the patient's skin.

Fig. 5 demonstrates a more complex example of a norm IAM. On this IAM, in contrast to the previous example, interhemispheric differences are observed in almost all electrodes located along the edges of the map. Such IAMs display EEG artifacts caused by the penetration of electromyographic signals (EMG) into EEG. The EEG electrodes located along the edges of the IAM are most affected by EMG of the muscles of the neck and face. In the example under consideration, observed EEG artifacts were caused by the patient lying mainly on his left side during the day.

Given examples demonstrate that the presence of amplitude asymmetry in the patient's IAM is not in itself a sign of delayed cerebral ischemia. It is necessary to take into account the form of EEG asymmetry, namely, the relative position and size of the colored area in IAM to diagnose the patient properly. Below, examples of IAMs of patients with delayed cerebral ischemia are given in various frequency ranges.

3. ANALYSIS OF INTERHEMISPHERIC EEG ASYMMETRY IN PATIENTS WITH DELAYED CEREBRAL ISCHEMIA

3.1. Data collection and preprocessing

EEG measurements of patients were carried out in the Department of Neurosurgery of the Sklifosovsky Research Institute for Emergency Medicine using a Mizar-EEG-202 electroencephalograph. Silver Chloride Cup EEG Electrodes were used. The electrodes were installed according to the standard 10-20 system; 21 EEG electrodes were installed. The reference and ground electrodes were placed

along the midline between points Fz and Cz. A high pass filter of 0.5 Hz and a low pass filter of 70 Hz were used. A sampling frequency of 250 Hz was used.

The clinical EEG differs from the laboratory EEG in containing a large number of outliers and significant zero drift. A possible method to improve the quality of EEG signals is the usage of the double banana montage. When using this montage, the computer screen displays the difference in EEG signals measured at nearby electrodes. Double banana montage helps to reduce the zero drift in the EEG signals but the number of outliers in the EEG signals only increases because EEG contains outliers originating from both subtracted EEG channels. In this study, we solve the problem of removing outliers in EEG signals using the X42 statistical method [22] with preliminary trend removal using median filtering. **Fig. 6** demonstrates an example of an EEG signal before zero drift and outliers were removed. **Fig. 7** demonstrates the same signal after removing the outliers.

During the construction of AUC diagrams, the EEG record is divided into segments of 10 minutes. When considering different frequency ranges, the EEG signal is filtered by 8-order Butterworth bandpass filters. The signal is passed through the filter in the forward direction and then in the reverse direction to

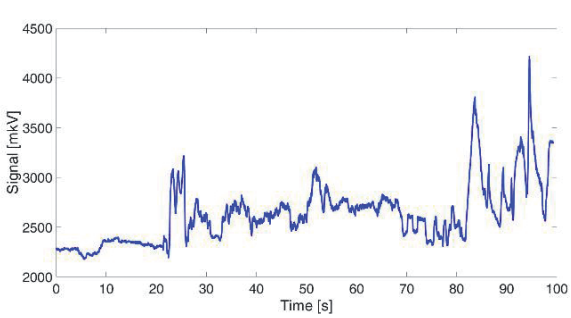

Fig. 6. *An example of a clinical EEG record. The signal contains a significant zero drift which complicates the application of standard outlier removal methods. The abscissa axis is time in seconds. The ordinate axis is the signal in μV.*

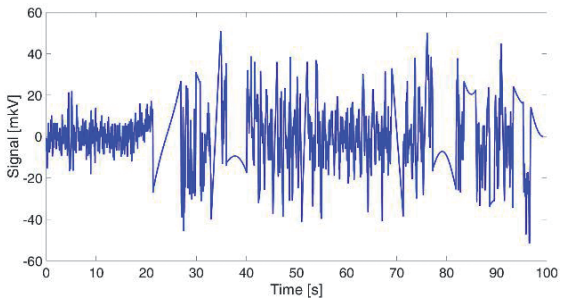

Fig. 7. *An example of a clinical EEG record after the removal of outliers using the X42 statistical method with preliminary removal of zero drift using median filtering. The abscissa axis is time in seconds. The ordinate axis is the signal in μV.*

prevent the phase shift. The instantaneous amplitude of the filtered EEG signal is computed using the Hilbert transform. The square of the instantaneous amplitude of the filtered EEG signal is computed. The average value of the squared instantaneous amplitude is computed. The computed average value is used to compare EEG segments and construct AUC diagrams. When constructing the M matrix, 16 electrodes of 21 were used; thus, 8 pairs of symmetrical EEG electrodes were considered.

3.2. EEG analysis in different frequency ranges

Let us consider examples of IAMs in different frequency ranges. The EEG data in the same patient with delayed cerebral ischemia discussed in Sections 1, 2.1, and 2.2 will be used to construct IAM.

The AUC diagram corresponding to the first component of PCA was considered in Fig. 2. Let us create an AUC diagram corresponding to the second component of PCA (see **Fig. 8**). In the diagram, there is a solid blue area in the delta, theta, alpha, and beta frequency ranges. Note that the abrupt transition from dark blue to dark red in the frequency range above 16 Hz is a computational artifact that does not affect the color of the corresponding IAMs.

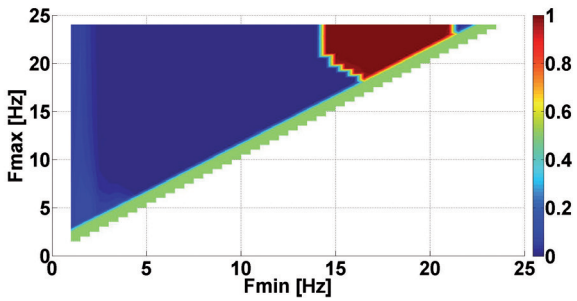

Fig. 8. *An example of an AUC frequency diagram of EEG in* **a patient** *with delayed cerebral ischemia. The displayed value is AUC when comparing the amplitudes of EEG fragments in the left and right hemispheres. The projection of the amplitude values onto* **the second** *principal component is computed. The value is indicated using a color scale. On the AUC diagram, there is a blue area in the delta frequency range of 2-4 Hz.*

The IAM corresponding to the second component of PCA in the delta frequency range (2-4 Hz) is demonstrated in **Fig. 9**. This IAM can be considered as a refinement of IAM corresponding to the first component of PCA demonstrated in Fig. 3. In other words, the relationship between the degrees of interhemispheric asymmetry in different pairs of electrodes is not limited to the correlation

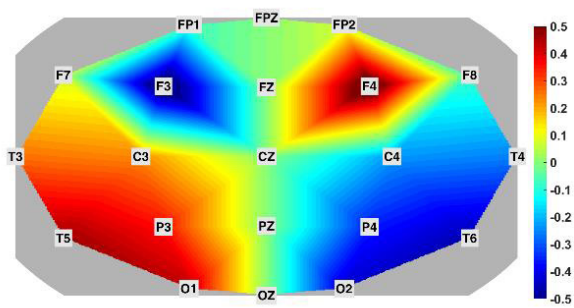

Fig. 9. *An example of an interhemispheric asymmetry map in* **a patient** *with delayed cerebral ischemia. The* **delta** *frequency range (2-4 Hz) is considered. The length of the EEG record is 19 hours. The displayed values are the coefficients of* **the second** *principal component of PCA. The values are indicated using a color scale. Interhemispheric EEG asymmetry in the delta frequency range is generalized over the entire surface of the scalp. There is a correlation between an increase in the EEG amplitude in the affected area (electrode F4) and a decrease in the EEG amplitude in the central and occipital regions of the scalp.*

demonstrated in Fig. 3. There is a weaker trend of the interhemispheric asymmetry demonstrated in Fig. 9 against the background of the trend demonstrated in Fig. 3.

In Fig. 9, there is a correlation between an increase in amplitude in the area of brain damage (electrode F4) and a decrease in amplitude in the central and occipital regions of the scalp. This correlation can be explained by that the increase in the amplitude of the delta rhythm in the F4 electrode is caused by the presence of a breach-rhythm [23] but not only the delayed cerebral ischemia. We observe IAMs, similar to Fig. 9 in both patients with delayed cerebral ischemia. At the same time, such IAM was not observed in patients if the delayed ischemia is absent.

Let us consider frequency ranges. The AUC diagram of the first component of PCA (Fig. 2) demonstrates that the theta neurophysiological range is located on the border between the frequency ranges where different interhemispheric asymmetry is observed. In this situation, we cannot consider the standard theta range (4-8 Hz) as a whole. Below, we consider the upper subrange of 6-8 Hz of the theta range.

The study of IAM in the theta subrange 6-8 Hz demonstrates that IAM in the theta subrange 6-8 Hz is more varied than in the delta range. In particular, we observed a decrease in the theta rhythm on different days in the occipital, central, and frontal parts of the scalp in patients with delayed ischemia in the first component of PCA (see an example in **Fig. 10**).

The high variability of IAM in the theta subrange 6-8 Hz may be caused by that this frequency range is located on the border of the delta and alpha ranges that demonstrate different directions of the change in the EEG amplitude. There is an opinion that the decrease in the alpha and beta rhythms

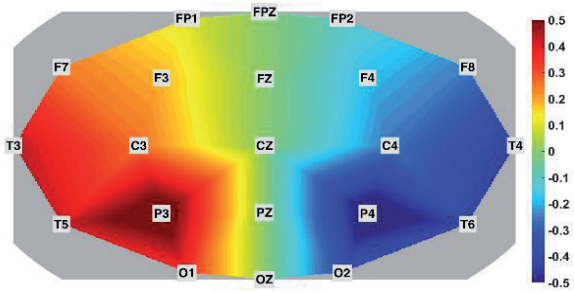

Fig. 10. *An example of an interhemispheric asymmetry map in* **a patient** *with delayed cerebral ischemia. The upper* **theta** *subrange 6-8 Hz is considered. The length of the EEG record is 19 hours. The displayed values are the coefficients of* **the first** *component of PCA. The values are indicated using a color scale. We observe an interhemispheric EEG asymmetry in IAM generalized over the entire surface of the scalp. Notably, maximal interhemispheric differences are observed in the posterior region of the scalp in the electrodes P3 and P4.*

may occur later than the increase in the delta rhythm in patients with delayed ischemia [12, 24]. This issue may also be a reason for the variability of IAM in the theta subrange. Thus, IAM in the theta range may contain important information about the clinical course but this issue requires more detailed study.

In IAM of the first PCA component in the alpha frequency range (8-12 Hz), we observed a decrease in the EEG amplitude in the central and posterior areas of the scalp on the affected hemisphere in one patient with delayed cerebral ischemia (see example in **Fig. 11**). This localization of the interhemispheric asymmetry may relate to the fact that the sources of the alpha rhythm are located in the occipital region of the cortex and the sources of the mu rhythm (at the same frequencies) are located in the central region of the cortex. In the second patient with delayed ischemia, a similar pattern of changes in the alpha rhythm was also observed; however, the corresponding IAM was practically the same as the IAM of the normal alpha rhythm. Thus, alpha IAMs also provide useful diagnostic information but their applicability may be more limited than delta IAMs.

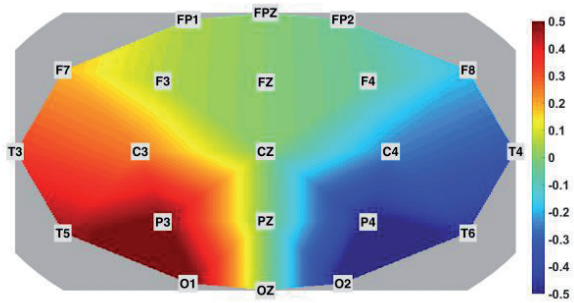

Fig. 11. *An example of an interhemispheric asymmetry map in* **a patient** *with delayed cerebral ischemia. The* **alpha** *frequency range (8-12 Hz) is considered. The length of the EEG record is 19 hours. The displayed values are the coefficients of* **the first** *component of PCA. The values are indicated using a color scale. We observe an interhemispheric asymmetry of EEG in the alpha frequency region generalized in the central and posterior regions of the scalp.*

IAMs of the first component of PCA in the beta-I frequency range (13-15 Hz) in both patients with delayed cerebral ischemia were similar to IAM in the alpha frequency range. Thus, examples of IAMs in the beta-I frequency range are not given for brevity.

Fig. 12 demonstrates an example of IAM of the first component of PCA in the beta-II frequency range (17-24 Hz). Notably, IAM in the beta-II range differs from IAM in the alpha range. This difference can be explained by that the sources of the beta

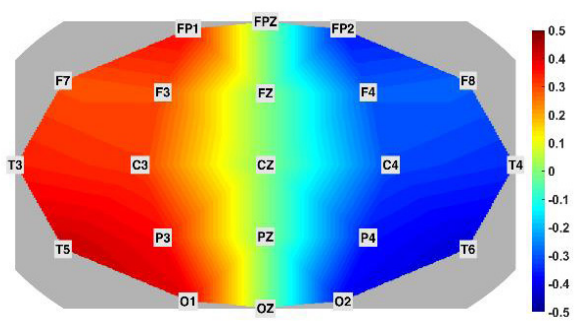

Fig. 12. *An example of an interhemispheric asymmetry map in* **a patient** *with delayed cerebral ischemia. The* **beta-II** *frequency range (17-24 Hz) is considered. The length of the EEG record is 19 hours. The displayed values are the coefficients of* **the first** *component of PCA. The values are indicated using a color scale. We observe the interhemispheric EEG asymmetry in the beta-II frequency range generalized over the entire surface of the scalp.*

rhythm in the cerebral cortex do not have a definite localization. We observe IAMs similar to Fig. 12 in both patients with delayed cerebral ischemia. At the same time, such IAMs were not observed in patients when delayed cerebral ischemia is absent.

Thus, all considered neurophysiological frequency ranges delta, theta, alpha, and beta contain useful information about the clinical course of the disease; however, the diagnostic value of the frequency ranges is different. Let us compare the results of the interhemispheric EEG asymmetry analysis with the data described in the literature.

3.3. Comparison of EEG analysis results in frequency ranges

Research papers studying EEG in patients with delayed cerebral ischemia describe mainly changes in EEG in different frequency ranges over time. In other words, EEG is compared before and after the onset of delayed ischemia [4-6]. In contrast to these studies, we compare EEG in the cerebral hemispheres directly during delayed ischemia. Nevertheless, the results of studies can be compared because EEG changes over time are different in the affected and contralateral hemispheres [3,25-28].

Research papers express different opinions about the diagnostic value of different EEG ranges. For example, [29] demonstrated that the theta and alpha ranges have the highest diagnostic value for the early diagnosis of delayed cerebral ischemia (2-3 days in advance); a 40% decrease within 5-6 hours in focal EEG amplitude was considered as a sign of this complication. The paper [29] notes the importance of removing EEG artifacts and the separation of focal EEG changes and regional EEG changes caused by the status of patients and drug-induced action. In the framework of our method, we use IAMs to detect interhemispheric asymmetry caused by focal EEG changes and PCA to separate uncorrelated focal and regional EEG changes. In addition, we use AUC diagrams to refine the boundaries of the EEG frequency ranges. In most studies, including [29], this check is not implemented; thus, the diagnosis is carried out using incorrect boundaries of the theta range, which simultaneously falls into the regions of an increase and a decrease in the EEG amplitude. This issue allows us to explain the contradictory data on the theta range EEG amplitude changes reported in the literature [4,5].

[30] reports that delta range EEG interhemispheric asymmetry depends on the degree of damage in the cortex and subcortical structures of the brain. Thus, EEG in the delta range may contain additional information useful for diagnosing the patient. We used IAM for analyzing delta range EEG to separate the sign of delayed cerebral ischemia and delta waves caused by sleep. IAMs allow one to abstract from EEG changes caused by sleep because they appear mainly simultaneously on both hemispheres of the brain.

A study of shorter time intervals (about 1 hour) demonstrated that IAMs of patients with delayed cerebral ischemia in some intervals were similar to IAMs of the daily records considered above. However, the estimation of minimal time intervals sufficient for an accurate diagnosis of delayed ischemia is a topic for additional research. The examples of patients with delayed cerebral ischemia considered in this paper are not sufficient to make conclusions about the sensitivity and specificity of the observed interhemispheric asymmetry maps. We can only conclude that the developed visualization tool helps to identify EEG asymmetry patterns that are expected from a neurophysiological point of view.

4. CONCLUSION

A new type of EEG head map named the interhemispheric EEG asymmetry map was developed. The purpose of these maps is to identify signs of delayed cerebral ischemia after subarachnoid hemorrhage. A new type of AUC diagram was developed to check the boundaries of the EEG frequency ranges in which the analysis is carried out. Using AUC diagrams, we have demonstrated that the standard neurophysiological theta range is located on the border between the frequency ranges where the EEG amplitude changes in different directions. This fact allows us to explain contradictory data reported in the literature. IAMs allow us to detect interhemispheric asymmetry caused by focal EEG changes, while PCA is used to separate uncorrelated focal and regional EEG changes. The principles of construction and reading of IAMs and AUC diagrams are demonstrated by the example of analyzing data in two patients with clinically confirmed delayed cerebral ischemia after subarachnoid hemorrhage. EEG changes were demonstrated in the delta, theta, alpha, and beta ranges.

REFERENCES

1. Roy CS, Sherrington CS. On the regulation of the blood-supply of the brain. *The Journal of physiology,* 1890, 11(1-2):85.
2. Berger H. Über das Elektrenkephalogramm des Menschen. XIV [The electroencephalogram of man. XIV]. *Archiv für Psychiatrie und Nervenkrankheiten,* 1938, 108:407-431.
3. Nagata K, Mizukami M, Araki G, Kawase T, Hirano M. Topographic electroencephalographic study of cerebral infarction using computed mapping of the EEG. *Journal of Cerebral Blood Flow & Metabolism,* 1982, 2(1):79-88.
4. Nagata K, Tagawa K, Hiroi S, Shishido F, Uemura K. Electroencephalographic correlates of blood flow and oxygen metabolism provided by positron emission tomography in patients with cerebral infarction. *Electroencephalography and clinical neurophysiology,* 1989, 72(1):16-30.
5. Vespa PM, Nuwer MR, Juhász C, Alexander M, Nenov V, Martin N, Becker DP. Early detection of vasospasm after acute subarachnoid hemorrhage using continuous EEG ICU monitoring. *Electroencephalography and clinical neurophysiology*, 1997, 103(6):607-615.
6. Claassen J, Hirsch LJ, Kreiter KT, Du EY, Connolly ES, Emerson RG, Mayer SA. Quantitative continuous EEG for detecting delayed cerebral ischemia in patients with poor-grade subarachnoid hemorrhage. *Clinical neurophysiology*, 2004, 115(12):2699-2710.
7. Finnigan SP, Rose SE, Walsh M, Griffin M, Janke AL, McMahon KL, Gillies R, Strudwick MW, Pettigrew CM, Semple J, Brown J. Correlation of quantitative EEG in acute ischemic stroke with 30-day NIHSS score: comparison with diffusion and perfusion MRI. *Stroke*, 2004, 35(4):899-903.
8. Tabaeizadeh M, Aboul Nour H, Shoukat M, Sun H, Jin J, Javed F, Kassa S, Edhi M, Bordbar E, Gallagher J, Moura VJ. Burden of epileptiform activity predicts discharge neurologic outcomes in severe acute ischemic stroke. *Neurocritical care*, 2020, 32:697-706.
9. Baang HY, Chen HY, Herman AL, Gilmore EJ, Hirsch LJ, Sheth KN, Petersen NH, Zafar SF, Rosenthal ES, Westover MB, Kim JA. The utility of quantitative EEG in detecting delayed cerebral ischemia after aneurysmal subarachnoid hemorrhage. *Journal of Clinical Neurophysiology,* 2022, 39(3):207-215.
10. van Putten MJ, Hofmeijer J. EEG monitoring in cerebral ischemia: basic concepts and clinical applications. *Journal of clinical neurophysiology,* 2016, 33(3):203-210.
11. van Putten MJ, Tavy DLJ. Continuous quantitative EEG monitoring in hemispheric stroke patients using the brain symmetry index. *Stroke*, 2004, 35(11):2489-2492.

12. Gavaret M, Marchi A, Lefaucheur JP. Clinical neurophysiology of stroke. *Handbook of Clinical Neurology,* 2019, 161:109-119.
13. Ajčević M, Furlanis G, Miladinović A, Buoite Stella A, Caruso P, Ukmar M, Cova MA, Naccarato M, Accardo A, Manganotti P. Early EEG alterations correlate with CTP hypoperfused volumes and neurological deficit: a wireless EEG study in hyper-acute ischemic stroke. *Annals of Biomedical Engineering*, 2021, 49(9):2150-2158; doi: 10.1007/s10439-021-02735-w.
14. Scherschinski L, Catapano JS, Karahalios K, Koester SW, Benner D, Winkler EA, Graffeo CS, Srinivasan VM, Jha RM, Jadhav AP, Ducruet AF. Electroencephalography for detection of vasospasm and delayed cerebral ischemia in aneurysmal subarachnoid hemorrhage: a retrospective analysis and systematic review. *Neurosurgical focus*, 2022, 52(3):E3.
15. Zheng WL, Kim JA, Elmer J, Zafar SF, Ghanta M, Junior VM, Patel A, Rosenthal E, Westover MB. Automated EEG-based prediction of delayed cerebral ischemia after subarachnoid hemorrhage. *Clinical Neurophysiology*, 2022, 143:97-106.
16. Yu Z, Wen D, Zheng J, Guo R, Li H, You C, Ma L. Predictive accuracy of alpha-delta ratio on quantitative electroencephalography for delayed cerebral ischemia in patients with aneurysmal subarachnoid hemorrhage: meta-analysis. *World neurosurgery,* 2019, 126:e510-e516.
17. Sushkova OS, Morozov AA, Gabova AV. Data mining in EEG wave trains in early stages of Parkinson's disease. *Advances in Soft Computing: 15th Mexican International Conference on Artificial Intelligence,* MICAI 2016, Cancún, Mexico, October 23-28, 2016, *Proceedings, Part II 15,* Springer International Publishing, 2017:403-412.
18. Sushkova OS, Morozov AA, Gabova AV, Karabanov AV. Application of brain electrical activity burst analysis method for detection of EEG characteristics in the early stage of Parkinson's disease. *Zhurnal Nevrologii i Psikhiatrii imeni S.S. Korsakova*, 2018, 118(7):45-48.
19. Sushkova OS, Morozov AA, Gabova AV, Karabanov AV. Investigation of surface EMG and acceleration signals of limbs' tremor in Parkinson's disease patients using the method of electrical activity analysis based on wave trains. *Advances in Artificial Intelligence – IBERAMIA* 2018: *16th Ibero-American Conference on AI,* Trujillo, Peru, November 13-16, 2018, *Proceedings 16*, Springer International Publishing, 2018: 253-264.
20. Sushkova OS, Morozov AA, Gabova AV, Karabanov AV, Illarioshkin SN. A Statistical Method for Exploratory Data Analysis Based on 2D and 3D Area under Curve Diagrams: Parkinson's Disease Investigation. *Sensors*, 2021, 21(14):4700.
21. Sushkova OS, Morozov AA, Kershner IA, Khokhlova MN, Gabova AV, Karabanov AV, Chigaleichick LA, Illarioshkin SN. Investigation of Phase Shifts Using AUC Diagrams: Application to Differential Diagnosis of Parkinson's Disease and Essential Tremor. *Sensors,* 2023, 23(3):1531.
22. Hampel FR, Ronchetti EM, Rousseeuw P, Stahel WA. *Robust statistics: the approach based on influence functions*. New York, Wiley-Interscience, 1986.
23. Mironov MB, Burd SG, Kukina NV, Rubleva YuV, Kordonskaya GG, Senko IV, Yurchenko AV, Bogomazova MA, Tairova RT, Dzhabrailova KhA. Breach-rhythm. *Epilepsy and paroxysmal conditions,* 2021, 13(2):140-146.
24. Hahn CD, Wusthoff CJ (eds.). *Neuromonitoring in Neonatal and Pediatric Critical Care*, Cambridge University Press, 2022.
25. Green RL, Wilson WP. Asymmetries of beta activity in epilepsy, brain tumor, and cerebrovascular disease. *Electroencephalography and Clinical Neurophysiology*, 1961, 13(1):75-78.

26. LaRoche SM, Haider HA (eds.). *Handbook of ICU EEG monitoring,* Springer Publishing Company, 2018.
27. Nurfirdausi AF, Apsari RA, Wijaya SK, Prajitno P, Ibrahim N. Wavelet Decomposition and Feedforward Neural Network for Classification of Acute Ischemic Stroke based on Electroencephalography. *International Journal of Technology,* 2022, 13(8):1745-1754.
28. Koziolkin OA, Kuznietsov AA. Electroencephalographic criteria of the functional outcome prognosis in the acute period of spontaneous supratentorial intracerebral hemorrhage. *Zaporozhye Medical Journal*, 2020, 22(5):604-610. DOI: 10.14739/2310-1210.2020.5.214759.
29. Gollwitzer S, Groemer T, Rampp S, Hagge M, Olmes D, Huttner HB, Schwab S, Madžar D, Hopfengaertner R, Hamer HM. Early prediction of delayed cerebral ischemia in subarachnoid hemorrhage based on quantitative EEG: a prospective study in adults. *Clinical Neurophysiology*, 2015, 126(8):1514-1523.
30. Fanciullacci C, Bertolucci F, Lamola G, Panarese A, Artoni F, Micera S, Rossi B, Chisari C. Delta power is higher and more symmetrical in ischemic stroke patients with cortical involvement. *Frontiers in human neuroscience*, 2017, 11:385.

DOI: 10.17725/rensit.2023.15.153

Obtaining of titanium dioxide (rutile) particles on the surface of reduced graphene oxide in supercritical isopropanol

Yulia A. Groshkova
Scientific and Production Association "GRAFENIKA", http://www. akkolab.ru/
Moscow 107143, Russian Federation
E-mail: JuliaGroshkova@yandex.ru

Sergey V. Kraevskii
Lopukhin Federal Research and Clinical Center of Physical-Chemical Medicine of Federal Medical-Biological Agency of Russia, http://rcpcm.org/
Moscow 119435, Russian Federation
E-mail: kraevskii@mail.ru

Elena Yu. Buslaeva
Kurnakov Institute of General and Inorganic Chemistry of RAS, http://www.igic.ras.ru/
Moscow 119090, Russian Federation
E-mail: buslaeva@igic.ras.ru

Received June 20, 2023, peer-reviewed June 23, 2023, accepted June 25, 2023

Abstract: **Sequential synthesis of rutile modification titanium dioxide particles on reduced graphene oxide in supercritical isopropanol is described. In this case, only graphene oxide was reduced to reduced graphene oxide. A one-stage method (one-pot) was also developed for the preparation of rutile particles on reduced graphene oxide, where supercritical isopropanol was the graphene oxide reducing agent and the reaction medium. The resulting composites were studied using X-ray phase analysis, transmission electron microscopy, and atomic force spectroscopy methods.**

Keywords: **titanium oxides, rutile, graphene oxide, reduced graphene oxide**

UDC 546.2+546.7+546.05

Acknowledgements: The work was carried out within the framework of the state task of Kurnakov Institute of General and Inorganic Chemistry of RAS.

For citation: Yulia A. Groshkova, Sergey V. Kraevskii, Elena Yu. Buslaeva. Obtaining of titanium dioxide (rutile) particles on the surface of reduced graphene oxide in supercritical isopropanol. *RENSIT: Radioelectronics. Nanosystems. Information Technology,* 2023, 15(2):153-160e. DOI: 10.17725/rensit.2023.15.153.

Contents

1. INTRODUCTION

Works on the graphene compounds synthesis and the study of its unique physical properties in the world form one of the most promising areas in the chemistry and physics of new inorganic functional materials [1–3]. One of the important consequences of the graphene discovery is the interest in obtaining composites of metal and metal oxides on the graphene surface [4,5].

Particularly attractive for use were composites based on RGO and titanium oxides. And a number of these composites are already being successfully used [6-8]. The works are aimed at obtaining a practical result as soon as possible. However, the choice of methods for the synthesis of both titanium dioxide nanoparticles and RGO is quite random. Often used for the synthesis of titanium oxide, as well as for the production of RGO, multistage methods, toxic substances [9]. However, there are practically no works on the synthesis of rutile composites on RGO. In our work, we have developed 2 universal, easy methods for the synthesis of TiO_2 (rutile) particles on RGO using a non-toxic reagent – supercritical isopropanol.

2. EXPERIMENTAL PART

As initial reagents we used: natural graphite (99.9% purity, China), titanium isopropoxide $Ti(OCH(CH_3)_2)_4$ (Titan(IV)-isopropylat, 98%, CAS: 546-68-9), isopropanol C_3H_7OH puriss. spec. TC 2632-011-29483781-09, hexane, analytical grade.

2.1. Production of TiO_2 particles (rutil)

Rutile particles were obtained by hydrolysis of titanium isopropoxide [10]. A solution was prepared from 5 ml of titanium isopropoxide and 15 ml of isopropanol. Distilled water (250 ml) was added to this solution. The solution was stirred at room temperature for 30 minutes. Then the resulting solution was poured into Petri dishes and placed in an oven at 95°C for 19 hours.

The volume of the solution was reduced by half and the resulting solution was dispersed using powerful ultrasound (parameters: frequency – 20.4 kHz, specific power – 0.1-1 W/cm^3) for 25 min. After cooling, they were centrifuged with hexane at 8000 rpm for 25 min. It was dried for several hours at 80°C, and then the resulting powder was washed with ethanol (3 times). The powder was calcined at 800°C for 2 h to get rutile.

2.2. Preparation of graphene oxide and reduced graphene oxide

Graphene oxide (GO) was obtained by the modified Hummers method [11], by sequentially oxidizing natural graphite acids with acids, followed by washing to neutral pH and ultrasonic treatment (parameters: frequency – 20.4 kHz, specific power – 0.1-1 W/cm^3), for 30 minutes until stable dark brown dispersion with c = 1 mg/ml. Part of the GO dispersion was dried to a constant weight, and the resulting dark gray powder was reduced in supercritical isopropyl alcohol using a small-volume autoclave made of EP-943 nickel alloys [12].

2.3. Deposition of rutile particles on the surface of graphene oxide (I metod)

0.1 g of GO and 5.8 ml of C_3H_7OH were added to 0.01 g of TiO_2-rutile, and the mixture was sonicated for 20 min. The solution was poured into a quartz container and placed in an autoclave, which was in an air thermostat at 285°C for 24 hours to restore in supercritical isopropanol. The resulting black precipitate was washed with C_3H_7OH and C_3H_6O in a ratio of 1:1 several times with a centrifuge at 6000 rpm for 10 min, after which the material

was dried at room temperature to constant weight. The composition and structure of rutile composites on the surface of RGO flakes were studied by a complex of physicochemical methods of analysis - X-ray phase analysis, atomic force spectroscopy and transmission electron microscopy

2.4. Obtaining of rutile particles on the surface of reduced graphene oxide (method II or one-pot method)

To 5 ml of $Ti(OCH(CH_3)_2)_4$ (in 15 ml of C_3H_7OH) was added in portions the earlier prepared dispersion of graphene oxide, sonicated for 20 min, with vigorous stirring on a magnetic stirrer. After that, 250 ml of deionized water was added, stirring for 30 minutes and dried at 65°C for 19 hours. The resulting powder was placed in a vacuum furnace at 100°C for 3 hours, followed by annealing at 800°C to obtain rutile on the RGO surface for 4 hours. The resulting powder was washed with C_3H_7OH and C_3H_6O in a ratio of 1:1 using a centrifuge at 6000 rpm for 10 min, after which the material was dried at room temperature to constant weight. Further, the obtained samples were investigated by physico-chemical methods of analysis.

3. RESULTS AND DISCUSSION

3.1. Research methods

To characterize rutile particles as well as composites of GO-rutile particles and RGO-rutile particles, a set of methods was used: *X*-ray phase analysis (XPA), transmission electron microscopy (TEM), atomic force microscopy (AFM).

The sizes and shapes of nanoparticles in a dispersion in an organic solvent and in nanocomposites were determined by analytical processing of TEM images obtained by TEM on a JEOL JEM-2100 setup at an accelerating voltage of 100 kV and 150 kV, respectively.

Before recording, the samples were placed on copper grids 3.05 mm in diameter covered with a polymer film. Transmission images were taken at magnifications up to 500,000 x, and a 0.4 μm diameter limiting diagram was used for electron diffraction imaging.

The ratio $\lambda L = Rd$ was used to determine the interplanar spacing using the reflections of the diffraction pattern in an electron microscope. The length of the chamber in an electron microscope was determined by passing electrons through all lenses.

AFM measurements were made in air using a Nanoscope III microscope (Digital Instruments) equipped with a 150 μm scanner in tapping and contact modes. We used commercial non-contact silicon cantilevers with a hardness of 11.5 N/m and a resonant frequency in the range of 193-325 kHz. The stiffness of the used contact cantilevers was 0.01 or 0.3 N/m. The scanning frequency is about 2 Hz. All AFM images were recorded simultaneously in two channels: height and deviation (for the contact mode) or height and amplitude (for the tapping mode). Image processing was performed using the FemtoScan program (Filonov AS et al., 2001).

Powder particles prepared at IGIC were diluted with distilled water. The resulting suspension was shaken, and 20 μl was taken from it to be applied to a fresh chip of mica, which was used as a substrate. The obtained samples were dried in a stream of nitrogen.

3.1.2. Study of the obtained GO and RGO

Fig. 1 shows the radiograph of the GO. The results of X-ray phase analysis showed the presence of one phase of GO, which is characterized by the presence of two peaks: the peak at 130 has a high intensity, and the peak at 430 is much less pronounced. The peak at 280 corresponds to the graphite peak.

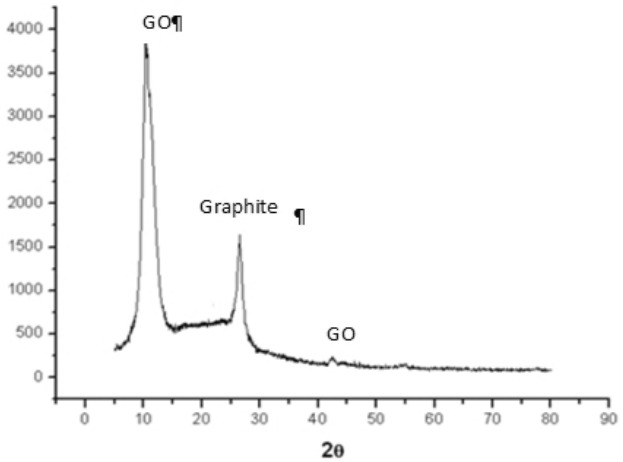

Fig. 1. *X-ray diffraction pattern of GO oxide.*

The presented TEM micrograph (**Fig. 2**) refers to GO.

Fig. 3 shows the result of X-ray phase analysis of the RGO. It is known that the RGO peak is similar to the graphite peak, but is shifted by 20, i.e. the peak related to RGO is 260, as shown in the image.

First, graphene oxide was obtained, after placing GO in the SCI, successful reduction occurred, and fully reduced graphene (RGO) was obtained with one peak at 260. This can be seen in the X-ray pattern (Fig. 3).

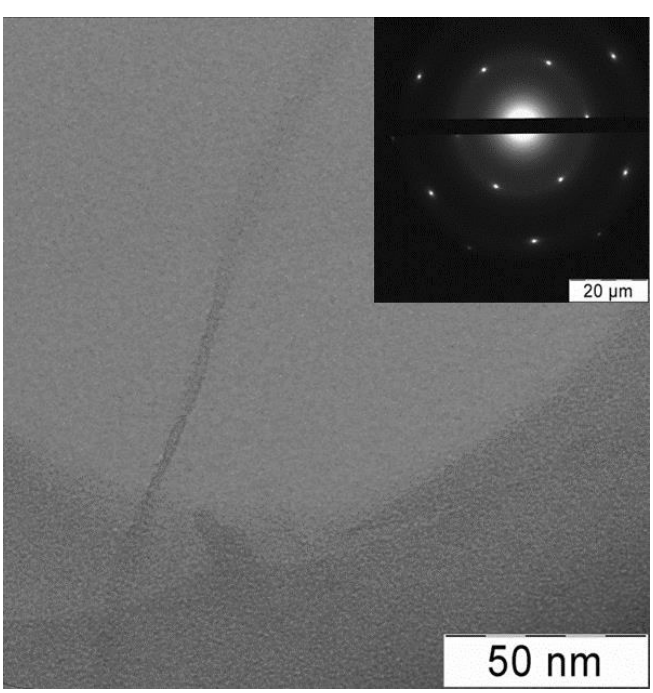

Fig. 2. *Micrograph of GO oxide.*

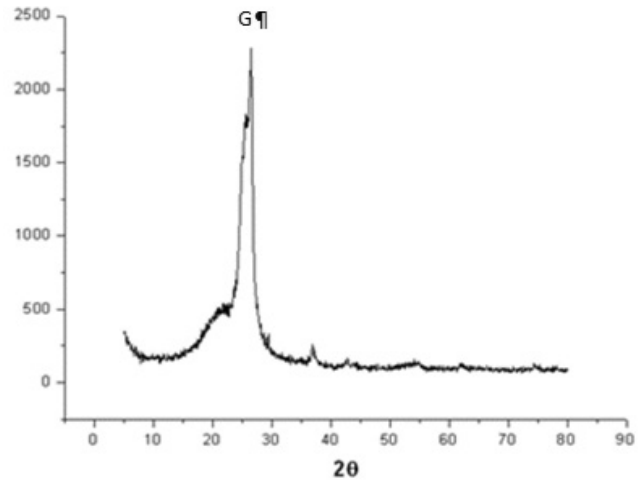

Fig. 3. *X-ray of the RGO.*

Fig. 4 shows a TEM micrograph of the RGO after SCI.

3.2. Deposition of rutile particles on the surface of graphene oxide

GO (0.1 g) and isopropanol C_3H_7OH (5.8 ml) were added to 0.01 g of titanium oxide (rutile), the mixture was treated with ultrasound (frequency – 20.4 kHz, specific power – 0.1-1 W/cm^3) within 20 min. The resulting crystalline rutile (0.069 g) was mixed with graphene oxide (0.135 g) and isopropanol (5.8 ml). The resulting solution was poured into a quartz container and placed in a small-volume autoclave for recovery in the SCI.

Small-volume autoclaves made of EP-

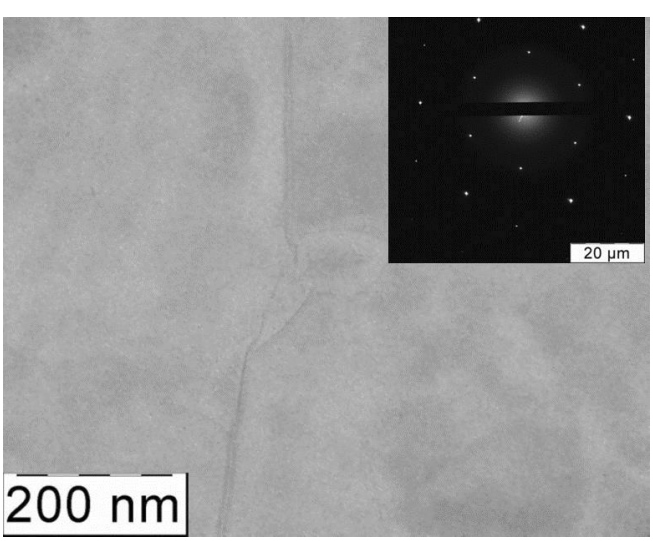

Fig. 4. *Micrograph of RGO.*

943 nickel alloys [13] were used for the experiment. A quartz container containing a dispersion of titanium dioxide, GO, and isopropanol was placed in the autoclave. The autoclave, in turn, is placed in an air thermostat, and kept at a given temperature for the required time (time in supercritical 18 hours, temperatures 280-285°C).The resulting black precipitates were redispersed in isopropanol using a centrifuge at 6000 rpm 3 times. After that, the powders were dried at room temperature to constant weight. Further, the resulting black precipitates were washed with isopropanol and acetone in a ratio of 1:1 several times, centrifuged at 6000 rpm for 10 minutes, after which the material was dried at room temperature to constant weight. The composition and structure of rutile composites on the surface of RGO flakes were studied using a complex of XRD, AFM, and TEM methods.

Rutile particles on the GO surface were obtained using isoropanol as a medium. The choice of isopropanol as a solvent was due to the fact that the synthesis of nanoparticles in it is relatively easy to control, reproducible and allows obtaining particles of a certain size. In addition, this solvent prevents particle agglomeration due to the interaction of functional –OH – groups with the particle surface.TiO_2.

3.3. Methods for the obtained samples studying

To characterize particles of titanium oxides, as well as composites of GO-rutile and RGO-rutile particles, a set of methods was used: X-ray phase analysis (XPA), transmission electron microscopy (TEM), and atomic force microscopy (AFM).

The analysis of the X-ray diffraction pattern of rutile presented in **Fig. 5** showed the presence of one TiO_2 phase (JCPDS # 86-0147, tetragonal, primitive space group $P4_2/$

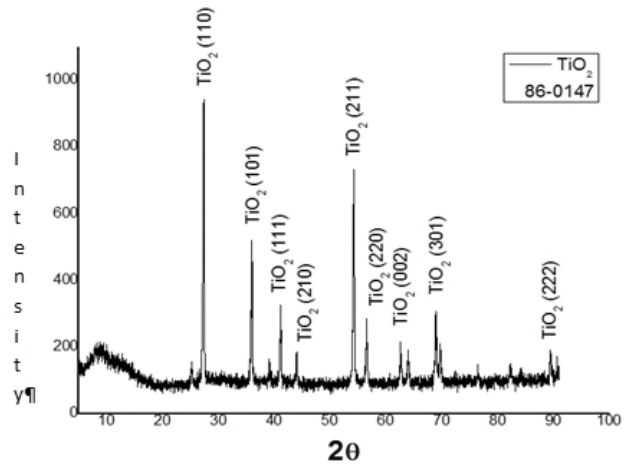

Fig. 5. *X-ray diffraction pattern of TiO2 particles (rutile).*

mmm, $a = 4.594$ Å, $c = 2.958$ Å). The reflections in the diffraction pattern are narrowed, which indicates the large sizes of the studied particles. The calculation using the Debye-Scherer formula showed that the average particle size of rutile is about 170-180 nm.

Fig. 6 shows an electron microscopic image of TiO_2 (rutile) particles, from which it can be seen that the studied sample has a shape close to spherical, and also has a narrow size distribution for an aggregate of more than 100 particles. The size distribution histogram showed that the average NP size is 180 nm.

The results of the study of the rutile/RGO X-ray pattern (**Fig. 7**) showed the presence of two phases: TiO_2 (JCPDS # 86-0147, tetragonal, space group $P4_2/mmm$, $a = 4.594$ Å, $c = 2.958$ Å) and graphene. The reflections of titanium oxide (rutile) on the diffraction pattern are narrowed, which indicates a significant size of the particles under study.

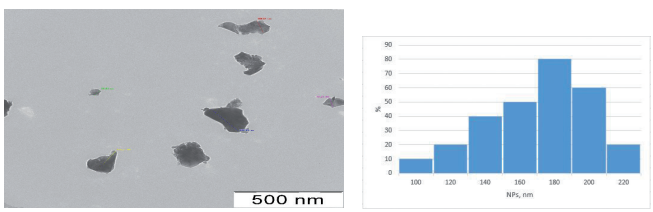

a *b*

Fig. 6. *a) micrograph of rutile particles, b) size distribution histogram.*

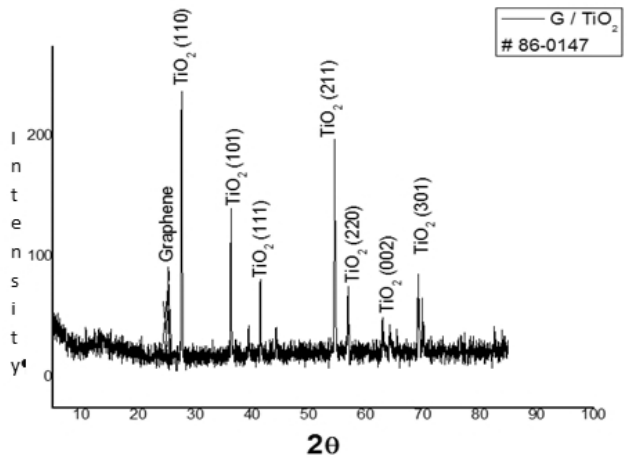

Fig. 7. *Rutile/RGO radiograph.*

According to the Debye-Scherer formula, it was calculated that the average particle size of TiO_2 (rutile) is about 170-180 nm.

According to the AFM images (**Fig. 8**) of rutile/RGO particles, it can be said that rutile

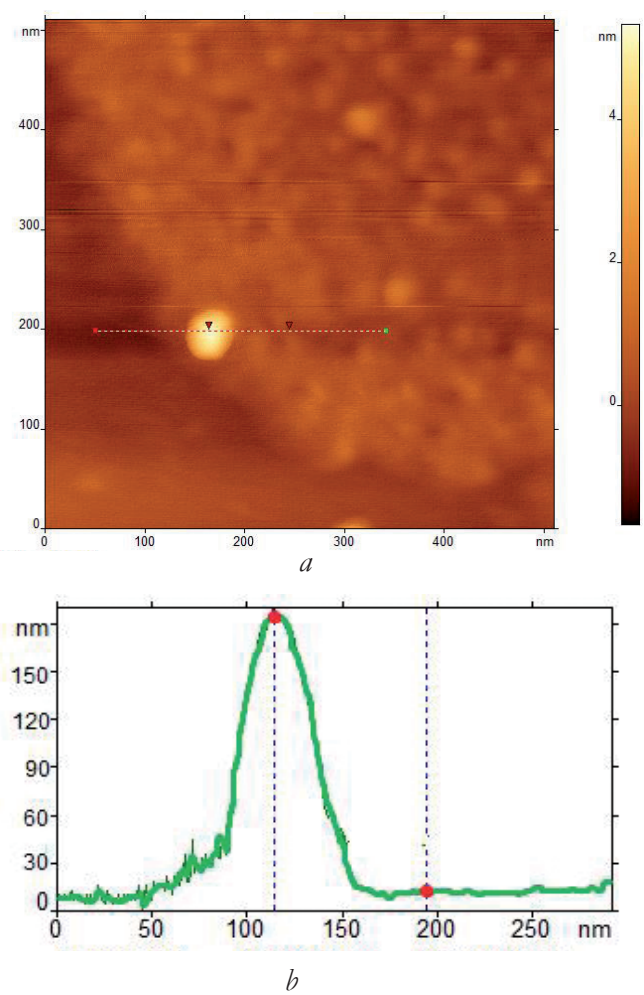

Fig. 8. *a) AFM/RGO image), b) longitudinal section along the cut line.*

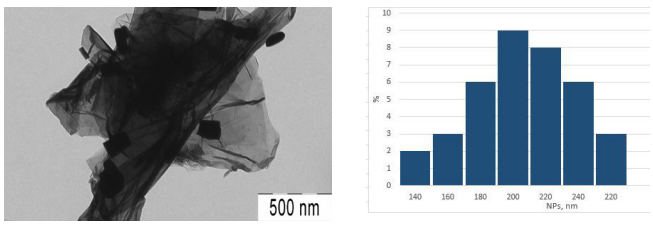

Fig. 9. *a) micrograph of rutile/RGO), b) size distribution histogram.*

particles are located only on the surface of graphene flakes, their average height is 180 nm. The thickness of graphene flakes is 5 nm, and the lateral size of graphene flakes is 1 μm.

The micrograph of the rutile/RGO sample (**Fig. 9**) under study clearly shows that the particles are immobilized on the graphene surface. Also, according to the size distribution histogram, the average size of TiO_2 nanoparticles was 200 nm

The XRF analysis is shown in **Fig. 10**. The image shows the presence of two phases: TiO_2 (# 78-1510, tetragonal, space group $P4_2/mmm$) and graphene. The reflections of the studied titanium oxide sample on the X-ray diffraction pattern are expanded, which indicates the large size of the nanoparticles. The peak at 260 corresponds to the graphene peak. The average size was calculated using

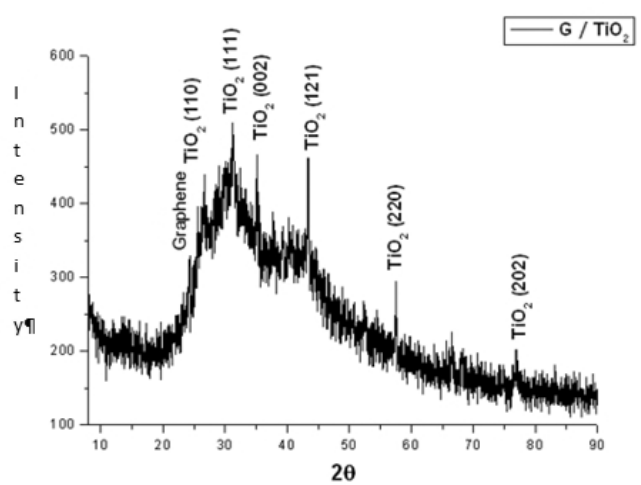

Fig. 10. *X-ray diffraction pattern of rutile/RGO composite.*

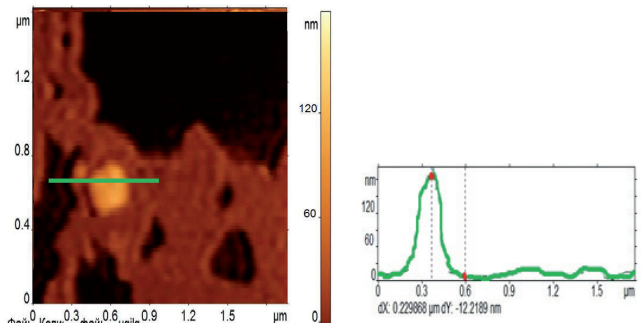

a *b*

Fig. 11. *a) AFM image of RGO rutile particles, b) longitudinal section along the cut line.*

the Debye-Scherer formula, which was 180 nm. According to the data obtained, it can be seen that, after reduction in supercritical isopropanol, titanium oxide nanoparticles were not reduced to Ti, which is typical for anatase powders, as was shown earlier [13].

The AFM micrograph (**Fig. 11**) shows that rutile particles are on the surface of graphene flakes. The particle size of rutile is 180 nm, which corresponds to the XRF data. Also, according to the longitudinal section along the cut line, it can be said that the thickness of the graphene flakes is 3 nm, and the lateral size of the graphene flakes is 1.5 μm.

According to the results of transmission electron microscopy in **Fig. 12**, it can be seen that the resulting rutile particles have a shape close to spherical, and they are also immobilized on the surface of graphene flakes. A histogram of the size distribution was plotted and the average particle size of rutile was shown to be 180 nm.

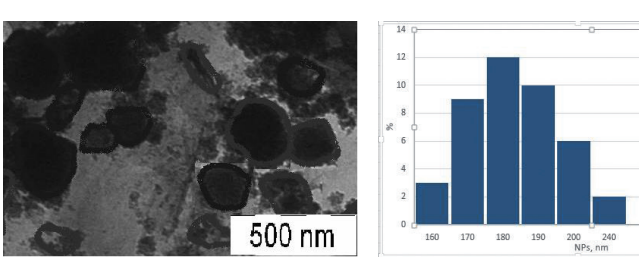

a *b*

Fig. 12. *a) micrograph of rutile/RGO, b) size distribution histogram.*

The resulting rutile particles on RGO were characterized by physico-chemical methods and their size was determined, which was 180 nm. When particles were fixed on the surface of graphene flakes, the particle size increased to 200 nm. Rutiles were also obtained on the RGO surface by the one-pot method, the size of which was also 180 nm. If we compare the thickness of graphene flakes in both cases, then in the one-stage method it was 3 nm (up to 8 layers), which is less than in the two-stage method.

Comparing the two-stage method and the one-pot method, we can say that in the case of the one-stage method, the particle size turned out to be somewhat smaller, and the thickness of the graphene flakes was less, it was 5 layers. In addition, the one-stage synthesis method takes 2 times less time compared to the two-stage one. However, the preparation of rutile nanoparticles (with a rutile particle size of less than 100 nm) on RGO requires further experiments.

4. CONCLUSION

1. As a result of the work done, graphene-TiO_2 (rutile) composites were obtained and characterized by two methods. The methods used are based on the reduction of SCI graphene oxide.

2. It has been shown that when using a dispersion of pre-prepared nanoparticles of metal oxides and graphene oxide, composites are formed containing rutile microparticles on the surface of graphene flakes.

Rutile microparticles are 180 nm in size, graphene flakes are 3-5 layers thick with a lateral size of up to 500 nm.

3. It is shown that it is possible to obtain the same composites in one stage (one pot method) by introducing a metal salt and graphene oxide into the reaction mixture, followed by SCI reduction.

4. SCI is used in all processes as a reaction medium and as a reducing agent for graphene oxide.

5. The obtained composites were characterized by the following methods: X-ray phase analysis, atomic force microscopy, transmission electron microscopy.

DOI: 10.17725/rensit.2023.15.161

Synthesis of polymer composite materials based on zinc oxide nanoparticles synthesized in a plasma discharge under the ultrasonic action

Nikolay A. Bulychev
Moscow Aviation Institute, http://www.mai.ru/
Moscow 125993, Russian Federation
E-mail: nbulychev@mail.ru
Yuri G. Mikhaylov
National Research University of Electronic Technology, http://www.miet.ru/
Zelenograd 124498, Moscow, Russian Federation
E-mail: icc.miet@mail.ru

Received May 24, 2023, peer-reviewed May 31, 2023, accepted June 07, 2023

Abstract: **Zinc oxide nanoparticles were synthesized and samples of films of polymer composite materials on their basis were obtained and studied. Zinc oxide nanoparticles were synthesized in a plasma discharge under the action of ultrasonic cavitation. To create composites with a homogeneous distribution of nanoparticles, solution technology was used, and then melt compounding technology. Composite materials based on a copolymer of polyethylene and vinyl acetate and zinc oxide nanoparticles were obtained, and not sonicated and sonicated nanoparticles were used. The obtained samples of composite materials were studied by X-ray phase analysis, X-ray fluorescence analysis and scanning electron microscopy. It was shown that there are differences between the samples: in the case of nanoparticles without ultrasonic treatment, the particles are more strongly aggregated inside the composite material and their average size is visually larger than in the case of a sample with nanoparticles subjected to ultrasonic treatment.**

Key words: **nanoparticles, polymers, composite materials, zinc oxide**

PACS: 61.46.+w

Acknowledgments: This work was supported by the Russian Science Foundation, project no. 23-19-00540.

For citation: Nikolay A. Bulychev, Yuri G. Mikhaylov. Obtaining polymer composite materials based on zinc oxide nanoparticles synthesized in a plasma discharge under the action of ultrasound. *RENSIT: Radioelectronics. Nanosystems. Information Technologies,* 2023, 15(2):161-168e. DOI: 10.17725/rensit.2023.15.161.

Contents

1. INTRODUCTION

Currently, composite materials based on various classes of polymers reinforced with nanosized fillers of various compositions and geometries (in the form of spheres, fibers, planar two-dimensional structures, etc.) are actively used in various fields of

science and technology, representing a very competitive alternative to materials from metals and alloys. High specific mechanical characteristics make this class of materials extremely valuable when used as structural materials in industry (aerospace, automotive), as well as in a number of other areas [1–6].

When using nanoparticles based on metals and ceramics and organic polymers as a matrix as fillers, it is necessary to take into account the very weak adhesion of nanoparticles to the material of the polymer matrix, which is due to the chemical inertness of the nanoparticle surface. Obviously, in the absence of chemical interaction between the components of the composite material, a very low level of strength of the interfacial interaction at the nanoparticle-matrix interface will be achieved, and this will negatively affect the physical and mechanical characteristics of the entire resulting material [3, 4]. This effect is especially pronounced when studying films made of such a composite material, where strengthening due to impregnated inclusions is especially important. At present, to increase the strength of interfacial interaction between a polymer and fillers, various methods are used, among which chemical or physical modification of the surface of fillers [7], functionalization of the polymer matrix [8], plasma treatment [9], and in-situ polymerization of the polymer on the surface of the filler are distinguished. [10] etc. A common feature of all the above methods is the formation of reactive functional groups on the surface of the reinforcing particles, capable of forming strong chemical bonds with the matrix polymer. However, it should be taken into account that these methods and approaches should be carried out taking into account the individual characteristics of each specific filler-polymer pair and provide the required level of interfacial interaction in the resulting composite [11–14].

When developing methods, technologies and equipment for obtaining functional and structural composite materials, as well as functional elements from filled polymers, it is also necessary to ensure the physicochemical and physicomechanical characteristics of the materials obtained, which is determined both by the properties of the dispersed filler and by the interaction of the filler and the matrix.

Therefore, in the framework of this work, zinc oxide nanoparticles were synthesized in a plasma discharge under the action of ultrasonic cavitation, and samples of films of polymer composite materials were obtained and studied on their basis.

2. MATERIALS AND METHODS

Zinc oxide nanoparticles were synthesized in a plasma discharge under the action of ultrasonic cavitation according to a previously developed procedure [15–17]. To create composites with a homogeneous distribution of nanoparticles, solution technology was used, and then melt compounding technology using heated laboratory mixing rolls. An ethylene-vinyl acetate copolymer was used as the polymer matrix. The content of vinyl acetate in the copolymer is 28%, the melt flow index is 25 g/10 min.

The copolymer was dissolved in chemically pure butyl acetate at 60°C with stirring with a magnetic stirrer. Powder of nanoparticles was poured into the resulting solution while stirring continued.

An IKA T18 Digital ULTRA TURRAX submersible high-speed disperser was used to break up particle agglomerates in the polymer solution for 10 min at a speed of 10,000 rpm. For ultrasonic treatment of nanoparticles before obtaining a sample, a Technosonic-1000 ultrasonic emitter was used at a frequency of 40 kHz and an intensity of 2 W/cm2 for 2 min. After dispersion, the solutions were dried under draft. The dried samples were then subjected to rolling. Mixing rollers are designed for the preparation and processing of rubber, plastic mixtures with various parameters of technological processes. Before rolling, the crushed components were subjected to conditioning at a temperature of 50±5°C in an oven (Loip, Russia) for 3 hours.

To obtain a composite, the resulting dried concentrate was diluted with pure copolymer granules to a final filler concentration of 1% wt. Melt mixing was carried out on a UBL-6175-BL laboratory mixing roll (Dongguan BaoPin International Precision Instruments Co., Ltd., China). When compounding, the following technological parameters were used: 8 rpm and a gap between the rolls of 1 mm, the temperature regime of the rolls was 130°C and 150°C. Next, the films were pressed on a cellophane substrate using an RPA-12 laboratory hydraulic press (Biolent, Russia) at a temperature of 150°C and a pressure of 20 kgf/cm2.

The identification of the phase composition of the obtained samples was carried out on a Bruker D8 Advance setup operating in reflection mode using Cu-Kα radiation (40 kV, 40 mA, λ = 1.54056 Å). Qualitative determination of the metal in the obtained samples of materials by X-ray fluorescence analysis was carried out on the analyzer Olympus Vanta (Japan) in the GeoChem mode with a 3-beam mode (scanning time: 45 s on each beam). Morphology was studied by scanning electron microscopy on a Carl Zeiss Supra 40-30-87 instrument.

3. RESULTS AND DISCUSSION

As was shown in previous studies, the combined impact on a liquid medium of pulsed or stationary electric fields and high-intensity ultrasonic vibrations above the cavitation threshold leads to the appearance of a special form of electric discharge in a cavitating liquid medium [15–17]. This type of discharge is still a little studied physical phenomenon, which has original electrical and optical characteristics. At the same time, as it was proved earlier, the use of ultrasonic cavitation makes it possible to solve the problem of preventing the agglomeration of synthesized nanoparticles after synthesis and activates their surface, creating additional active adsorption centers on it, which contributes to the effective interaction of such particles with organic polymers and makes it possible to create polymer composite materials with high operational properties [15-17].

Zinc metal electrodes were used as starting materials for the synthesis of nanoparticles. Synthesis was carried out in various liquid media: water, alcohols (ethanol, isopropanol). The nanometer size and high resistance of nanoparticles to aggregation made it possible to obtain relatively stable aqueous disperse systems (suspensions) of nanoparticles without the use of any stabilizing compounds [15–17].

This is explained by the fact that, firstly, ultrasonic action on a liquid-phase medium in the mode of developed cavitation changes the conditions of electrical breakdown between the discharge electrodes in the reaction chamber during the synthesis of nanoparticles due to the fact that cavitation bubbles in a liquid in an electric field are able to line up in chains, thus changing the medium from liquid-phase to vapor-liquid; while the discharge itself has a falling current-voltage characteristic similar to the current-voltage characteristic of an anomalous glow discharge. Optically, this is determined in the form of a more intense glow of the discharge. Secondly, intense ultrasonic cavitation during synthesis ensures efficient dispersion of particles formed [15–17]. In the case of association of nanoparticles, they were additionally ultrasonically dispersed in an aqueous medium for 1 min.

Typical discharge parameters during the synthesis of nanoparticles are: DC voltage 30–60 V, current strength 3–5 A [15–17]. These parameters were chosen, on the one hand, based on the need to ensure stable discharge burning, and, on the other hand, to create reproducible conditions for the synthesis of nanoparticles.

At the next stage of the work, studies were carried out on the introduction of zinc oxide nanoparticles synthesized in a plasma discharge into a polymer matrix to obtain polymer composite materials and study their physical and mechanical properties. At this stage, a copolymer of polyethylene and vinyl acetate was used as a matrix. Composite materials based on zinc oxide nanoparticles were obtained, and

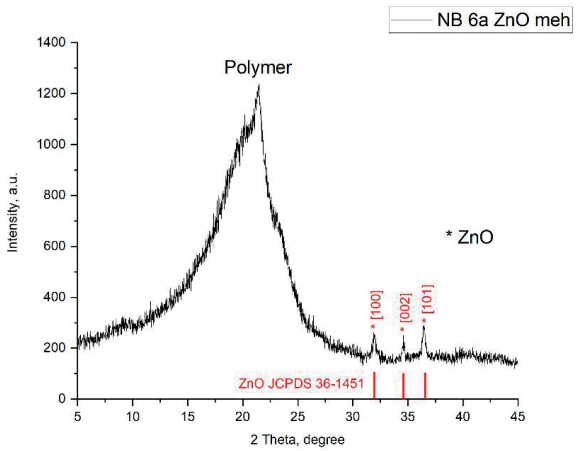

Fig. 1. *Results of the X-ray phase analysis of a sample of a composite material based on nanoparticles without sonication.*

nanoparticles not treated with ultrasound and treated with ultrasound were used.

Figures 1 and **2** present the data of studies of samples of polymer films based on a copolymer of polyethylene and vinyl acetate as a matrix and zinc oxide nanoparticles as a filler by X-ray phase analysis.

According to X-ray diffraction data, the sample contains at least two phases. A strongly broadened peak at 2θ = 22°

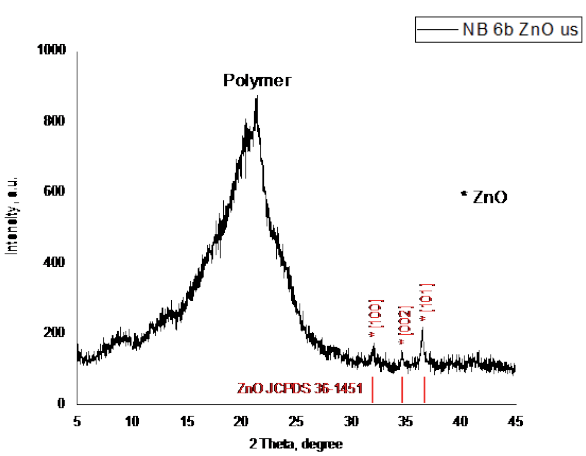

Fig. 2. *Results of X-ray phase analysis of a composite material sample based on nanoparticles after sonication.*

corresponds to the phase of a complex polymer. Also on the diffraction pattern there are peaks at 2θ values: 31.29°, 34.68° and 36.50° corresponding to the zinc oxide phase (JCPDS # 36-1451, wurtzite structure).

According to X-ray phase analysis, the sample with nanoparticles after ultrasonic treatment also contains a complex polymer phase (a strongly broadened peak at 2θ = 21.2°) and peaks at 2θ: 31.90°, 34.61° and 36.52°, corresponding to the oxide phase zinc (JCPDS # 36-1451, wurtzite structure). It should be noted a slight decrease in the intensity of the peak corresponding to the polymer in comparison with the data in Fig. 1, as well as a slight decrease in the intensity of the peaks corresponding to the zinc oxide phase. This may indicate an increase in the interaction of the nanoparticle surface with the polymer when ultrasound is used, as well as a decrease in the size of the filler nanoparticles themselves.

Figures 3 and **4** show the data of studies of samples of polymer films based on a

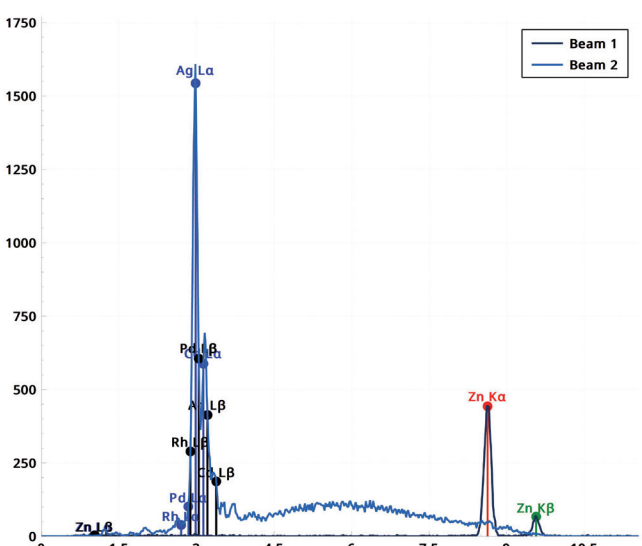

Fig. 3. *Results of X-ray fluorescence analysis of a composite material sample based on nanoparticles without sonication.*

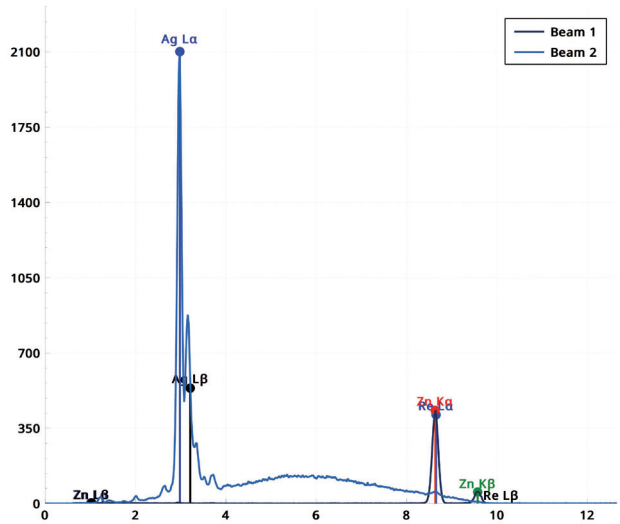

Fig. 4. *Results of X-ray fluorescence analysis of a composite material sample based on nanoparticles after sonication.*

copolymer of polyethylene and vinyl acetate as a matrix and zinc oxide nanoparticles as a filler by X-ray fluorescence analysis.

According to the data of X-ray fluorescence analysis, the presence of zinc oxide nanoparticles was qualitatively confirmed in the sample.

X-ray fluorescence analysis also qualitatively confirmed the presence of zinc oxide in the film sample. In this case, the intensity of the peak increases in comparison with the sample obtained on the basis of nanoparticles without ultrasonic treatment.

Figures 5 and **6** show the data of studies of samples of polymer films based on a copolymer of polyethylene and vinyl acetate as a matrix and zinc oxide nanoparticles as a filler by scanning electron microscopy.

Scanning electron microscopy confirms that the zinc oxide nanoparticles are enclosed within the polymer film. In this case, there are differences between the samples: in the case of nanoparticles

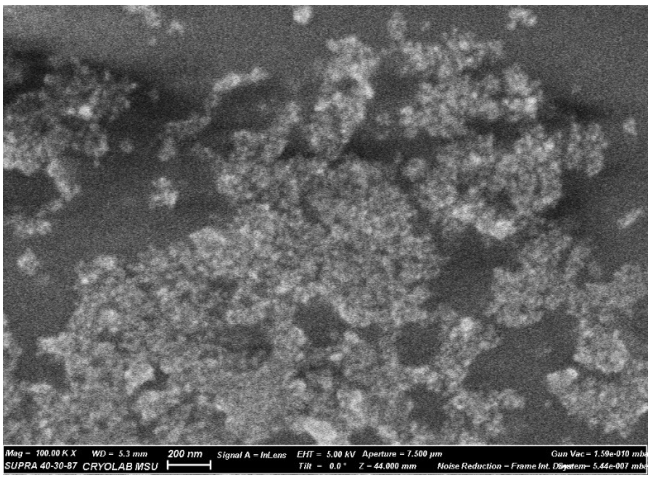

Fig. 5. *Results of a study by scanning electron microscopy of a sample of a composite material based on nanoparticles without sonication.*

without ultrasonic treatment, the particles are more strongly aggregated inside the composite material and their average size is visually larger than in the case of a sample with nanoparticles subjected to ultrasonic treatment.

Thus, as a result of the studies carried out by the methods of physicochemical analysis, it was shown that the activation of the surface of particles using the methods of physical and physicochemical effects is an important factor that can significantly increase the efficiency of interaction between filler particles and the polymer matrix. Among the physical methods, first of all, the effect of intense ultrasound should be noted. The use of methods that would allow the synthesis of filler particles with an activated surface can give a great impetus to the production of composite materials with improved physical and mechanical characteristics [15–17].

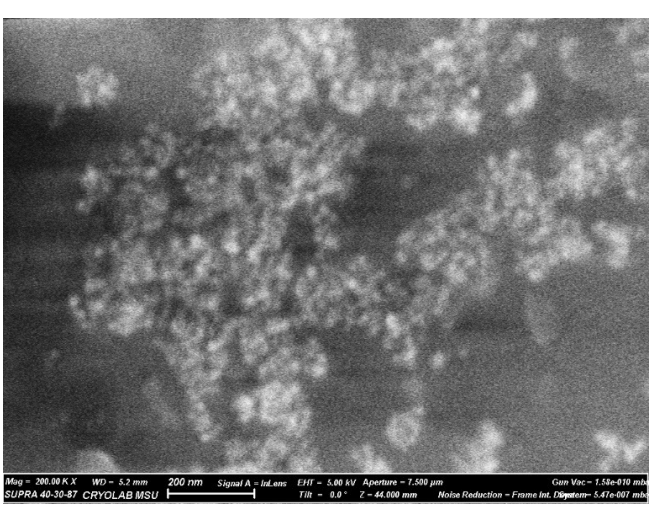

Fig. 6. *Results of a study by scanning electron microscopy of a sample of a composite material based on nanoparticles after sonication.*

4. CONCLUSION

Composite materials in the form of films based on zinc oxide nanoparticles that were not sonicated and sonicated were obtained and studied. According to X-ray diffraction analysis, a sample with nanoparticles after ultrasonic treatment shows a slight decrease in the intensity of the peak corresponding to the polymer. This may indicate an increase in the interaction of the nanoparticle surface with the polymer when ultrasound is used, as well as a decrease in the size of the filler nanoparticles themselves. X-ray fluorescence analysis also qualitatively confirmed the presence of zinc oxide in the film sample. In this case, the intensity of the peak increases in comparison with the sample obtained on the basis of nanoparticles without ultrasonic treatment. Scanning electron microscopy confirms that the zinc oxide nanoparticles are enclosed within the polymer film. In this case, there are differences between the samples: in the case of nanoparticles without ultrasonic treatment, the particles are more strongly aggregated inside the composite material and their average size is visually larger than in the case of a sample with nanoparticles subjected to ultrasonic treatment.

REFERENCES

1. Sai Krishna Samudrala C, Krishna Sai Radhi P, Murthy BS. Metal, ceramics and polymer nano-composites for various applications: A review. Materials Today. *Proceedings*, 2022, 56(3):1120-1128.
2. Nanda T, Singh, Shelly D, Mehta R. Advancements in multi-scale filler reinforced epoxy nanocomposites for improved impact strength: A review. *Critical Reviews in Solid State and Materials Sciences*, 2021, 46:281-329.
3. Pavlović VB, Pavlović VP. Polymer-ceramic nanocomposites and converging technologies. *Encyclopedia of Materials: Composites*, 2021, 2:134-144.
4. Khare V, Srivastava S, Kamle S, Kamath GM. Effect of Filler Functionalization on the Thermo-Mechanical behavior of Polypropylene Nanocomposites. *Procedia Structural Integrity,* 2019, 14:215-225.
5. Pukanszky B. Interfaces and interphases in multicomponent materials: past, present, future. *Eur. Polym. J.*, 2005, 41:645-662.
6. Sharma M, Gao S, Mader E, Sharma H, Wei LY, Bijwe J. Carbon surfaces and composite interphases. *Compos. Sci. Technol.*, 2014, 102:35-50.
7. Wen Z, Xu C, Qian X, Zhang Y, Wang X, Song S, Dai M, Zhang C. A two-step carbon fiber surface treatment and its effect on the interfacial properties of CF/EP composites: The electrochemical oxidation followed by grafting of silane coupling agent. *Appl. Surf. Sci.*, 2019, 486:546-554.
8. Salavagione HJ, Martinez G. Importance of covalent linkages in the preparation of effective reduced graphene oxide-poly(vinyl chloride) nanocomposites. *Macromolecules*, 2011, 44:2685-2692.
9. Lin J, Sun C, Min J, Wan H, Wang S. Effect of atmospheric pressure plasma treatment on surface physicochemical properties of carbon fiber reinforced polymer and its interfacial bonding strength with adhesive. *Composites Part B: Engineering,* 2020, 12:199-205.
10. Rafiee MA, Rafiee J, Srivastava I, Wang Z, Song H, Yu ZZ, Koratkar N. Fracture and fatigue in graphene nanocomposites. *Small,* 2010, 6:179-183.
11. Jeziorska R, Zielecka M, Gutarowska B, Zakowska Z. High density polyethylene composites filled with nanosilica containing inmobilized nanosilver or nanocopper: thermal, mechanical, and bactericidal properties and morphology and interphase characterization. *Int. J. Polym. Sci.,* 2014, 10:1-13.
12. Pourbeyram S, Mohammadi S. Synthesis and characterization of highly stable and water dispersible hydrogel–copper nanocomposite. *J. Non-Crystalline Solids,* 2014, 402:58-63.
13. Xue B, Jiang Y, Li G. Preparation of Cu/Dickite/LLDPE nanocomposites and synergistic effect of exfoliated dickite and nano Cu in LLDPE matrix. *Polymer Composites*, 2013, 34(7):1061-1070.
14. Cárdenas G, Diaz J, Meléndrez MF, Cruzat C, García A. Colloidal Cu nanoparticles/chitosan composite film obtained by microwave heating for food package applications. *Polym. Bull.*, 2009, 62:511-524.
15. Bulychev NA. Preparation of Stable Suspensions of ZnO Nanoparticles with Ultrasonically Assisted

Low-Temperature Plasma. *Nanosci. Techn.: An International J.*, 2021, 12(3):91-97.

16. Bulychev NA, Kolesnik SA. Reinforcement of Polymer Composite Materials by Titanium Dioxide Nanoparticles Synthesized in Plasma Discharge under Ultrasonic Cavitation. *IOP Conf. Proc.*, 2022, 2231:012012.
17. Bulychev NA. Study of Interaction of Surface-Active Polymers with ZnO Nanoparticles Synthesized in Ultrasonically Assisted Plasma Discharge. *Nanosci. Techn. An International J.,* 2022, 13(1):55-65.

DOI: 10.17725/rensit.2023.15.169

Holographic processing of hydroacoustic information using linear antennas

Venedikt M. Kuz'kin
Prokhorov Institute of General Physics of Russian Academy of Sciences, http://www.gpi.ru/
Moscow 119991, Russian Federation
E-mail: kumiov@yandex.ru

Sergey A. Pereselkov, Sergey A. Tkachenko, Nadezhda P. Stadnaya
Voronezh State University, http://www.vsu.ru/
Voronezh 394006, Russian Federation
E-mail: pereselkov@yandex.ru; sega-th@mail.ru, stadnaya.edu@yandex.ru

Yuri V. Matvienko
Institute for Marine Technology Problems, Far Eastern Branch of Russian Academy of Sciences, http://www.febras.ru/
Vladivostok 690091, Russian Federation
E-mail: ymat@marine.febras.ru

Vladimir I. Grachev
Kotelnikov Institute of Radioengineering and Electronics of RAS, http://www.cplire.ru/
Moscow 125009, Russian Federation
E-mail: grachev@cplire.ru

Received May 25, 2023, peer-reviewed May 31, 2023, accepted June 07, 2023

Abstract: **The formation of an interferogram and a hologram of a moving underwater noise source using linear antennas is considered. The relationship between the spectral density of the hologram and the aperture and the angular dependence of the received field is derived. Antenna gain has been estimated. The issue of the limiting signal-to-noise ratio at which the holographic processing remains operational is discussed. An analytical expression is obtained that establishes a relationship between the signal/noise ratios at the output and input of the antenna. Conditions are formulated under which the interferogram of the source is not distorted.**

Keywords: **shallow water area, interferogram, hologram, noise source, linear antenna, signal-to-noise ratio, antenna parameters**

UDC 004.052.34

Acknowledgments: The study was supported by the Russian Science Foundation grant No. 23-61-10024, https://rscf.ru/project/23-61-10024/. Numerical calculations of antenna parameters S.A. Tkachenko were supported by the grant of the Russian Federation President MK-4846.2022.4.

For citation: Venedikt M. Kuz'kin, Sergey A. Pereselkov, Yuri V. Matvienko, Vladimir I. Grachev, Sergey A. Tkachenko, Nadezhda P. Stadnaya. Holographic processing of hydroacoustic information using linear antennas. *RENSIT: Radioelectronics. Nanosystems. Information Technologies*, 2023, 15(2):169-178e. DOI: 10.17725/rensit.2023.15.169.

Contents

1. INTRODUCTION

Currently, one of the topical areas of underwater research is the illumination of the underwater environment, which ensures the detection and localization (resolution, determination of bearing, radial velocity, distance and depth) of moving underwater low-noise sound sources using small-sized antennas. The solution to this problem based on holographic processing based on stable structural features of the interference pattern (interferogram) formed by a noise source is considered in [1−3]. Interferogram refers to the energy characteristics of the received vector-scalar field in frequency-time variables. Holographic processing implements quasi-coherent accumulation of the spectral density of a noise source along localized interferogram fringes in frequency-time variables. During the observation time Δt, in the band Δf, J independent realizations are accumulated with duration t_1 and with a time interval t_2 between them

$$J = \frac{\Delta t}{t_1 + t_2}. \quad (1)$$

Realizations are independent if $t_2 > 1/\Delta f$. Noise accumulation is incoherent. An interferogram is formed in frequency-time variables, to which a two-dimensional Fourier transform is applied. At the output of the integral transformation (hologram), the spectral density is concentrated in a narrow band in the form of focal spots caused by the interference of modes of different numbers. The spectral density of interference is distributed over the entire region. Such processing has a high noise immunity. Based on the location of the spectral densities of holograms and some a priori data on the propagation channel, the problems of detection, direction finding, determination of the radial velocity, distance and resolution of sources are solved.

Holographic processing today is a very active field of research, in which many interesting results of theoretical and practical interest have been obtained. First, a method has been developed for restoring the interferogram of an unperturbed field on a stationary path, when intense internal waves cause horizontal refraction and interaction of acoustic field modes [4–7]. Secondly, a noise-resistant method for detecting and localizing moving low-noise sources, which is stable with respect to the hydrodynamic variability of the oceanic environment, has been proposed [8]. Thirdly, adaptive algorithms for determining the source parameters have been created that do not require knowledge about the characteristics of the propagation medium [9,10]. Further, fourthly, a method is implemented for resolving several sources of different intensities under conditions when their interferograms overlap in frequency and time and are masked by interference [11]. Finally, fifthly, a method has been developed for selecting acoustic field modes and determining their parameters [12–14]. Works [15–18] have played a significant role in the progress in the development of holographic interferometry in shallow water areas.

The purpose of this article is, firstly, to describe holographic processing using linear antennas and consider their characteristics that determine the effectiveness of the work. Secondly, to reveal the reception conditions under which the interferogram of the source is not distorted in the absence of interference.

2. HOLOGRAPHIC PROCESSING USING LINEAR ANTENNAS

Let the number of elements Q_b of the receiving antenna be equal to B, $b = \overline{1, B}$, the interelement distance is d. The received

spectrum of a noise source moving with a radial velocity w at a depth z_s is concentrated in the frequency range $f_1 \le f \le f_2$, where $f_{1,2} = f_0 \pm (\Delta f/2)$, Δf and f_0 are the bandwidth and the average frequency of the spectrum. The fields from each antenna element are summed, and an interferogram is formed at the output, to which a two-dimensional Fourier transform is applied. We will consider the processing using the example of the scalar component of the field, i.e. sound pressure spectrum $p(f,t)$.

2.1. Horizontal line antenna

The layout of the source S and the horizontal linear antenna is shown in **Fig. 1.** The antenna elements are at a depth z_q. The reference element of the antenna is the first element Q_1. The aperture $L = (B - 1)d$ is much smaller than the distance to the source. In this case, $r_b = r_1 - (b - 1)d\sin\theta$, where θ is the angle complementary to the bearing.

When summing the fields from the antenna elements, the difference in distances from the source to its various elements in the direction of the angle θ is compensated. Therefore, the field Q_b of the element is multiplied by the exponential factor $\exp[ih_*(f_0)(b - 1)d\sin\theta_*]$. Here $h_*(f_0)$ is the distinguished real part of the horizontal wavenumber (propagation constant) at the middle frequency f_0 of the source spectrum, θ_* is the compensation angle. The field at the output Q_b of the antenna element can be represented as a sum of modes [19]

$$p_b(f,r_b) = \sum_m A_m(f,r_b)\exp\left\{i\left[h_m(f)r_1 - \right.\right.$$
$$\left.\left. -2(b-1)\left(h_m(f) - h_*(f_0)_*\right)\right]\right\}, \quad (2)$$

where

$$\eta = d\sin\theta/2,\ \eta_* = d\sin\theta_*/2. \quad (3)$$

Here A_m and h_m are the amplitude and propagation constant of the m-mode. Cylindrical field divergence, modal attenuation, source depths zs and antenna element depths zb are taken into account in the modal amplitude. At the antenna output, the field $p_{an}(f,r_1)$, neglecting the dependence of the amplitude on distance, $A_m(f,r_1) \approx A_m(f,r_b)$, we write as

$$p_{an}(f,r_1) = \sum_m A_m(f,r_1) I_m \exp\left\{i\left[h_m(f)r_1 - \right.\right.$$
$$\left.\left. -(B-1)\left(h_m(f)\eta - h_*(f_0)\eta_*\right)\right]\right\}, \quad (4)$$

where

$$I_m(f) = \frac{\sin[B(h_m(f)\eta - h_*(f_0)\eta_*)]}{\sin(h_m(f)\eta - h_*(f_0)\eta_*)}. \quad (5)$$

The antenna interferogram $P_{an}(f,r_1) = |p_{an}(f,r_1)|^2$, according to (4), is equal to

$$P_{an}(f,r_1) = \sum_m \sum_n P_{an}^{(mn)}(f,r_1), \quad (6)$$

$$P_{an}^{(mn)}(f,r_1) = A_m(f,r_1) A_n^*(f,r_1) I_{mn}(f) \times$$
$$\times \exp\left[ih_{mn}(f)\left(r_1 - (B-1)\eta\right)\right], \quad (7)$$

where

$$I_{mn}(f) = I_m(f) I_n(f). \quad (8)$$

Here $h_{mn}(f) = h_m(f) - h_n(f)$. Let at the initial time $t_0 = 0$ the distance $r_1 = r_0$. In interferogram (6), we pass from the distance variable r_1 to the time variable t, $r_1 = r_0 + wt$, and apply the two-dimensional Fourier transform to it.

At the output of the integral transformation (hologram), the spectral density is expressed through the interferogram as

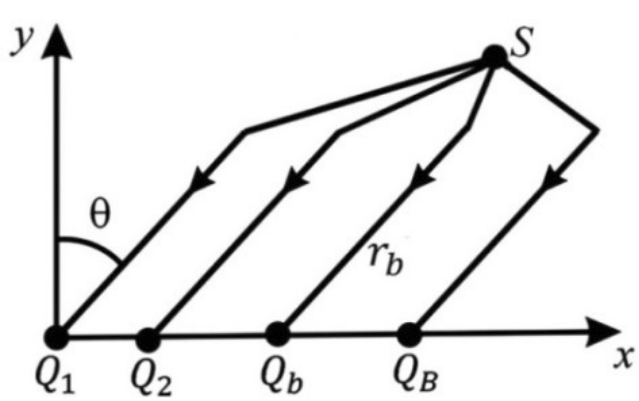

Fig. 1. *Geometry of the problem (view in the horizontal plane): r_b is the horizontal distance of the element Q_b to the source S, θ is the angle of direction to the source.*

$$F_{an}(\nu,\tau)=2\pi\int_0^{\Delta t}\int_{f_1}^{f_2}P_{an}(f,t)\exp[i2\pi(\nu t-f\tau)]dtdf= \\ =\sum_m\sum_n F_{an}^{(mn)}(\nu,\tau), \quad (9)$$

where ν and τ are the frequency and time of the hologram; Δt is the observation time. Using the approach for calculating the hologram of a single receiver [1], for partial antenna holograms, we obtain

$$F_{an}^{(mn)}(\nu,\tau)=2\pi A_m(f_0,r_0)A_n^*(f_0,r_0)I_{mn}(f_0)\Delta f\,\Delta t\times \\ \times\exp\left[i2\pi\left(\frac{\nu\Delta t}{2}-\tau f_0\right)\right]\times \\ \times\exp\left\{i\left[h_{mn}(f_0)\left(\frac{w\Delta t}{2}+r-(B-1)\eta\right)\right]\right\}\times \\ \times\frac{\sin\left\{\pi\left[(r_0-(B-1)\eta+wt_*)\frac{1}{2\pi}\frac{dh_{mn}(f_0)}{df}-\tau\right]\Delta f\right\}}{\pi\left[(r_0-(B-1)\eta+wt_*)\frac{1}{2\pi}\frac{dh_{mn}(f_0)}{df}-\tau\right]\Delta f}\times \\ \times\frac{\sin\left\{[wh_{mn}(f_0)+2\pi\nu]\frac{\Delta t}{2}\right\}}{[wh_{mn}(f_0)+2\pi\nu]\frac{\Delta t}{2}}. \quad (10)$$

Here t_* is the distinguished moment of time on the observation interval Δt, $0 < t_* < \Delta t$. If we set $B = 1$, then $I_{mn}(f_0) = 1$ and formula (10) becomes the corresponding formula for a single receiver [1]. The factor $I_{mn}(f_0)$ (8) determines the distribution of the spectral density of the antenna hologram with respect to a single receiver. The dependences of $I_{mn}(f_0)$ on the angle θ at the compensation angle $\theta_* = 0$ are considered in [20].

2.2. Vertical line antenna

The field at the output of the b-th element at a horizontal distance r from the noise source is written as a sum of modes as [19]

$$p_b(f,r,z_b)=\sum_m\psi_m(z_b)A_m(f,r)\exp[ih_m(f)r], \quad (11)$$

where $\psi_m(z)$ – eigenfunction of the mth mode. In (11), the slow change in the eigenfunction with frequency is neglected. At the output of the antenna, the source field takes the form

$$p_{an}(f,r)=\sum_b p_b(f,r)=\sum_m E_m A_m(f,r)\exp[ih_m(f)r], \quad (12)$$

where

$$E_m=\sum_m\psi_m(z_b). \quad (13)$$

The antenna interferogram, according to (12), is equal to

$$P_{an}(f,r)=\sum_m\sum_n P_{mn}(f,r), \quad (14)$$

$$P_{mn}(f,r)=E_mE_n^*A_m(f,r)A_n^*(f,r)\exp[ih_{mn}(f)r]. \quad (15)$$

Let the initial time $t_0 = 0$ correspond to the distance r_0. In the interferogram (14), we pass from the distance variable r to the time variable t and apply the two-dimensional Fourier transform (9) to it. As a result, for partial antenna holograms, we obtain

$$F_{an}^{(mn)}(\nu,\tau)=2\pi A_m(f_0,r_0)A_n^*(f_0,r_0)\,\mathrm{E}_m\,E_n^*\Delta f\,\Delta t\times \\ \times\exp\left[i2\pi\left(\frac{\nu\Delta t}{2}-\tau f_0\right)\right]\exp\left[ih_{mn}(f_0)\left(\frac{w\Delta t}{2}+r_0\right)\right]\times \\ \times\frac{\sin\left\{\pi\left[(r_0+wt_*)\frac{1}{2\pi}\frac{dh_{mn}(f_0)}{df}-\tau\right]\Delta f\right\}}{\pi\left[(r_0+wt_*)\frac{1}{2\pi}\frac{dh_{mn}(f_0)}{df}-\tau\right]\Delta f}\times \\ \times\frac{\sin\left\{[wh_{mn}(f_0)+2\pi\nu]\frac{\Delta t}{2}\right\}}{[wh_{mn}(f_0)+2\pi\nu]\frac{\Delta t}{2}}. \quad (16)$$

If we put $B = 1$, then relation (16) turns into an expression for a single receiver [1]. The spectral density of the partial holograms of the antenna $F_{an}^{(mn)}$ with respect to a single receiver differs by a weight factor $E_mE_n^*$. For this reason, the regions of localization of the spectral density for the antenna and a single receiver are similar in shape.

3. ANTENNA PARAMETERS

3.1. Amplification factor and directivity characteristic

The effectiveness of holographic processing using receiving antennas characterizes the amplification factor

$$\chi = G_{an}/G_r \quad (17)$$

and directivity characteristic (horizontal antenna)

$$D = G_{an}/\max G_{an}, \quad (18)$$

where

$$G_{an,r} = \iint \left| F_{an,r}(\tau, \nu) \right| d\tau d\nu. \quad (19)$$

Index "*r*" refers to a single receiver. In the compensation angle direction, the amplification factor of horizontal antenna reaches its maximum value $\chi_{\max} \cong B^2$. The amplification factor χ of the vertical antenna is $\chi \approx B^2$. Thus, the amplification factors of the horizontal and vertical antennas are comparable to each other. The results of numerical simulation for considering the amplification factor and directivity characteristics of linear antennas were discussed in [20, 21].

3.2. Limit input signal-to-noise ratio

Holographic processing has certain limitations, which lie in the nature of interference phenomena and the presence of interference. The restriction associated with interference can be conveniently characterized by the limiting (minimum) input signal-to-noise ratio (s/n) $q_{\lim}$, when stable detection and estimates of bearing, radial velocity, distance, and depth are close to real for input s/n $q_0 > q_{\lim}$. In the case of isotropic interference and a single receiver for the scalar component of the noise source field $q_{\lim}^{(r)} \approx 1.5/J^2$ [2]. The estimate was established on the basis of a number of physical considerations and verified on the results of numerical and natural experiments. When using the combinational components of the vector-scalar field, the value $q_{\lim}^{(r)}$ decreases by 2-5 times [2,3]. Let us generalize the estimate of the limiting input s/n ratio of a single receiver to linear antennas.

Let us assume that the noise signal and interference are statistically unrelated random processes and the interference at the input of the antenna elements is not correlated. The second condition is satisfied if $d \geq \lambda/2$, where λ is the wavelength. Then the limit input s/n ratio on the antenna element is estimated as

$$q_{\lim}^{(an)} = \alpha q_{\lim}^{(r)}, \quad (20$$

where $\alpha = B/\chi$. The value of $\chi \approx B^2$, so $\alpha \approx 1/B$. The input s/n ratios on a single antenna element, when the estimates of the source parameters are close to real values, are limited by the inequality $q_0 > q_{\lim}^{(an)}$. If, first, holographic processing is performed on each *b*-th receiver and then the spectral densities of the holograms are summed at the antenna output, then there will be no gain in the limiting s/n ratio with respect to a single receiver.

3.3. Noise immunity

Let us consider how the s/n ratio at the antenna output is related $q_{an}^{(out)}$ to the s/n ratio at the input of the antenna element q_0. Their ratio, as is known, determines the noise immunity of processing

$$\rho_{an} = \frac{q_{an}^{(\text{out})}}{q_0}. \quad (21)$$

When solving this problem, we first analyze the question of the relationship between the s/n ratios $q_r^{(out)}$ at the output and input q_0 of a single receiver.

Let the pressure spectra of the noise signal and interference, which we denote as *s*(*t*,*f*) and *n*(*t*,*f*), be concentrated in the band Δ*f*. Signal and noise are mutually independent Gaussian random stationary processes with zero mathematical expectations. We restrict ourselves to q_0 values satisfying the condition $q_0 > q_{\lim}^{(r)}$. Let us assume that the band Δ*f* contains *W* localized bands of width *δf* and the contrast of the interferogram, i.e. the bands visibility is equal to one. Let us assume that the noise signal field accumulates coherently along the interference fringes, while interferences accumulates incoherently. Strictly speaking, this provision is not fulfilled, however, from the qualitative and quantitative side, as shown by the data of computer simulation and field experiments [1−3,11], the results remain quite meaningful.

The s/n ratio q_0 at the input of a single receiver at the initial time $t = 0$ is understood as the value

$$q_0 = q(0) = \frac{\overline{E}_s(0)}{\overline{E}_n(0)}, \quad (22)$$

where

$$\overline{E}_s(0) = 2\int_0^\infty \overline{|s(0,f)|^2}\,df = 2\Delta f\,\overline{|s(0,f_s')|^2}, \quad (23)$$

$$\overline{E}_n(0) = 2\int_0^\infty \overline{|n(0,f)|^2}\,df = 2\Delta f\,\overline{|n(0,f_s')|^2}, \quad (24)$$

– average signal energies and interference. Here f_s' and f_n' are the selected signal frequencies and noise in the band Δf. The overline means averaging over the ensemble of realizations. In accordance with (23), (24), the input ratio s/n (22) is equal to

$$q_0 = \frac{\overline{|s(0,f_s')|^2}}{\overline{|n(0,f_s')|^2}}. \quad (25)$$

The average signal energies and noise at the output of trajectory accumulation over time Δt can be written in the form of summation of energies over time intervals of duration t_1 along the interference fringes

$$\overline{E}_s(\Delta t) = 2\int_0^\infty \overline{\left|\sum_{j=1}^{J} W s(t_J,f)\right|^2}\,df, \quad (26)$$

$$\overline{E}_n(\Delta t) = 2WJ\sum_{j=1}^{J}\int_0^\infty \overline{|n(t_J f)|^2}\,df. \quad (27)$$

Using the assumption of stationarity of processes, expressions (26), (27) can be reduced to the form

$$\overline{E}_s(\Delta t) = 2W^2J^2\,\overline{|s(f_s'')|^2}\,\delta f, \quad (28)$$

$$\overline{E}_n(\Delta t) = 2WJ\,\overline{|n(f_n'')|^2}\,\delta f, \quad (29)$$

so that at the output of the trajectory accumulation, the ratio s/n is equal to

$$q_r(\Delta t) = \frac{\overline{E}_s(\Delta t)}{\overline{E}_n(\Delta t)} = WJ\,\frac{\overline{|s(f_s'')|^2}}{\overline{|n(f_n'')|^2}}. \quad (30)$$

Here f_s'' and f_n'' – selected signal frequencies and interference in the band δf.

Using the input ratio s/n (25), we represent expression (30) in the form

$$q_r(\Delta t) = JW\,\frac{\overline{|s(f_s'')|^2}}{\overline{|n(f_n'')|^2}}\,\frac{\overline{|n(f_n')|^2}}{\overline{|s(f_s')|^2}}\,q_0. \quad (31)$$

At the initial moment of time, the average energies of the signal (23) and interference (24) can also be expressed as

$$\overline{E}_s(0) = 2W^2\,\overline{|s(f_s'')|^2}\,\delta f, \quad (32)$$

$$\overline{E}_n(0) = 2W\,\overline{|n(f_n'')|^2}\,\delta f. \quad (33)$$

From a comparison of expressions (23), (24) and (32), (33) we find

$$\overline{|s(f_s')|^2}\,\Delta f_1 = W\,\overline{|s(f_s'')|^2}\,\Delta f_2, \quad (34)$$

$$\overline{|n(f_n')|^2}\,\Delta f_1 = W\,\overline{|n(f_n'')|^2}\,\Delta f_2. \quad (35)$$

and then expression (32) takes the form

$$q_r(\Delta t) = Jq_0, \quad (36)$$

so that at the output of trajectory accumulation, the s/n ratio does not depend on the number of interference fringes W and their width δf, and is proportional to the input s/n ratio q_0 up to a factor J.

Thus, the multiple coherent summation of the interference maxima of the wave field of the noise source along the localized fringes increases the output s/n ratio $q_r(\Delta t)$ by a factor of J with respect to the input value q_0. Such an increase becomes clear if we draw an analogy with the coherent spatial processing of a multi-element antenna containing J receivers: with respect to a single receiver, the s/n ratio increases by a factor of J.

Recording an interferogram onto a hologram and clearing the region of spectral density localization from interference leads to an additional increase in the output s/n ratio compared to $q_r(\Delta t)$. The two-dimensional Fourier transform of the interferogram

localizes the two-dimensional spectral density of the noise signal within a narrow band of the hologram, the area of which can be estimated as

$$S_s = \frac{\tau_*}{\Delta t}. \quad (37)$$

Here τ_* is the position of the main maximum of the focal spot on the time axis due to interference between the extreme modes. The spectral noise density is distributed over the entire region of the hologram, the area of which is equal to

$$S_n = |\nu_*|\tau_*, \quad (38)$$

where ν_* is the position of the main maximum of the focal spot on the frequency axis due to interference between the extreme modes. During the integral transformation, the energy does not change.

Assuming the interference power to be uniformly distributed in the hologram region, the s/n ratio at the output of holographic processing can be represented as

$$q_r^{(out)} = \gamma q_r(\Delta t), \quad \gamma = S_n / S_s, \quad (39)$$

where the concentration coefficient, according to (37), (38), $\gamma = |\nu_*|\Delta t$. In the case of a stationary source, the quantity ν_* is replaced by the spectral width $\Delta\nu$ in the region of the hologram. In accordance with (36), expression (39) takes the form

$$q_r^{(out)} = J\gamma q_0. \quad (40)$$

Thus, the noise immunity of holographic processing using a single receiver is estimated as

$$\rho_r = J\gamma. \quad (41)$$

It is easy to see how the output s/n ratio at the output of the antenna can be estimated. According to (10), (16), the value of the concentration coefficient γ does not change. Taking into account that the noise signal and interference are accumulated coherently and incoherently, the s/n ratio at the antenna output, with respect to a single receiver, increases by $1/\alpha = \chi/B \approx B$ times. Therefore, the s/n ratio at the output of the antenna will be

$$q_{an}^{(out)} = (J\gamma / \alpha)q_0. \quad (42)$$

4. CRITERIA FOR FORMING A UNDISTORTED INTERFEROGRAM

The formation of an interferogram, respectively, and a hologram, is affected by background interference, spatio-temporal inhomogeneities of the propagation medium, and reception conditions. At present, the state of the art on the influence of distorting factors on the formation of an interferogram is mainly concentrated on such aspects as interference [1-3] and intense internal waves [4-8].

In this section, we consider the influence of reception conditions – bandwidth and accumulation time – on the formation of an undistorted interferogram in a regular waveguide in the interference absence. Based on the fact that the interference pattern of the sound source is characterized by frequency $\Lambda_f^{(mn)}$ and time $\Lambda_t^{(mn)}$ scales of variability due to the interference of the *m*-th and *n*-th modes [19]

$$\Lambda_f^{(mn)} = \frac{2\pi}{r\left|dh_{mn}(f_0)/df\right|}, \ \Lambda_t^{(mn)} = \frac{1}{\left|wh_{mn}(f_0)\right|}, \quad (43)$$

let us establish the following two criteria for the formation of an undistorted interferogram. For any pair of (*m,n*) modes:

I. The frequency range $f_1 \le f \le f_2$ should not be less than the frequency period of interferogram variability

$$\Delta f \ge \Lambda_f^{(mn)}. \quad (44)$$

II. The observation time Δt should not be less than the time period of interferogram variability

$$\Delta t \ge \Lambda_t^{(mn)}. \quad (45)$$

Conditions (44), (45) imply certain restrictions on the bandwidth and observation time depending on the distance, radial velocity,

and time-frequency scales of the variability of the transfer function of the medium during the formation of an undistorted interferogram. Reducing the distance and increasing the average frequency of the spectrum leads to the requirement to increase the bandwidth. The latter is due to the fact that, as the frequency increases, the group velocities of the modes $u_m(\omega_0) = d\omega/dh_m(\omega_0)$ asymptotically tend to a value that does not depend on the mode number [19]. A decrease in the radial velocity and the average frequency of the spectrum cause an increase in the observation time. The criteria are most critical with respect to the numbers of neighboring modes.

Criterion I excludes the possibility of the formation of an interferogram due to the interference of (*m, n*) modes with a uniform spectral density, i.e. in a band of infinite width, when localized bands are not observable. It is useful to note that the violation of condition (44) with respect to all pairs of interfering modes leads to a spectral density in the hologram in the form of a single focal spot at the origin. A different situation is observed when condition (45) is not met, when the observation time is not enough for the source to intersect the spatial scales of the variability of the interference pattern. In this case, the position of the peak of the focal spot formed by such interfering modes is shifted to the time axis of the hologram, since the interferogram is formed with respect to them by a stationary source. The formulated conditions (44) and (45) make it possible to estimate the bandwidth and observation time to reduce the error in reconstructing the parameters of a moving noise source.

5. CONCLUSION

Holographic processing of hydroacoustic information has made it possible to change the solution of the problem of detection and localization of moving low-noise underwater noise sources in the most significant way. It turned out to be possible to establish, in the most general case, simple and transparent relationships between the measured characteristics of the spectral density of a hologram and the parameters of a low-noise underwater source. This gave the holographic processing a certain completeness and very tangible advantages compared to other types of processing in solving specific problems of monitoring the underwater situation with a small input noise signal against the background of interference. As a result, a radical simplification of the solution of the problem of detecting and localizing the source of underwater noise has been achieved, and, at the same time, a significant expansion of the range of problems that can be solved in general. For example, with a small input s/n ratio against the background of space-time inhomogeneities and in the absence of information about the hydroacoustic characteristics of the propagation medium.

The paper presents the theory of holographic processing of hydroacoustic information using linear horizontal and vertical antennas. The structure of interferograms and holograms is considered. Expressions for the gain and directivity characteristics are given. The limiting input ratio s/n is estimated, above which the parameters of the noise source of the sound are adequately restored. A connection is established between the output and input s/n relations. The relations obtained allow us to consider a wide range of problems of monitoring the underwater situation using linear antennas. Restrictions on the bandwidth and observation time are formulated, which ensure the minimum error in the reconstructed parameters of the noise source.

REFERENCES

1. Kuznetsov GN, Kuz'kin VM, Pereselkov SA. Spectrogram and sound source localization in a shallow sea. *Acoustic Journal,* 2017, 63(4):406-418.
2. Kuznetsov GN, Kuz'kin VM, Pereselkov SA, Kaznacheev IV, Grigor'ev VA. Interferometric method for estimating the velocity of a noise sound source and the distance to it in shallow water using a vector-scalar receiver. *Phys. Wave Phenom.*, 2017, 25(4):299-306.
3. Kaznacheev IV, Kuznetsov GN, Kuz'kin VM, Pereselkov SA. Interferometric method for detecting a moving sound source by a vector-scalar receiver. *Acoustic Journal,* 2018, 64(1):33-45.
4. Kuz'kin VM, Pereselkov SA, Zvyagin VG, Malykhin AYu, Prosovetskiy DYu. Intense internal waves and their manifestation in interference patterns of received signals on oceanic shelf. *Phys. Wave Phenom.*, 2018, 26(2):160-167.
5. Badiey M, Kuz'kin VM, Lyakhov GA, Pereselkov SA, Prosovetskiy DYu, Tkachenko SA. Intense internal waves and their manifestation in the interference patterns of received signals on oceanic shelf. Part II. *Phys. Wave Phenom.,* 2019, 27(4):313-319.
6. Kuz'kin VM, Lyakhov GA, Pereselkov SA, Kaznacheeva ES. Transmission of information through a randomly inhomogeneous oceanic medium. *Fundam. appl. hydrof.,* 2021, 14(2):54-64.
7. Kaznacheeva ES, Kuz'kin VM, Pereselkov SA. Interferometric processing of hydroacoustic information in the presence of intense internal waves. *Phys. Wave Phenom.*, 2021, 29(3):278-284.
8. Kuz'kin VM, Pereselkov SA, Kaznacheeva ES, Grachev VI, Tkachenko SA, Rybyanets PV. Holographic processing of moving sources in a shallow sea in the presence of intense internal waves. *RENSIT: Radioelectronics. Nanosystems. Information Technology,* 2022, 14(2):197-204. DOI: 10.17725/rensit.2022.14.197.
9. Kaznacheeva ES, Kuznetsov GN, Kuz'kin VM, Lyakhov GA, Pereselkov SA. Measurement capability of the interferometric method of sound source localization in the absence of data on the waveguide transfer function. *Phys. Wave Phenom.,* 2019, 27(1):73-78.
10. Kaznacheeva ES, Kuz'kin VM, Lyakhov GA, Pereselkov SA, Tkachenko SA. Adaptive algorithms for interferometric processing. *Phys. Wave Phenom.*, 2020, 28(3):267-273.
11. Kuz'kin VM, Kuznetsov GN, Pereselkov SA, Grigor'ev VA. Resolving power of the interferometric method of source localization. *Phys. Wave Phenom.,* 2018, 26(2):150-159.
12. Kuz'kin VM, Matvienko YuV, Pereselkov SA, Prosovetskii DYu, Kaznacheeva ES. Mode selection in oceanic waveguides. *Phys. Wave Phenom.*, 2022, 30(2):111-118.
13. Kuzkin VM, Pereselkov SA, Kaznacheeva ES, Grachev VI, Tkachenko SA, Rybyanets PV. Isolation of modes of a noise source in a shallow sea by holographic interferometry in the presence of intense internal waves. *RENSIT: Radioelectronics. Nanosystems. Information Technology,* 2022, 14(3):279-286. DOI: 10.17725/rensit.2022.14.279.
14. Kuz'kin VM, Matvienko YuV, Pereselkov SA, Kaznacheeva ES, Tkachenko SA. Holographic method for mode selection in a shallow sea in the presence of intense internal waves. *Phys. Wave Phenom.,* 2022, 30(5):314-320.

15. Zurk LM, Rouseff D. Striation-based beamform-ing for active sonar with a horizontal line array. *J. Acoust. Soc. Am.,* 2012, 132(4):EL264-EL270.
16. Cockrell KL, Schmidt H. Robust passive range estimation using the waveguide invariant. *J. Acoust. Soc. Am.,* 2010, 127(5):2780-2789.
17. Bonnel J, Touze GLe, Mars JI. Physics-based time-frequency representations for underwater acoustics: Power class utilization with waveguide invariant approximation. *IEEE Signal Process. Mag.,* 2013, 30(6):120-129.
18. Emmetiere R, Bonnel J, Cristol X, Gehant M, Chonavel T. Passive source depth discrimination in deep-water. *IEEE J. of Selected Topics in Signal Processing*, 2019, 13(1):185-197.
19. Brekhovskikh LM, Lysanov YUP. *Theoretical Foundations of Ocean Acoustics*. Moscow, Nauka Publ., 2007, 370 p.
20. Kaznacheev IV, Kuz'kin VM, Kutsov MV, Lyakhov GA, Pereselkov SA. Interferometry in acoustic-data processing using extended antennas. Space–time analogy. *Phys. Wave Phenom.*, 2020, 28(4):326-332.
21. Kuz'kin VM, Matvienko YuV, Pereselkov SA, Kaznacheeva ES. Interferometric processing using a vertical linear antenna. *Vestn. MSU. Series: Physics. Mathematics*, 2020, 2:14-23.

DOI: 10.17725/rensit.2023.15.179

The problems of scaling components in streaming data processing systems

George G. Bulychev, Alexey V. Chernykh
MIREA-Russian Technological University, https://www.mirea.ru/
Moscow 119454, Russian Federation
E-mail: geo-bulychev@mail.ru, meidm@yandex.ru

Received April 24, 2023, peer-reviewed April 30, 2023, accepted May 08, 2023

Abstract: **The article examines the existing problems of scaling components in streaming data processing systems. The algorithm proposed by the authors significantly reduces the number of operations for creating and removing components when scaling the system. The algorithm is based on linear regression. For the proposed algorithm, the practical load on the system is simulated to confirm the theoretical results obtained.**

Keywords: **streaming data processing, scaling, big data**

UDC 004.62

For citation: George G. Bulychev, Alexey V. Chernykh. The problems of scaling components in streaming data processing systems. *RENSIT: Radioelectronics. Nanosystems. Information Technologies*, 2023, 15(2):179-184e. DOI: 10.17725/rensit.2023.15.179.

Contents

1. INTRODUCTION

In the conditions of the modern information society, characterized by gigantic volumes of data [1], constantly arriving in real time, the relevance and importance of streaming data processing [2] is steadily growing. This approach to information processing involves immediate analysis and processing of data, unlike the classical approach with data storage and post-processing.

The main advantage of streaming data processing systems is the ability to quickly make decisions based on fresh and up-to-date information, which allows organizations and specialists to adapt to dynamically changing conditions and maintain competitiveness in the market. However, along with the growing scale and complexity of data processing flows, a number of technical and conceptual problems arise. In particular, algorithms for scaling components in streaming data processing systems face requirements related to efficiency, reliability and flexibility.

The need to quickly and efficiently allocate resources between data processing nodes creates problems in determining the optimal amount of resources for each node to ensure high performance and reliability of the system. Incorrect scaling can lead to reduced performance, additional resource costs, and difficulty processing data in real time.

2. ANALYSIS OF EXISTING ALGORITHMS

Existing streaming data processing systems use a scaling algorithm with a threshold value [3] due to the high decision-making speed.

2.1. Scaling algorithm with a threshold value

The scaling algorithm with a threshold value is based on determining the threshold values of the load on the system nodes. If the load on a node exceeds a certain threshold, the system automatically scales to distribute the load.

The result of the algorithm is the number of component entities - a value that characterizes the required number of copies of the component to process the incoming load.

The number of component entities is calculated using the formula:

$$C_t = N_{t-1}/M, \quad (1)$$

where C_t – is the number of component entities at time t, N_{t-1} – is the load on the system at time t - 1, M – is the threshold value of the load.

As can be seen from the formula, the algorithm does not predict the load and operates only with known values. This feature leads to a "lag" of the algorithm from the current load. With a jumpy load schedule, the system will adjust to the load with a lag, performing an excessive number of operations for creating and deleting component entities.

3. LOAD FORECASTING ALGORITHMS

To scale components efficiently, it is necessary to reduce the number of operations for creating and deleting component entities. To fulfill this requirement, it is necessary to implement a load prediction algorithm. The problem of load forecasting can be reduced to the problem of time series forecasting (since the load is directly related to the time series).

However, in the context of an existing task, the algorithm should have a minimum decision delay time and use a minimum number of resources. Otherwise, the algorithm will work with a strong delay or with a significant increase in resource consumption, thereby leveling the savings caused by a decrease in the number of operations for creating or deleting component entities.

These features do not allow using algorithms based on: neural networks [4], random forest [5] and most other machine learning algorithms [6,7]. However, the linear regression algorithm [8] and exponential smoothing [9] fall under these requirements.

3.1. Linear regression algorithm

Linear regression is a statistical machine learning method used to model the relationship between a dependent variable and one or more independent variables. In the context of load forecasting, the dependent variable can be the load on the system, and the independent variables are factors that affect the load (for example, time of day, day of the week, traffic volume).

Mathematically, linear regression is described as:

$$C_{t+1} = \frac{\overline{Y}_{t+1}}{M}, \quad \overline{Y}_{t+1} = \delta \cdot N_t + \varepsilon, \quad (2)$$

where C_{t+1} – is the number of component entities at time $t + 1$, $\overline{Y}_{t+1}$ – is the predicted

load at time $t + 1$, M – is the threshold value of the load, N_t – load on the system at time t, δ,ε – regression coefficients.

The linear regression coefficients are selected using the least squares method.

3.2. Exponential smoothing algorithm

Exponential smoothing is a time series forecasting method that takes into account all observations in the past by assigning exponentially decreasing weights to them. Thus, newer observations have a greater impact on the forecast than older ones.

To solve the existing problem, the algorithm of triple exponential smoothing (the Holt-Winters method [10]) will be optimal, since this algorithm takes into account trends and seasonality, and most of the processed messages are characterized by these features.

The mathematical algorithm is described as:

$$\begin{aligned} &C_{t+h} = \frac{\overline{Y}_{t+h}}{M}, \\ &\overline{Y}_{t+h} = A(t) + h \cdot B(t) + S(t - p + 1 + (h-1) \bmod p), \\ &A(t) = \alpha \cdot (N_t - S(t-p)) + (1-\alpha) \cdot (A(t-1) + B(t-1)t), \\ &B(t) = \beta \cdot (A(t) - A(t-1)) + (1-\beta) \cdot B(t-1), \\ &S(t) = \gamma \cdot (N_t - A(t)) + (1-\gamma) \cdot S(t-p), \end{aligned} \quad (3)$$

where C_{t+h} – is the number of component entities at time $t + h$, $\overline{Y}_{t+h}$ – is the predicted load at time $t + 1$, M – is the threshold value of the load, N_t – is the load on the system at time t, A – is the equation describing the smoothed series, B – is the equation for estimating the trend, S – is the equation for estimating seasonality, α – is the constant value determining the effect of the smoothed series, β – is the constant value determining the effect of the trend, γ – is the constant values determining the effects of seasonality, p – the period of seasonality.

For the algorithm to function, it is necessary to determine constant values. However, for most components it is impossible to estimate them in advance.

4. MODELING

4.1. Key indicators

Using the algorithm should lead to:

- Reducing the number of operations for creating and deleting components.
- Reducing the delay in processing messages from the moment they arrive in the line. For streaming data processing systems, the critical parameter is the processing time of each message.
- Reducing the maximum and average line size. The system is modeled using the example of one component, however, in the target system, the number of components and lines can be in the thousands, and with a significant increase in the line size of each component, the total memory consumption of the system can offset the resource savings obtained by reducing the number of scaling operations.

The target algorithm should show the minimum value of the specified parameters during modeling.

The algorithm should use minimal resources to predict the load.

To evaluate all of the above parameters, the following metrics are selected:

- Number of operations for creating and deleting component entities.
- Average delay time of message processing.
- Maximum line size.
- Average line size.
- Changing the amount of memory consumed.

4.2. Modeling context

Consider a system consisting of a single component – a message handler in public code repositories ($A1$) and a queue ($Q1$) that receives messages for processing (**Fig. 1**). Processing of these messages allows you to identify leaks

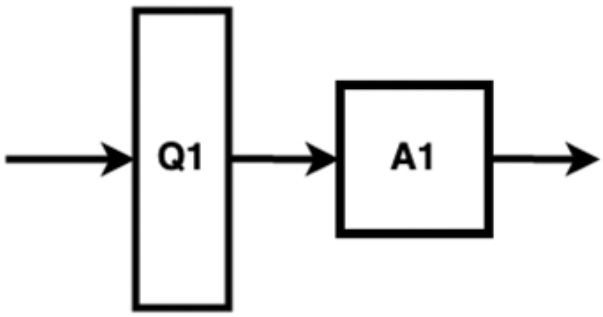

Fig. 1. *Processing system with queue.*

of source code or confidential information of companies.

During the simulation process, each algorithm receives information about the current load and returns – the number of component entities to be started or deleted at the next time.

Events on the github.com for the period from 2022-01-01 15:00:00 to 2022-01-12 02:51:46.

Additional modeling parameters are shown in **Table 1**.

Table 1

Modeling parameters

Parameter	Meaning
A1 performance	50 messages per second
Total number of messages	30 715 323
Time to start or delete entities	1 second

4.3. Modeling an algorithm with a threshold value

When modeling the algorithm with a threshold value, memory consumption was fixed.

As a result (**Table 2**) of the modeling, a minimal delay in message processing was achieved, but a huge number of operations for creating and deleting components.

Table 2

Results of modeling the algorithm with a threshold value

Parameter value	Number of operations
Number of scaling operations	81 746 850
Average queue size	3.534165161
Average message delay time	0.156226077
Maximum queue size	140

Table 3

Modeling results of the exponential smoothing algorithm

Parameter value	Number of operations
Number of scaling operations	148 122 776
Average queue size	10.47011898
Average message delay time	0.46282659
Maximum queue size	415

4.4. Modeling of the exponential smoothing algorithm

To model the algorithm, it is necessary to determine three constants:

- The effect of a smoothed series.
- Trend influence.
- Influence of seasonality.

However, before the load is formed and analyzed, it is impossible to correctly determine these parameters. The following values were randomly selected for modeling:

- The effect of the smoothed series – 0.4.
- Trend impact – 0.1.
- The influence of seasonality – 0.02.

As a result of the algorithm modeling, the memory consumption was fixed.

The algorithm showed results (**Table 3**) significantly worse than the algorithm with a threshold value. The number of operations is higher than 1.8 times, and the average delay is more than twice as compared to the algorithm with a threshold value.

4.5. Modeling a linear regression algorithm

When modeling the linear regression algorithm, memory consumption was fixed.

The algorithm showed a decrease in the number of operations for creating and deleting components by more than 740 times. However, message latency and queue size have increased significantly.

The result obtained (**Table 4**) can be explained by the fact that the algorithm

Table 4

Modeling results for linear regression

Parameter value	Number of operations
Number of scaling operations	109 596
Average queue size	7.624188911
Average message delay time	0.337023616
Maximum queue size	539

effectively smoothes the spikes and drops of the load to the average value and correctly determines trends.

4.6. Conclusions based on the modeling results

The algorithm with exponential smoothing is not applicable for this problem since it is necessary to strictly determine the initial constants to work correctly.

The linear regression algorithm showed a significant reduction in the number of component creation and deletion operations, compared to the classical threshold algorithm: 109,596 vs. 81,746,850 operations. However, the message delay time increases from 0.156 to 0.337 seconds.

The use of the linear regression algorithm allows to achieve a significant reduction in resource consumption with a minimal increase in delay time.

5. CONCLUSION

Using the linear regression algorithm for scaling components allows to significantly reduce the operations of creating and removing components (by more than 700 times), but the delay in message processing increases. This peculiarity can be leveled by adding a time window, on the basis of which the load forecasting will be performed.

By using the proposed algorithm for load prediction and the marking algorithm [11] for message routing in a stream processing system, it is possible to achieve a reduction of more than 800 times in the number of component scaling operations.

The proposed algorithms can be embedded in systems built on microservice [12] architecture. Thanks to the developed algorithms, resource consumption is significantly reduced, both when processing large amounts of data and when solving applied tasks.

REFERENCES

1. Volume of data/information created, captured, copied, and consumed worldwide from 2010 to 2020, with forecasts from 2021 to 2025 // https://www.statista.com/statistics/871513/worldwide-data-created/ (accessed: 24.04.2023)
2. Loshin D. *ETL (Extract, Transform, Load): Business Intelligence*. USA, Silver Spring, Morgan Kaufmann Publ., 2012, 400 p.
3. Chandrima R, Kashyap B, Sandeep A, Manjusha P. Horizontal Scaling Enhancement for Optimized Big Data Processing: *Proceedings of IEMIS*. *Emerging Technologies in Data Mining and Information Security,* 2019, 639-649 p.p. DOI: 10.1007/978-981-13-1951-8_58.
4. Oancea B, Ciucu S. Time series forecasting using neural network. //https://arxiv.org/pdf/1401.1333.pdf (accessed: 24.04.2023)
5. Random Forests for Time Series // https://hal.science/hal-03129751/file/Block_bootstrap_for_random_forests.pdf (accessed: 24.04.2023)
6. Machine Learning Algorithms for Time Series Analysis and Forecasting //https://arxiv.org/abs/2211.14387 (accessed: 24.04.2023)
7. Gianluca B, Souhaib B, Yann-Aël B. Machine Learning Strategies for Time Series Forecasting. *Lecture Notes in Business Information Processing 138*, 2013, 62-77 p.p. DOI: 10.1007/978-3-642-36318-4_3.
8. Dastan H, Adnan M. A Review on Linear Regression Comprehensive in Machine

Learning. *Journal of Applied Science and Technology Trends,* 2020, 140-147 p.p. DOI: 10.38094/jastt1457.

9. Handanhal V. Forecasting With Exponential Smoothing – What's The Right Smoothing Constant? *Review of Business Information Systems,* 2013, 117-126 p.p. DOI:10.19030/rbis.v17i3.8001.
10. Chatfield C. The Holt-Winters Forecasting Procedure. *Journal of the Royal Statistical Society,* 1978, 264-279 p.p. DOI: 10.2307/2347162.
11. George G. Bulychev, Alexey V. Chernykh. Problems of Message Routing Algorithms in Streaming Data Processing Systems. *RENSIT: Radioelectronics. Nanosystems. Information Technologies,* 2022, 14(3):279-290e. DOI: 10.17725/rensit.2022.14.279.
12. Al-Debagy O, Martinek P. A Comparative Review of Microservices and Monolithic Architectures. *18th IEEE International Symposium on Computational Intelligence and Informatics*, 2018. DOI: 10.1109/CINTI.2018.8928192.

DOI: 10.17725/rensit.2023.15.185

Application of Chimeric Meshes for Explicit Accounting for Inhomogeneities in Modeling the Propagation of Elastic Waves

Ivan A. Mitskovets

Moscow Institute of Physics and Technology, https://mipt.ru/

Dolgoprudny 141701, Moscow Region, Russian Federation

E-mail: mitkovets@phystech.edu

Received May 04, 2023, peer-reviewed May 11, 2023, accepted May 18, 2023.

Abstract: **The method of chimeric meshes is applied to simulate the propagation of elastic perturbations in media containing porous and fractured inclusions. A model of a linearly elastic isotropic medium is considered, which describes the state of a geological rock. The grid-characteristic method with the third-order accurate Rusanov scheme is used for numerical modeling of the dynamic propagation of elastic disturbances. Special attention is paid to the presence of separate inclusions of pores or fractures, which introduce heterogeneity into the medium and can substantially influence the response of elastic disturbances. The use of the chimera grid method allows for both the position and shape of such inclusions to be described explicitly, taking into account their influence on the propagation of elastic disturbances. As a result of the conducted investigation, a methodology for numerical modeling of the propagation of elastic disturbances in media with porous and fractured inclusions was developed, which can be used to assess the influence of such inclusions on the dynamic response of elastic disturbances. The presented results can be applied in geophysical and seismic research related to modeling the dynamics of various processes in soils and rocks.**

Keywords: **grid-characteristic method, chimera grids, elastic wave, pores, cracks**

UDC 519.633.2

For citation: Ivan A. Mitskovets. Application of Chimeric Meshes for Explicit Accounting for Inhomogeneities in Modeling the Propagation of Elastic Waves. *RENSIT: Radioelectronics. Nanosystems. Information Technologies*, 2023, 15(2):185-192e. DOI: 10.17725/rensit.2023.15.185.

Contents

1. INTRODUCTION

Seismic exploration is one of the oldest and most widespread methods used to search for and explore hydrocarbon deposits. Its main purpose is to determine the structure of the subsurface based on ground and well observation data. However, no less important element of this method is the description of the process of propagation of seismic waves from the source into the geological environment. This allows tasks such as refining hydrocarbon reserves in areas with a high well activity, generating synthetic seismograms for regional studies, and refining the presence and characteristics of hydrocarbons in known geological structures to be solved. Significant progress in this area is achieved by using numerical modeling of the propagation of seismic waves in reliable geological models,

as it allows for the creation of arbitrary internal structures of the environment and the estimation of the synthetic response signal.

In this paper, we consider a method for studying spatial dynamic processes occurring in geological environments with porous and fractured inclusions in the process of seismic exploration. The grid-characteristic method is used for numerical integration of emerging systems of partial differential equations [1,2].

Geological rocks containing porous and fractured inclusions are one of the main sources of hydrocarbons, but understanding their structure and properties remains a difficult task for geologists. This is due to the fact that such structures have a complex geometry and their properties can vary depending on many factors, such as a combination of porosity, permeability and pore density. One of the tasks that can be solved by studying dynamic processes in geological environments with porous and fractured inclusions is to determine the optimal places for hydrocarbon production. Developed network of microcracks and relatively high porosity play an important role in the extraction of natural gas in dense gas-bearing sandstone reservoirs. These structures can be used for controlled gas storage and migration due to their low porosity and permeability [3].

At the same time, the development of natural microcracks contributes to the formation of a network of pore-cracks during hydraulic fracturing, which is also an important factor in the production of hydrocarbons. Wave scattering on porous inhomogeneities makes significant changes in the nature of elastic wave propagation, which was shown in [4].

Classical works, in the construction of which it is assumed that the pores are equally distributed in volume, such as the Gassman or Bio models [5,6,7], do not allow taking into account all the features of the distribution of porous inclusions. This necessitates the creation of models that allow us to describe the physical properties of such structures with maximum accuracy, describing their shape [8,9] and including the seismic characteristics of pores and microcracks. Solving the inverse problem based on seismic data is one of the ways to create such models. This approach allows you to create a model of the geological structure under the surface and determine the optimal places for drilling wells. The use of models that take into account various physical properties of pores and microcracks makes it possible to predict and detect manifestations associated with the extraction of hydrocarbons, and to control such processes.

2. MATERIALS AND METHODS

The concept of chimeric (overset) grids arose from the need to model multicomponent systems in which each component requires an optimal grid adapted to its shape. By implementing an arbitrary overlap between adjacent grids in an overlapping system, each grid can be generated independently. The emphasis when creating a grid can be focused on maintaining high quality cells, such as orthogonality and cell size. The flexibility of this approach usually leads to significantly better grid quality compared to hierarchical grids, where grid points on the borders of neighboring zones must completely coincide. In addition, the overset grid approach allows you to identify local geometry changes, such as adding or removing components, without the need for a complete restructuring of the grid system.

When using the method of chimeric grids, which can include various numerical methods, including the grid-characteristic

method, to solve problems related to the calculation of physical parameters describing the behavior of the medium at subsequent points in time, it is possible to perform calculations independently in the main computational grid and in chimeric grids at each time step separately. After completing the simulation of the propagation of disturbances at this time step in all chimeric and basic grids, it is necessary to interpolate the values of the physical state of the medium from the chimeric grids into the main grids that intersect with them. This is necessary to be able to take into account the influence of inhomogeneities described by these chimeric grids when calculating at the next time step [10]. Further, the next time step begins with interpolation from the main grid to the boundary nodes of the chimeric grids that intersect with the main grid. Thus, the simulation of the interaction of various regions described by chimeric grids with other parts of the simulated area is achieved. This approach is designed to achieve greater accuracy when performing calculations, especially in cases where the calculation area contains heterogeneous areas located in different places of the simulated area.

3. CRACKS

Regular rectangular grids were used to represent the fractured medium. The continuous medium was described by a single rectangular grid, and the cracks were defined using overset rectangular grids, coaxial to the described cracks. The method used for calculating a straight crack on a regular rectangular grid and its implementation in relation to the grid-characteristic method was described in the article [11]. The adjusted regular rectangular grid was necessary to account for the crack of the coaxial rotated grid. Thus, in the proposed method, it is necessary to use the number of overset grids equal to the number of cracks taken into account.

However, there is another way to define a rotated crack that does not require the use of overset grids. This method works by replacing one crack with many small cracks tied to the nodes of the main grid, and was also described in [12,13]. Despite the fact that both methods provide sufficient accuracy of calculations, the use of many small cracks can lead to an increase in the number of computational operations, and in some cases, may introduce an additional error associated with the "ladder structure" of the crack described by such a method. Thus, the choice between these methods may depend on the specific conditions and the required accuracy of calculations.

To verify this method, a number of test calculations were performed to calculate the propagation of wave disturbances originating from a point source with a frequency of $f = 15$ Hz for various angles of rotation of the crack model. The angle of rotation of the crack is the angle between the axes OX of the overset and the main grid. The disturbances created by the source are described by the Ricker wavelet.

During the calculations, a regular rectangular grid of 700×700 nodes, each measuring 2 m, was used to describe a continuous medium. To describe rotated cracks, rotated regular rectangular grids of 32×13 nodes were used, consisting of cells of 2 m. The characteristics of the continuous medium were as follows: density $\rho = 400$ kg/m^3; longitudinal velocity of the elastic wave $C_p = 2850$ m/s; lateral velocity $C_s = 1650$ m/s.

In this work, the propagation of dynamic wave disturbances was calculated during a time step of $dt = 0.3$ ms for 0.75 seconds. The scheme of setting up in a series of test calculations for various angles of rotation

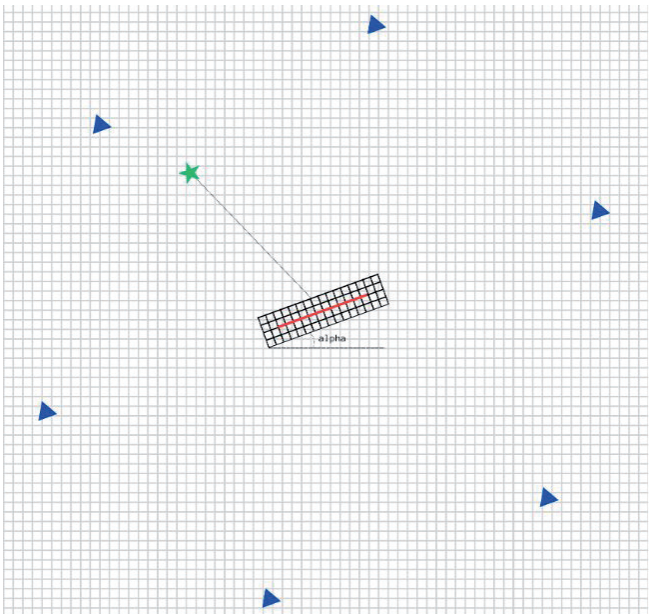

Fig. 1. *Gray lines indicate the edges of the main grid, black edges of the overset one. The blue triangles indicate the positions of the receivers, the green star indicates the position of the source of elastic waves.*

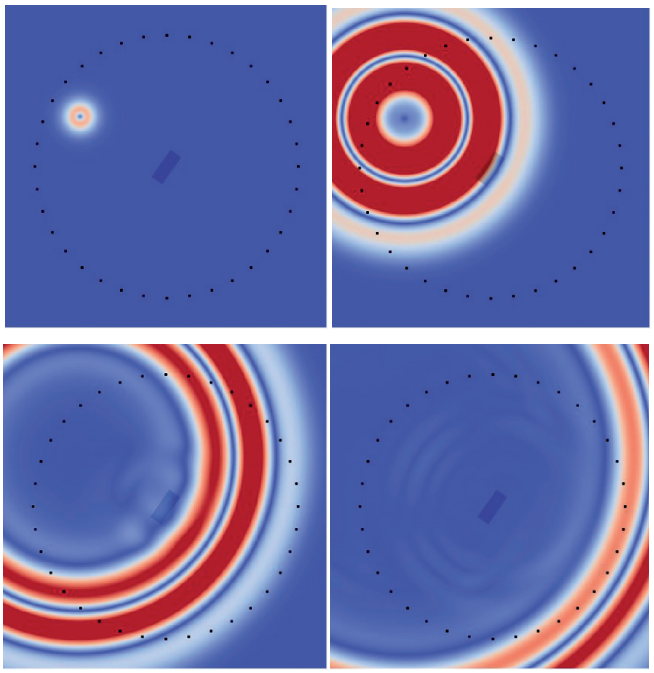

Fig. 2. *Wave patterns of the tension of a medium containing a rotated crack described by means of a overset grid in the presence of a point source of an elastic wave.*

of the crack relative to the axes of the main grid is shown in **Fig. 1**, in this series, the angle α is variable in Fig. 1, the angle between the normal to the crack and the segment from the center of the crack to the source remains unchanged and is 5°. At the same time, from calculation to calculation, the position of the source remains unchanged, and the overset grid-crack-receivers system rotates relative to the source. Visualization of the propagation of tension in the medium, under the conditions of the described calculation for α = 55° in the form of wave patterns is shown in **Fig. 2** visualization of the propagation of voltage in the medium, under the conditions of the described calculation for α = 55 ° in the form of wave patterns is shown in Fig. 2.

As a measure to assess the correctness of the proposed method of modeling a single crack at different angles of rotation, the average error according to the *L2* norm was used, calculated for all receivers throughout the entire modeling period. To compare the results, reference data obtained by turning the crack by an angle α = 0° were used. A graphical representation of the error dependence for various components of the medium tension tensor can be seen in **Fig. 3**.

The results showed that the method is quite accurate when modeling a crack at small angles of rotation of the crack relative to the axes of the main grid, but at steeper angles, additional research is required to refine the accuracy of the method. It should be emphasized that the maximum value of the error we obtained for both

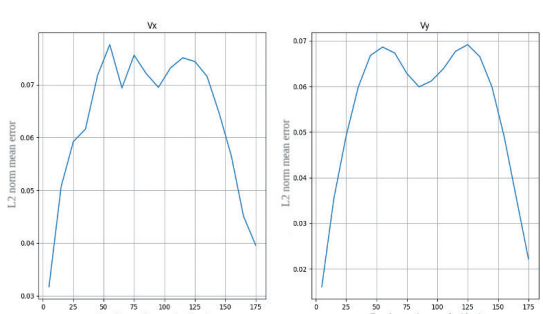

Fig. 3. *The average error according to the L2 norm for all receivers from the angle of rotation of the crack.*

components of the tension does not exceed 0.08, demonstrating the effectiveness of the method we propose.

The correctness of the method was checked when simulationg a single crack for different angles of rotation relative to the axes of the main grid. The results showed that the method gives fairly accurate results in this case. However, for convincing confirmation of the method's abilities in a wider range of conditions, additional research is needed. In particular, modeling of several cracks interacting with each other should be considered, as well as modeling of cracks at different angles between the crack normal and the direction to the source.

4. PORES

To accurately simulate the propagation of elastic waves with hollow holes, the method of overset grids was proposed [14]. It allows you to describe the free boundary conditions of a round or ellipse-shaped hole, forming an annular curved grid. This is achieved by a one-to-one transformation of a uniform regular grid into a curved one consisting of a ring of nodes. Periodic boundary conditions were applied at the grid nodes on the boundaries perpendicular to it. These borders, marked in red in **Fig. 4,** completely coincide and close the grid into a ring, which makes it possible to simulate the propagation of perturbation in nodes at these boundaries in any direction similar to the internal nodes of the grid.

Periodic boundary conditions are implemented in such a way that for nodes located close to one of the boundaries, the neighbor nodes are also located at the opposite boundary. The outer side of such a "looped" grid has no boundary conditions. The implementation of periodic boundary conditions makes it possible to describe hollow holes with an equilateral polygon, which is

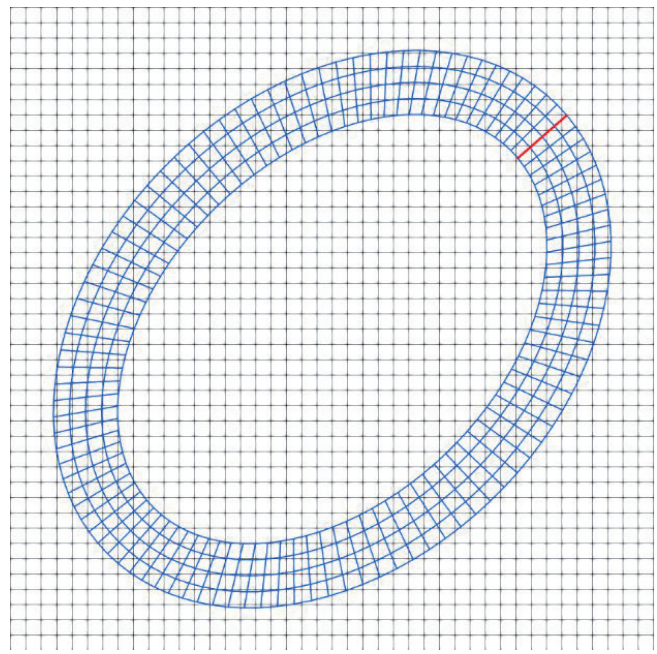

Fig. 4. *Black lines indicate the edges of the main grid, blue edges of the overset one. The red line indicates the position of the ends of the overset grid having periodic boundary conditions.*

formed on the inner side of the overset grid. Unlike a poly-line consisting of segments perpendicular to each other that coincide with the edges of the main regular grid, when using a "ladder" description of the boundary by a regular grid, this method is more accurate and correct.

The boundary of the overset grid, which is the inner boundary of the ring, is used to determine the boundary conditions of the free surface that form the wall of the hollow hole. Thus, it is possible to simulate the propagation of elastic waves in a medium in which there are hollow pore inclusions of various ellipse shapes, a special case of which are round pores. The wave patterns obtained as a result of modeling the interaction of an elastic wave with an ellipse-shaped hole implemented by the proposed method are shown in **Fig. 5**.

To verify the correctness of the use of our method in modeling the propagation of elastic waves in an inhomogeneous

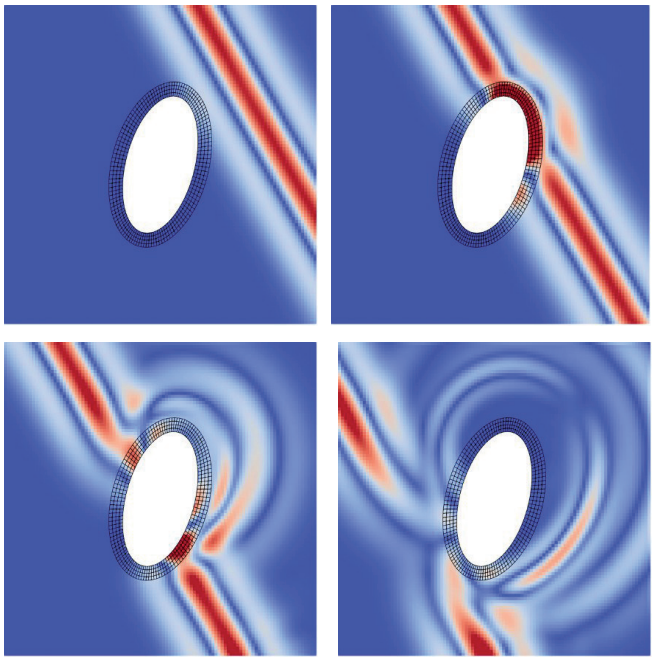

Fig. 5. *Wave patterns of the tension of a medium containing a hollow hole of elliptical shape during the passage of a plane elastic wave.*

medium through single holes, a series of calculations was carried out. They made it possible to check the symmetry of the implementation of the overset grid system and the main grid in the case of applying a periodic boundary condition on the closed boundaries of the overset grid forming a ring around the hole.

For numerical evaluation, we performed a series of calculations in a square area in the presence of a round hole. The characteristics of the continuous medium were as follows: density ρ = 2500 kg/m^3; longitudinal velocity of the elastic wave C_p = 3000 m/s; lateral velocity C_s = 1500 m/s. In the work, the propagation of dynamic wave disturbances was simulated during a time step of dt = 0.2 ms for 0.12 seconds.

The main grid is a square uniform grid of 450×450 nodes of 1.8 m each, the overset grid is also represented by a square uniform grid of 119×5 nodes, measuring 1.8 m. In addition, we have located 72 receivers at a

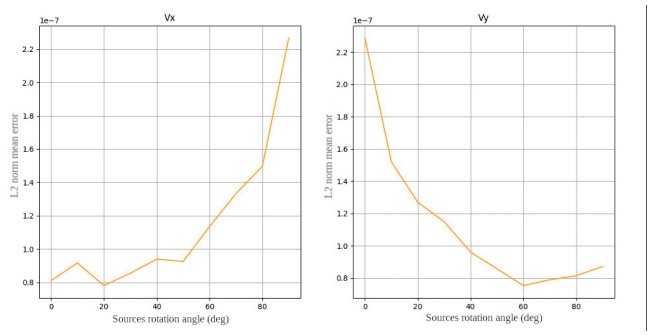

Fig. 6. *Graph of the dependence of the accumulated error according to the L2 norm on various angles between the incident wave front and the axis of the main grid.*

distance of 12 meters from the outer edge of the overset grid. Then we superimposed two plane waves with a frequency of 100 Hz on the described hole, symmetrically with respect to a straight line passing through the center of the hole at a variable angle. As a result of this calculation, the sum of errors of the signal received by the receivers according to the *L2* norm during the entire simulation period was calculated. The results of calculating this metric for various angles between a straight line parallel to the planes of incident waves and the Ox axis are shown in **Fig. 6.**

As can be seen from the graph shown in Fig. 6, the error for different components of the tension tensor increases at different angles. This dependence is explained by the features of the numerical method used in modeling the propagation of elastic perturbations along the longitudinal axes of the main computational grid. The calculations performed have shown the high accuracy of our method in modeling the propagation of elastic waves in a medium in the presence of a circular inhomogeneity. The data obtained demonstrate that our method can be used to solve complex problems related to modeling elastic waves in porous media.

5. CONCLUSION

The method of overset grids in combination with a grid-characteristic method for modeling the propagation of elastic waves in an inhomogeneous medium with various inhomogeneities, such as cracks and pores, is considered. In addition to describing the implementation of the proposed method, the ways of validating the applicability of the overset grid method are considered in detail. The results of validation of the proposed method are demonstrated, while the accuracy of the proposed method is estimated as a result of test calculations.

It is found that the proposed method provides high accuracy in modeling the propagation of elastic waves through an elastic medium having such inhomogeneities as cracks and pores. An important conclusion is that the presented method can be used in various fields related to the modeling of elastic waves in an inhomogeneous medium, and its potential can be revealed in future studies.

REFDRENCES

1. Favorskaya AV, Zhdanov MS, Khokhlov NI, Petrov IB. Modelling the wave phenomena in acoustic and elastic media with sharp variations of physical properties using the grid-characteristic method. *Geophysical Prospecting,* 2018, 66(8):1485-1502.
2. Petrov IB, Khokhlov NI. Modeling 3D seismic problems using high-performance computing systems. *Mathematical Models and Computer Simulations,* 2014, 8:342-350.
3. Qi Y, Chen X, Zhao Q, Luo X, Feng C. Seismic wave modeling of fluid-saturated fractured porous rock: Including fluid pressure diffusion effects of discrete distributed large-scale fractures. *EGUsphere*, 2023, 1-26 p. DOI:10.5194/egusphere-2022-1388.
4. Liu J, Wei XC, Ji YX, Chen TS, Liu CY, Zhang CT, Dai MG. An analysis of seismic scattering attenuation in a random elastic medium. *Applied Geophysics,* 2021, 8(4):344-354. DOI:10.1007/c11770-011-0296-y.
5. Biot MA. Theory of propagation of elastic waves in a fluid-saturated porous solid. I. Low-frequency range. *The Journal of the Acoustical Society of America*, 1956, 28(2):168-178.
6. Berryman JG. Origin of Gassmann's equations. *Geophysics,* 1999, 64(5):1627-1629. DOI: 10.1190/1.1444667.
7. Gassmann F. On elasticity of porous media. *Classics of Elastic Wave Theory*, 2007, pp. 389-408.
8. Li T, Wang Z, Yu N, Wang R, Wang Y. Numerical study of pore structure effects on acoustic logging data in the borehole environment. *Fractals,* 2020, 28(3):2050049-518. DOI: 10.1142/S0218348X20500498.
9. Cho Y, Gibson RL, Vasilyeva MV, Efendiev Y. Generalized multi-scale finite elements for simulation of elastic wave propagation in fractured media. *Geophysics*, 2017, 83(1):WA9-WA20. DOI: 10.1190/geo2017-0076.1.
10. Petrov IB, Khokhlov NI. Modeling 3D seismic problems using high-performance computing systems. *Mathematical Models and Computer Simulations,* 2014, 6(4):342-350. DOI: 10.1134/S2070048214040061.
11. Khokhlov N, Favorskaya A, Stetsyuk V, Mitskovets I. Grid-characteristic method using Chimera meshes for simulation of elastic waves scattering on geological fractured zones. *Journal of Computational Physics,* 2021, 446(1):110637. DOI: 10.1016/j.jcp.2021.110637.
12. Khokhlov N, Stognii P. Novel Approach to Modeling the Seismic Waves in the Areas with Complex Fractured Geological Structures. *Minerals*, 2020, 10(2):122. DOI: 10.3390/min10020122.

13. Stognii P, Khokhlov N, Zhdanov M. Novel approach to modelling the elastic waves in a cluster of subvertical fractures. *81st EAGE Conference and Exhibition,* 2019, 1:1-5. DOI: 10.3997/2214-4609.201901014.
14. Khokhlov NI, Stetsyuk VO, Mitskovets IA. Overset grids approach for topography modeling in elastic-wave modeling using the grid-characteristic method. *Computer Research and Modeling,* 2019, 11(6):1049-1059.

DOI: 10.17725/rensit.2023.15.193

Calculation of rolling stock movement along the railway track by the grid-characteristic method

[1,2]Anton A. Kozhemyachenko

[1]Moscow Institute of Physics and Technology, https://mipt.ru/
Dolgoprudny 141700, Moscow region, Russian Federation
[2]Scientific Research Institute of System Analysis of RAS, https://www.niisi.ru/
Moscow 117218, Russian Federation
E-mail: anton-kozhemyachenko@yandex.ru

Received May 04, 2023, peer-reviewed May 11, 2023, accepted May 18, 2023

Abstract: **The application of a grid-characteristic method is proposed for numerical simulation of the movement of rolling stock along a railway track laid on an earth and a bridge. In the study, the railway track is presented using a dynamic system of equations of the theory of elasticity of hyperbolic type. The grid-characteristic method relies on the characteristic properties of the system under consideration and uses finite-difference schemes of high order of accuracy to obtain a space-time solution. The features of railway structures are considered by changing the boundary conditions and conditions at the contact borders. To simulate the areas of contact of wheel pairs of rolling stock with the rail – the "wheel-rail" system – a previously developed pressure boundary condition is applied, modified so as to consider multi-element rolling stock. As a result of computer simulation of the movement of rolling stock along the railway track of various types, full-wave stress distribution in the track structure is obtained, which makes it possible to predict dangerous sections of rolling stock movement.**

Keywords: **computer simulation, grid-characteristic method, wheel-rail, rolling stock, railway track**

UDC 519.63

Acknowledgements: The work was carried out within the framework of the state task of the Federal State Institution «Scientific Research Institute for System Analysis of the Russian Academy of Sciences» on the topic No. FNEF-2022-0005 "Mathematical Modeling of Dynamic Processes in Deformable and Reacting Media using Multiprocessor Computing Systems", Reg. No. 1021060708369-1-1.2.1.

For citation: Anton A. Kozhemyachenko. Calculation of the movement of rolling stock along the railway track by the grid-characteristic method. *RENSIT: Radioelectronics. Nanosystems. Information Technologies,* 2023, 15(2):193-198e. DOI: 10.17725/rensit.2023.15.193.

Contents

1. INTRODUCTION

The problems of monitoring and safety during railway transportation have significant importance for the development of heavy-weight and high-speed movement of rolling stock in various operating conditions. Much attention is paid to the problems of force modeling in the "wheel-rail" system, the analysis of contact spots and wear models of wheel sets and rails [1-5], the design features of the track [6-7], movement on ballast and with riding on slabs of the railway track [8-10].

For numerical modeling of this class of problems finite element approaches, Galerkin

methods [11-15] are often used, including commercial software ANSYS, ABAQUS, etc.

In this paper, we propose the application of the grid-characteristic method that allows us to consider the problems of rolling stock movement in a dynamic formulation and to investigate the influence of wave processes during rolling stock movement using finite-difference schemes of high order accuracy in time and space [16-18].

2. MODELS AND METHODS

For numerical simulation of the problem of train movement, the railway track is represented as a set of layers of an isotropic linear elastic medium described in the two-dimensional case by a system of equations:

$$\frac{\partial \mathbf{q}}{\partial t} + \mathbf{A}_1 \frac{\partial \mathbf{q}}{\partial x} + \mathbf{A}_2 \frac{\partial \mathbf{q}}{\partial y} = 0, \quad (1)$$

$$\mathbf{q} = (v_x, v_y, \sigma_{xx}, \sigma_{yy}, \sigma_{xy})^T, \quad (2)$$

$$\mathbf{A}_1 = \begin{pmatrix} 0 & 0 & -\frac{1}{\rho} & 0 & 0 \\ 0 & 0 & 0 & 0 & -\frac{1}{\rho} \\ -\lambda-2\mu & 0 & 0 & 0 & 0 \\ -\lambda & 0 & 0 & 0 & 0 \\ 0 & -\mu & 0 & 0 & 0 \end{pmatrix},$$

$$\mathbf{A}_2 = \begin{pmatrix} 0 & 0 & 0 & 0 & -\frac{1}{\rho} \\ 0 & 0 & 0 & -\frac{1}{\rho} & 0 \\ 0 & -\lambda & 0 & 0 & 0 \\ 0 & -\lambda-2\mu & 0 & 0 & 0 \\ -\mu & 0 & 0 & 0 & 0 \end{pmatrix}, \quad (3)$$

where in (2) $\mathbf{q}$ – the vector of the initial functions, which include the components of the perturbation propagation velocity $\mathbf{v}$ and the components of the symmetric Cauchy stress tensor $\boldsymbol{\sigma}$, in (3) λ, μ – the Lame parameters that determine the elastic properties of the material. Matrices $\mathbf{A}_1$, $\mathbf{A}_2$ have a set of eigenvalues $\{c_P, -c_P, c_S, -c_S, 0\}$, where $c_P = \sqrt{(\lambda+2\mu)/\rho}$ – velocity of propagation of longitudinal waves, $c_S = \sqrt{\mu/\rho}$ – velocity of propagation of transverse waves. Thus, initial system (1) is hyperbolic, which means that the matrices $\mathbf{A}_1$, $\mathbf{A}_2$ can be represented as

$$\mathbf{A} = \boldsymbol{\Omega}\boldsymbol{\Lambda}\boldsymbol{\Omega}^{-1},$$

where the matrix $\boldsymbol{\Omega}$ consists of columns that are the right eigenvectors of the original matrix, which, in turn, correspond to the eigenvalues, which are elements of the diagonal matrix $\boldsymbol{\Lambda}$. Splitting the system (1) in spatial directions and using the transition to Riemann invariants $\boldsymbol{\omega} = \boldsymbol{\Omega}^{-1}\mathbf{q}$, which are transferred according to the characteristics of the hyperbolic system, we obtain the hyperbolic system from linear transfer equations with constant coefficients in Riemann invariants

$$\frac{\partial \boldsymbol{\omega}}{\partial t} + \boldsymbol{\Lambda}\frac{\partial \boldsymbol{\omega}}{\partial x} = 0. \quad (4)$$

The system in Riemann invariants (4) on the upper layer in time can be numerically integrated using finite-difference schemes, for example, using the Rusanov scheme [19], used in calculations in this paper, of the third order in time and space. To move to the components $\mathbf{v}$ and $\boldsymbol{\sigma}$ on the upper layer in time after calculating the Riemann invariants, the inverse transformation is used $\mathbf{q} = \boldsymbol{\Omega}\boldsymbol{\omega}$.

The basic model of the construction of a railway track laid on the earthen bed is shown in **Fig. 1**, and on the bridge structure in **Fig. 2**. The

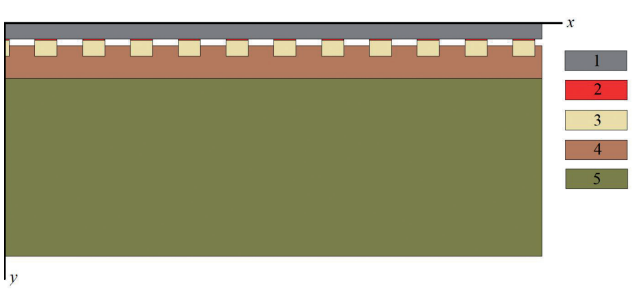

Fig. 1. *The railway track laid on the roadbed: 1 – rail, 2 – dampers, 3 – sleepers, 4 – ballast, 5 – earthen bed.*

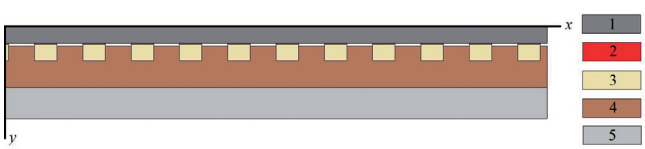

Fig. 2. *Railway track on the bridge: 1 – rail, 2 – dampers, 3 – sleepers, 4 – ballast, 5 – supporting structure.*

Table 1

Elastic parameters of media.

Medium	Velocity P-waves, m/s	Velocity S-waves, m/s	Density, kg/m³
Rail	5740	3092	7800
Damper	700	120	1200
Sleeper	4200	2200	2500
Balast	500	300	1400
Earthen bed	2000	1000	2000
Supporting structure	4200	2200	2500

elastic characteristics of the media are given in **Table 1**. The total length of the track section in both cases was 25 m. Free boundary conditions were set at the boundaries of the media that were elements of the corresponding model

$$\boldsymbol{\sigma}\cdot\mathbf{n} = 0, \quad (5)$$

where $\mathbf{n}$ – normal to the corresponding boundary.

Between the contact media (medium 1 and medium 2), a condition of complete adhesion is set at the contact boundary, which is described by the expressions

$$\mathbf{v}_1 = \mathbf{v}_2,$$

$$\boldsymbol{\sigma}_1\cdot\mathbf{n} = \boldsymbol{\sigma}_2\cdot\mathbf{n},$$

here $\mathbf{n}$ – normal to the boundary of the contacting medium 1.

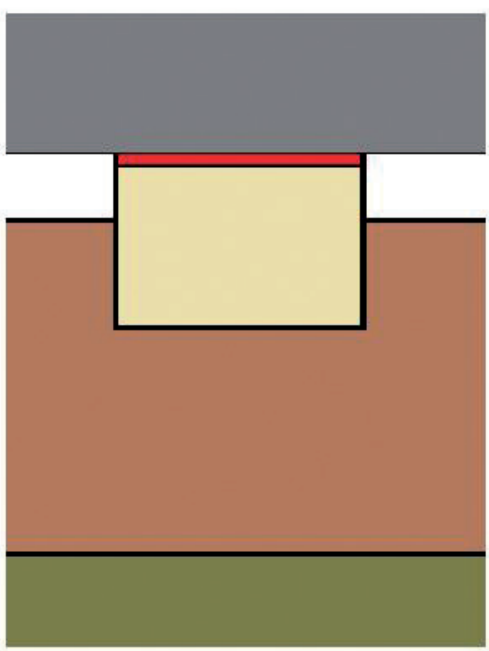

Fig. 3. *The position of the damper (red) between the rail and the sleeper.*

Absorption conditions are used on the left and right boundaries of the integration regions in Fig. 1 and Fig. 2. Similarly, this condition is used for the lower boundary of the integration region in Fig. 1 for the sedimentary rock layer. In the case of a bridge structure, a free boundary condition is set at the lower boundary of the supporting structure (5). Between the rail and the sleeper, a damper is used in both settings for clarity, shown separately in **Fig. 3**.

To simulate the movement of rolling stock along the railway track from Fig. 1 and Fig. 2, the force boundary condition in the wheel-rail system from [16] is used with the modification that allows to consider several elements of the rolling stock at once in **Fig. 4**. The geometric parameters of the rolling stock element are H_{TRAIN} = 7.7 m, L_{TRAIN} = 1.85 m, mass 90 t. The pressure of the wheel without defects on the rail in the "wheel-rail" system is equal 188 MPa.

In the calculation the integration areas in Fig. 1 and Fig. 2 were covered with rectangular calculation meshes with the constant step for the corresponding medium according to **Table 2**, the integration step in time was 10^{-7} s.

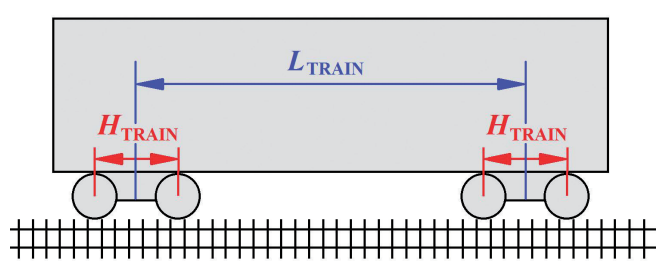

Fig. 4. *Rolling stock element.*

Table 2

Meshes parameters.

Medium	Step along OX, m	Step along OY, m
Rail	0.01	0.005
Damper	0.01	0.001
Sleeper	0.01	0.005
Balast	0.01	0.005
Earthen bed	0.01	0.010
Supporting structure	0.01	0.010

3. RESULTS AND DISCUSSION

Fig. 5 and **Fig. 6** show the results of calculations of the dynamic load distribution of the vertical component of the Cauchy stress tensor at various points in time when the rolling stock consisting of two elements is moving along the railway track laid on the earthen bed with the velocity of 120 km/h and on a bridge with the velocity of 72 km/h, respectively. To account for the slow increase in stresses due to the interaction of the train and the rail from zero to a set value in the wheel-rail system 170000 iterations have performed. The total number of iterations over time is 680000, i.e. the total movement time of the rolling stock is 0.051 s.

The obtained results show the importance of consideration in the mathematical model the number of relevant standards of railway

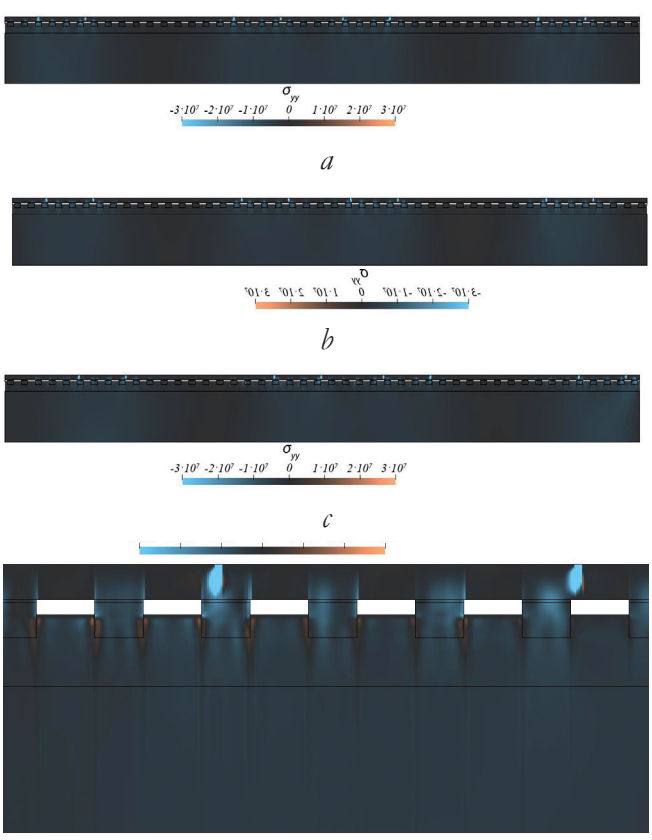

a

b

c

d

Рис. 5. *The movement of the rolling stock of two elements on the earthen bed: a – the beginning of movement, b – 0.0255 s, c – 0.051 s, d – the enlarged picture on the left at 0.051 s.*

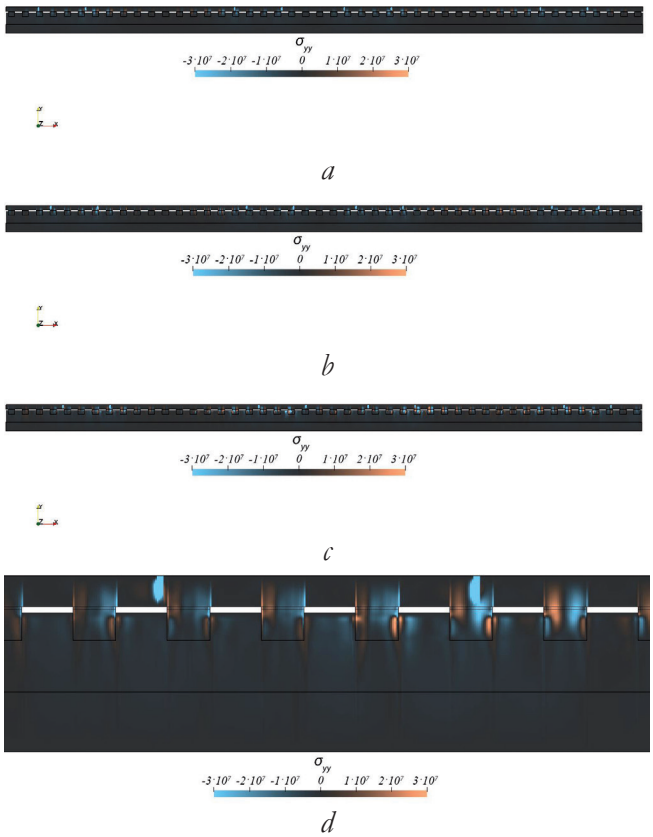

a

b

c

d

Рис. 6. *The movement of the rolling stock of two elements on the bridge: a – the beginning of movement, b – 0.0255 s, c – 0.051 s, d – the enlarged picture on the left at 0.051 s.*

track design, some of which were not consider earlier in [16-18]: the presence of the damping layer between rails and sleepers, the use of reinforced concrete sleepers, unlike wooden ones. Due to the modification of the boundary condition used, it is possible to specify the rolling stock consisting of a large number of elements. When comparing the wave patterns in Fig. 4 and Fig. 5 it can be seen that when moving on the bridge, the more pronounced stress pattern is formed in the bridge structure in the area of the rail-damper-sleeper junction than when moving along the earthen bed. This is due to the fact that in the case of movement along the earthen bed, the wave front propagate into the thickness of sedimentary rocks, whereas on the lower surface of the bridge, the incoming wave front is reflected back into the track structure.

4. CONCLUSIONS

Using the grid-characteristic method on structured rectangular meshes in combination with the modification of the boundary condition for the wheel-rail system, it is possible to obtain stress distributions during the movement of rolling stock consisting of the large number of elements along the railway track at various points in time. The proposed approach and mathematical models make it possible to consider the damping layer between rails and sleepers, change the parameters and type of construction using various types of contact and boundary conditions, speed mode. The obtained algorithms and models can be used to analyze wave effects during the movement of rolling stock and to formulate the problem of the movement of rolling stock in conditions of transition from the railway track laid on an earthen bed to the track laid in conditions of the bridge structure, considering changes in the rigidity of the sub-rail base.

REFERENCES

1. Six K, Mihalj T, Trummer G, Marte C, Krishna VV, Nia SH, Stichel S. Assesment of running gear performance in relation to rolling contact fatigue of wheels and rails based on stochastic simulations. *Proceedings of the Institution of Mechanical Engineers Part F Journal of Rail and Rapid Transit,* 2019, 234(4):0954409719879600. DOI: 10.1177/0954409719879600.
2. Goryacheva I, Torskaya EV. Modeling the Accumulation of Contact Fatigue Damage in Materials with Residual Stresses under Rolling Friction. *Journal of Friction and Wear*, 2019, 40(1):33-38.
3. Torskaya EV, Goryacheva IG, Muravyeva TI, Shcerbakova OO, Tsukanov IY, Meshcheryakova AR, Shkaley IV, Zagranichek KL, Zakharov SM, Shur EA. Rolling Contact Fatigue Damage in Welded Rail Steel Joints. *Physical Mesomechanics,* 2023, 26(1):7-18; doi: 10.1134/S1029959923010022.
4. Loktev AA, Korolev VV, Shishkina IV, Basovsky DA. Modeling the Dynamic Behavior of the Upper Structure of the Railway Track. *Procedia Engineering*, 2017, 189:133-137. DOI: 10.1016/j.proeng.2017.05.022.
5. Huang YB, Shi LB, Zhao XJ, Cai ZB, Liu QY, Wang WJ. On the formation and damage mechanism of rolling contact fatigue surface cracks of wheel/rail under dry condition. Wear, 2018, 400:62-73. DOI: 10.1016/j.wear.2017.12.020.
6. Zakeri JA, Rezvani FH. Failures of railway concrete sleepers during service life. International *Journal of Construction Engineering and Management*, 2012, 1(1):1-5.
7. Ngamkhanong C, Kaewunruen S, Costa BJA. State-of-the-art review of railway track resilience monitoring. *Infrastructures*, 2018, 3(1):3.
8. Liu K, Lombaert G, De Roeck G. Dynamic analysis of multi-span viaducts under the passage of the train using a substructure approach. *Bridge Engineering,* 2014, 19(1):83-90.
9. Poliakov V, Dang TN. Wheel-rail impact interaction on the high-speed railroad bridges. *Russian Journal of Transort Engineering,* 2019, 6(1):15SATS119.
10. Charoenwong C, Connolly DP, Colaco A, Alves Costa P, Woodward PK, Romero A, Galvin P. Railway slab vs ballasted track: A comparison of track geometry degradation. *Construction and Building Materials*, 378:131121.
11. Adak D, Pramod A, Ooi E, Natarajan S. A comined virtual element method and the scaled boundary finite element method for linear elastic fracture mechanics. *Eng. Anal. Boundary Elem*, 2020, 113:9-16.
12. Tang Z, Liu F, Guo S, Chang J, Zhang J. Evaluation coupled finite element/meshfree method for a robust full-scale crashworthiness simulation of railway vechicles. *Adv. Mech. Eng,* 2016, 8:1687814016642954.

13. Nejad R, Liu Z, Ma W, Berto F. Reliability analysis of fatigue crack growth for rail steel under variable amplitude service loading conditions and wear. *Int. J. Fatigue*, 2021, 152:106450.
14. Krishnamoorthy RR, Saleheen Z, Effendy A, Alisibramulisi A, Awaludin A. The Effect of Rubber Pads on The Stress Distribution for Concrete Railway Sleepers. *IOP Conference Series Materials Science and Engineering*, 2018, 431(11):112007.
15. Shahraki M, Warnakulasooriya C, Witt KJ. Numerical Study of Transition Zone Between Ballasted and Ballastless Railway Track. *Transportation Geotechnics*, 2015, 3:58-67.
16. Kozhemyachenko AA, Petrov IB, Favorskaya AV, Khokhlov NI. Boundary conditions for modeling the impact of wheels on railway track. *Comput. Math. Math. Phys.*, 2020, 60(9):1539-1554.
17. Kozhemyachenko AA, Petrov IB, Favorskaya AV. Calculation of the stress state of a railway track with unsupported sleepers using the grid-characteristic method. *J. Appl. Mech. Tech. Phys.,* 2021, 62:344-350.
18. Koyhemzachenko AA, Kabanova AS, Petrov IB, Favorskaya AV. Modeling Movement of Train Along Bridge by Grid-Characteristic Method. Smart Modelling For Engineering Systems. *Smart innovation, Systems and Technologies,* 2021, 214:165-174.
19. Favorskaya A, Khokhlov N. Accounting for curved boundaries in rocks by using curvilinear and Chimera grids. *Procedia Computer Science,* 2021, 192:3787-3794.

IN MEMORY OF ROSTISLAV V. BELYAEV

PACS: 01.60.+q

DOI: 10.17725/rensit.2023.15.199

On April 19, 2023, at the age of 89, Rostislav Vladimirovich Belyaev, Candidate of Physical and Mathematical Sciences, Senior Researcher at the Laboratory of Physical Fundamentals of Nanocomposite Materials for Information Technology, Department of the Physical Fundamentals of Nanoelectronics, Kotelnikov Institute of Radio Engineering and Electronics of the Academy of Sciences of the Russian Federation, Corresponding Member of the Russian Academy of Natural Sciences, a well-known specialist in the field of generation of microwave noise oscillations and processing of broadband signals based on dynamic chaos.

Rostislav Vladimirovich was born in 1934 in the city of Astrakhan. His father, VI Belyaev, a surgeon, graduated from Astrakhan Medical Institute. He died in 1939 at age 30 from an incurable disease. Paternal grandfather - IA Belyaev was born in 1885 in the Kaluga province, graduated in 1914, the Medical Faculty of the University of Emperor Nicholas in Saratov. Was called up for military service, was awarded the Order of St. Stanislaus 2 and 3rd degree, the Order of St. Anne 3rd degree. Since 1915, worked at the Department of Ophthalmology of the Imperial University of Nicholas, from 1923 to 1933. headed the Eye Clinic of Astrakhan Medical Institute at the rank of professor, from 1933 to 1944. headed the Department of Ophthalmology at Saratov State Medical Institute. Mom graduated from Astrakhan Medical Institute and worked all her life pediatrician. Her parents were military, but by her husband mother - entrepreneurs.

After graduating in 1952, high school, RV Belyaev enters the Moscow Institute of Physics and Technology in the 1st specialty - Electronics (faculties then MIPT not yet exist). In the process of learning takes place in the MIPT basic practice and training on leading electronics industry of the USSR Research Institute "Istok" Fryazino Moscow region. Thesis at the end of training devoted to the study of field emission properties of rare-earth elements, under the supervision of Ph.D. BS Kulvarskoy performs in the newly established in Moscow on the initiative of academician AI Berg Institute of Radio Engineering and Electronics, Academy of Sciences of the USSR (1953, in the building of the Faculty of Physics, Moscow State University, migrated to the Lenin Hills).

After graduation RV Belyaev in 1958 distributed in IRE USSR Academy of Sciences for the post of junior researcher, where the Department of Electronics, headed by Corresponding Member of the USSR Academy of Sciences DV Zernov, engaged in the development and study of electron-beam systems with flat beam for automatic coding signals. In 1971, during the reorganization of the structure of RV Belyaev transferred to the laboratory headed by VYa Kislov, and thus changes the direction of the work performed.

The main themes of future activities RV Belyaev associated with developing area generating chaotic oscillations with a level greater than the noise floor systems, that is due to the properties of nonlinearity and delay effects, implemented in particular in systems with feedback delay feedback:

- research and development in the field of microwave generation broadband noise oscillations in plasma;
- research and the creation of electron-wave microwave devices;
- research and creation of a noise signal generator of the microwave range on the basis of solid state semiconductor devices.

Further, due to the transition from analog to digital, RV Belyaev conducted research algorithms of pseudo-numeric (integer) sequences and their properties:

- development of digital broadband information technologies based on dynamic chaos for processing, transmission, storage and protection of information;
- development and application of research methods of fractal analysis of complex wideband signals.

The thesis is an RV Belyaev the title of Ph.D., completed in 1986, is devoted to the study of excitation noise oscillations in generators on the avalanche-transit diodes (ATDG). It is known that these oscillators are excited into oscillation, which together with the spectrum of the harmonic components comprises a continuous component with a level exceeding the feedback fluctuations of the avalanche current. In some cases, increasing operating current ATDG leads to the excitation of noise fluctuations without isolation of the harmonic components. Studies on simple models of self-oscillating systems such as the Van der Pol has shown that under certain conditions, even in such systems can be implemented modes of the complex nature of the oscillations. In order to identify the nature of the excitation of anomalous noise regulations in ATDG experimentally investigated such generators on simple systems that allow a controlled excite one-, two- and three-mode oscillation. It is shown that in these systems when the current ATDG modes implemented with the spectra vary according to the complexity of sequential scenarios generated oscillations typical for a large class of dynamical systems studied simple models. These results demonstrate the dynamic nature of the excitation of abnormal noise oscillations in such generators, although fluctuations of the avalanche current in such generators will undoubtedly affect the level of their appearance, but they are not the direct cause of the chaos, it is - in the complex dynamics of the diode-oscillating circuit. These results have practical application in the creation of practical systems generating wideband noise signals ATDG based on a power level comparable to the level of the oscillation generating ordered.

RV Belyaev, together with Institute staff developed, implemented and studied in the form of digital circuits forming algorithms broadband noise signal, which have found practical application in real-world applications.

Together with other members of the Institute, he repeatedly took part in field work and trials in various parts of the country from Kamchatka to Astrakhan, from Voronezh to Sevastopol.

Since 1958 to the present time Rostislav Belyaev - employee IRE RAS, from 1971 to 1986. - Junior Researcher, from 1989 to present - Senior Researcher, from 2007 to 2010. Acting Head of laboratory.

The scientific results RV Belyaev published in 65 articles in various journals and presented at 42 national and international conferences. Has 4 inventor's certificates.

RV Belyaev - conferee of several international and national conferences, schools systems with chaotic oscillations. Is responsible executor of the decree of the government, as well as on numerous grants RFBR and ISTC. Rostislav Vladimirovich - member Russian Scientific and Technical Society of Popov Radio Engineering, Electronics and Communication since its inception in 1991, corresponding member of the Russian Academy of Natural Sciences (2001) in the Department of Radio Electronics problems, nanoscale physics and information technology.

RV Belyaev since 2009 - Executive Secretary of scientific journal "RadioElectronics. Nanosystems. Information Technology "(RENSIT).

In 1997 he was awarded the honorary title of Veteran of Labor; he was awarded the medal "In commemoration of the 850th anniversary of Moscow", the badge "Honorary Radio Operator" the Ministry of Radio of Russian Federation.

Rostislav Vladimirovich - a tireless traveler and experienced water tourists, traveled the country and outcome of Far North - Kola Peninsula, Ural Mountains, Putoran, Kamchatka, tributaries of Pechora, Ob, Yenisei (Lower and Stony Tunguska), Lena, to the South - Lake Baikal, Issyk Kul, Tuva - the origins of the Yenisei region near border with Mongolia. Herewith he is actively promoting this lifestyle among employees, pulling them into their dizzying projects.

Life Rostislav Vladimirovich - a living history IRE, he - where need heavier laborious work, creating soil in which grew all important results of collective. Its reliability, natural intelligence, politeness, courtesy, responsiveness, high scientific erudition, amazing performance, devotion to work, integrity and responsibility - priceless gift to the his collaborators.

Rostislav Vladimirovich Belyaev was a very kind and warm, extremely decent and wise man, possessing at the same time strength and firm conviction in his research. A bright and eternal memory of him will remain in our hearts.

Relatives, friends, colleagues
and the Editorial Board RENSIT journal

IN MEMORY OF NIKOLAY N. ZALOGIN

PACS: 01.60.+q

DOI: 10.17725/rensit.2023.15.201

On May 31, 2023, at the age of 88, Nikolay Nikolayevich Zalogin, Leading Researcher of Physical Fundamentals of Nanocomposite Materials for Information Technologies Laboratory of the Physical Fundamentals of Nanoelectronics Department of V.A. Kotelnikov Institute of Radioengineering and Electronics of the Academy of Sciences of the Russian Federation, a well-known specialist in the field of generation of microwave noise oscillations, their application in radio electronic warfare, radar and broadband signal processing based on dynamic chaos.

A descendant (6th generation) of the old merchant family of the Zalogins from Bogorodsk (now – Noginsk) near Moscow, Nikolai Nikolayevich was born on August 6, 1935 in Moscow. Father – Zalogin Nikolai Georgievich (1902-1978), engineer, specialist in flue gas cleaning at thermal power plants in Moscow. During the war, he was awarded the Order of the Red Star for the creation of a system for masking smoke in the infrared range. Mother – Bauman Lyudmila Nikolaevna, researcher, laboratory head.

After graduating from secondary school in 1953, N.N. Zalogin on the second attempt, in 1954 entered the Moscow Institute of Physics and Technology. Since 1957, after the 3rd year, he passed basic and then undergraduate practice at the Institute of Radioengineering and Electronics (IRE) of USSR Academy of Sciences.

In 1960, he was hired at the IRE as a junior researcher to the Microwave Electronics Department under the direction of Academician of USSR Academy of Sciences Nikolai Dmitrievich Devyatkov, to the Electronic Generators Laboratory, led by Technical Sciences Doctor Chernov Z.S. In 1961, during the reorganization of the structure of the department, N.N. Zalogin is transferred to a laboratory led by Ph.D. V.Ya. Kislov, and, accordingly, the direction of the work performed by him changes. Initially, the Kislov laboratory was engaged in the study of the possibility of creating O-type plasma devices in the centimeter wavelength range. The successful development of this direction, as expected, made it possible to get rid of small-sized slow-wave systems in the millimeter wavelength range. Working in this direction as an experimenter, N.N. Zalogin was the first to discover (1962) the generation of microwave noise in a plasma-electron flow system (in a backward-wave plasma lamp). According to the application for the invention of the noise generator (authors N.N. Zalogin and V.Ya. Kislov), Authorship Certificate No. 28547 was received with priority dated April 15, 1963.

Since 1963 N.N. Zalogin is a correspondence post-graduate student at IRE, USSR Academy of Sciences. The dissertation work "Plasma Noise Generator" for the title of Technical Sciences Candidate, completed in 1967 with a successful defense, was devoted to the study of the generation of noise oscillations in the plasma-electron flow system as a result of its longitudinal interaction with a backward electromagnetic wave in the 10 mm wavelength range propagating along the plasma waveguide. The scientific adviser of the postgraduate

student Zalogin N.N. was the 16th Department head, Academician of USSR Academy of Sciences N.D. Devyatkov.

Since 1970, Nikolai Nikolaevich has been a senior researcher. In 1970, together with other laboratory workers, V.Ya. Kislov was transferred to the Fryazinsky branch of IRE in the lab. 166. In 1975 he was transferred back to the IRE Moscow part, but continued to work on the "noisetron" themes with the lab. 166. These works were awarded in 1980 by the USSR State Prize in science and technology (on a closed topic) to the team of authors of the IRE of USSR Academy of Sciences – Kislov V.Ya., Zalogin N.N. and Myasin E.A.

After the discovery of the effect of generation of noise oscillations in systems based on traveling-wave tubes with delayed feedback, the main subject of N.N. Zalogina was associated with this developing area of research – the generation of chaotic oscillations with a level exceeding the level of the system's own noise, that is, due to the properties of nonlinearity and delay effects, implemented, in particular, in systems with delayed feedback: research and development in the field of microwave generation broadband noise oscillations; research and creation of electron-wave devices in the microwave range; research and development of microwave noise signal generators based on solid-state semiconductor devices.

Together with other employees of the IRE, N.N. Zalogin repeatedly took part in field work and testing of the developed systems in various regions of the USSR from Kamchatka to Astrakhan, from Voronezh to Sevastopol.

Since 1999 N.N. Zalogin is a leading researcher at the V.A. Kotelnikov IRE of RAS.

The results of the scientific work of N.N. Zalogin published in more than 120 articles in various journals and presented at dozens of national and international conferences. When the group of co-authors collected material for publication, then the question "Who will write?" – followed the answer: "N.N. Zalogin, of course". He has 4 copyright Inventions Certificates, winner of two Awards of the USSR Council of Ministers (1984 and 1989). He is author of the monograph "Broadband Chaotic Signals in Radio Engineering and Information Systems" (Moscow, Radiotekhnika Publ., 2006), written in an amazing language for a scientific monograph, reflecting the author's rare literary gift with his sharp, imaginative, always ironic tone.

N.N. Zalogin is a participant in a number of international and republican conferences, schools on systems with chaotic oscillations. He was the responsible executor of work under the Government Decrees, as well as under numerous grants from the ISTC and RFBR. Nikolai Nikolaevich is a member of the A.S. Popov Russian Scientific and Technical Society of Radioengineering, Electronics and Communications since its inception in 1991. In 1997 he was awarded the honorary title of Labor Veteran; he was awarded the medal "In Commemoration of the 850th Anniversary of Moscow", the badge "Honorary Radio Operator" of the Russian Federation Ministry of Radio Industry.

Wife Zalogina (née Shidlovskaya) Elena Alexandrovna (1937-1999), chemist, employee of the Research Institute of Chemical Reagents and Highly Pure Chemical Substances. Sons (7th generation of the Zalogin family) Alexander (1961) – Candidate of Physical and Mathematical Sciences (children – Alexey, Tatyana, Maria, Andrey), and Vladimir (1964) – a specialist in the field of computer networks (son Ivan, 1998).

Since 1993, he lived in the Dunino village, Odintsovo district, Moscow region. The whole village went to him for help and advice on everything from technical to family matters. In the Dunino M.M. Prishvin Museum Nikolai Nikolaevich has always been a welcome participant in all key events in the museum life, almost a freelancer. In addition, being the grandson of the last owner of the Fryanovo estate near Moscow, which has now become a museum, Nikolai Nikolayevich participated in equipping the museum with exhibits.

The life of Nikolai Nikolaevich is a living history of the IRE RAS, his natural intelligence, excellent scientific erudition, amazing efficiency, responsiveness, integrity and responsibility are an invaluable gift to the team of his employees.

The bright memory of you, Nikolai Nikolaevich, will warm the hearts of all who knew you, for a long time.

Relatives, friends, colleagues
and the Editorial Board RENSIT journal